Laser Spectroscopy, Matrix Isolation and *Ab Initio* Studies of Free Radicals and Weakly Bound Complexes.

Thesis submitted for the degree of
Doctor of Philosophy
at the University of Leicester

by

Peter Robert Butler BSc. (Leicester)
Department of Chemistry
University of Leicester

September 2002

ProQuest LLC
789 East Eisenhower Parkway
P.O. Box 1346
Ann Arbor, MI 48106-1346

TITLE: Laser spectroscopy, matrix isolation and *ab initio* studies of free radicals and weakly bound complexes.

AUTHOR: Peter Robert Butler

ABSTRACT:

The work presented in this thesis applies laser spectroscopy, matrix isolation and *ab initio* calculations to the study of free radicals and weakly bound species.

The $\widetilde{C}-\widetilde{X}$ region of BaOH has been re-investigated in the gas phase at higher resolution than by previous workers. A new assignment of the recorded spectra is tentatively proposed based on the higher resolution achieved. The spectrum appears to be heavily perturbed, which seriously complicates the spectral assignment.

A new basis set extrapolation procedure has been developed for *ab initio* calculations on van der Waals complexes. The procedure developed, a modification of the Truhlar extrapolation, employs calculations using modest sized basis sets. This has been tested on 15 van der Waals species with well known equilibrium dissociation energies and bond distances. The modified Truhlar extrapolation procedure is found to be generally of comparative accuracy to CCSD(T)/aug-cc-pV5Z calculations but at much reduced computational cost.

The modified Truhlar extrapolation has been applied for the first time to HRgF molecules, where Rg is Ar, Ne and He. The potential energy surfaces generated for HHeF and HNeF represent the most accurate *ab initio* calculations to date on these species. The HArF calculations are of comparable accuracy to aug-cc-pV5Z calculations by other workers. Vibrational frequencies have also been calculated for all three molecules.

The modified Truhlar extrapolation procedure has been applied for the first time to RgC_2 clusters, where Rg is Ar, Ne and He. The potential energy surfaces generated. Rovibrational frequencies have been calculated for all three clusters. These lead to the conclusion that both ArC_2 and NeC_2 are spectroscopically observable, although this would be challenging.

Matrix isolation apparatus recently built for recording LIF spectra of trapped reactive intermediates has been tested, improved and evaluated. Vibrationally-resolved LIF spectra of benzene have been recorded. A metal containing free radical, CaCl has been trapped and observed using the apparatus.

STATEMENT OF ORIGINALITY

The work in this thesis was conducted by the author in the Department of Chemistry at the University of Leicester during the period between September 1998 and September 2002 and is original unless otherwise acknowledged in the text or references.

None of the work has been submitted for another degree at this or any other university.

Signed _____ Date _____

ACKNOWLEDGEMENTS

I would like to acknowledge the following people for support, assistance and amusement throughout my PhD.

I cannot thank my supervisor Andy enough for his continued support and always useful suggestions.

I must also thank Victor Mikhailov for assistance with the simulations of the BaOH rotationally resolved spectra and Martyn Wheeler for assistance on the use of the BOUND program (for calculating the energy levels of the RgC_2 species).

I must thank Mum, Dad and Andy for their continuous support, encouragement and always being there whenever I needed them.

A certain (odd) collection of friends for putting up with me on a sadly not frequent enough basis, Ian, Clare, Ian, Neil, Graham, Phil, Grizzle and the others.

Squidgy for being, well ..... squidgy - May ye live forever!

Finally, to Ria for being understanding enough to give me the time to finish writing.

Ta

LIST OF PUBLICATIONS

Some of the work in this thesis has appeared (or will appear) in the following publications.

"Application of the Truhlar basis set extrapolation procedure to *ab initio* calculations on van der Waals complexes." , P. R. Butler and A. M. Ellis, *Molec. Phys.*, **99** (2000) 525-529.

"Electronic spectroscopy in the $\widetilde{C} - \widetilde{X}$ region of BaOH: a complex vibronic system", P. R. Butler, V. Mikhailov and A. M. Ellis, in preparation.

"Application of the Modified Truhlar basis set extrapolation procedure to RgC_2 clusters", M. D. Wheeler, P. R. Butler, K. Patel and A. M. Ellis, in preparation.

"Application of the Modified Truhlar basis set extrapolation procedure to HRgF molecules", P. R. Butler and A. M. Ellis, to be published.

TABLE OF CONTENTS

LIST OF FIGURES AND TABLES

Figures:

Tables:

CHAPTER 1

Introduction

1. INTRODUCTION

1.1 PREAMBLE

The work presented in this thesis centres on the spectroscopic and theoretical investigation of short-lived molecules and clusters. Metal-containing free radicals, notably BaOH, have been investigated in the gas phase using laser spectroscopy. A new matrix isolation apparatus has also been developed to allow the van der Waals interactions between metal-containing free radicals and rare gas atoms to be probed. In support of the experimental studies of van der Waals complexes, *ab initio* calculations have been performed on a number of weakly bound species that contain the noble gases helium, neon and argon. A basis set extrapolation technique has been developed with the aim of allowing accurate and detailed calculations to be performed with limited computational resources.

In this introductory chapter some of the general background to this work is reviewed.

1.2 PAST AND PRESENT WORK

1.2.1 Laser spectroscopy of free radicals

Laser induced fluorescence (LIF) spectroscopy was the spectroscopic technique employed for both the gas phase and matrix isolation work presented in this thesis. Lasers offer several important features that are highly beneficial to the investigation of short-lived molecules including free radicals. Lasers are highly directional, coherent, bright and highly monochromatic.[1] The high intensities and narrow

linewidths of commercially available tuneable lasers make possible several highly sensitive spectroscopic techniques, one of which is LIF spectroscopy.

Although not essential, supersonic jets add another useful technique to the armoury of transient molecule spectroscopists. Supersonic jets were first introduced by Kantrowitz and Grey in 1951.[2] A key property of a supersonic jet is that molecules can be cooled to very low temperatures (a few kelvin) with minimal condensation occurring.[1] Thus a supersonic jet both significantly simplifies the spectra compared to molecules at room temperature, because fewer energy levels are populated, and prevents them from reacting for a short period of time while they are observed. These characteristics, when combined with LIF spectroscopy, offer the opportunity to observe free radicals and other short-lived species in the gas phase.

1.2.2 Matrix isolation

Matrix isolation first became possible when liquid helium was produced. The first experiments were carried out by Onnes in 1924.[3] However it was not until the early 1960s that matrix isolation became more common due to the much more widespread availability of liquid helium and the invention of microrefrigerators.[4] A range of spectroscopic techniques have been used in combination with matrix isolation, including UV/Vis absorption and emission spectroscopy, IR and ESR.

The matrix isolation technique is discussed in detail in Chapter 8. Briefly, it consists of trapping the target molecules inside a cage of other (usually noble gas) atoms/molecules. The cage around the target molecule isolates it from any interactions, thereby preventing it from reacting. The target molecule may then be observed in isolation via spectroscopic techniques. For example OH radicals may be produced in an excess of argon. The OH argon mixture is then directed on to a

surface cooled to a few kelvin, where upon the argon condenses, trapping the OH radicals in a cage of argon atoms.

Traditionally the main advantage of matrix isolation is that it allows short lived and highly reactive molecules to be trapped almost indefinitely (several hours or even days), thus allowing any observations via spectroscopy to be performed at leisure. Furthermore only a very small quantity of the target molecules need be produced and trapped to allow good quality spectra to be recorded.

In an ideal situation the inert species used to trap the reactive species will not interact with the trapped species at all. However in reality the host species does interact with the guest. Matrix isolation is less popular today than in the past, because laser spectroscopy is now capable of offering the ability to study short-lived species in the gas phase, where molecules are truly isolated. In contrast, a large part of this thesis is concerned with the study of weak interactions, and a cold matrix provides an excellent means for probing them.

1.2.3 Background to gas phase and matrix isolated studies in this work.

There are very few studies in the literature that make use of LIF spectroscopy to observe metal-containing free radicals in a matrix. One of the advantages of LIF combined with matrix isolation is that only a very small amount of the species of interest need be trapped within the matrix because LIF is typically 10^9 times more sensitive than IR;[5] indeed examples exist of single molecules being observed using LIF.[6,7] The combination of LIF with matrix isolation to investigate radicals offers the potential to investigate the very weak host-guest interactions that are present within the matrix. The spectra obtained from radicals trapped within a matrix can be compared to similar spectra of the radical that have been obtained in the gas phase.

This comparison should yield information on the weak interactions that are present. Indeed it is this possibility that ties all the threads of the work presented in this thesis together. If *ab initio* calculations on the weak bonding in the matrix between the radicals and the host species were performed it would most likely significantly aid interpretation of any matrix isolated LIF spectra. In order to perform meaningful *ab initio* calculations on such weakly bonded species huge computational resources must be employed, or an alternative, more efficient but still highly accurate methodology must be found. The *ab initio* work presented here suggests such an alternative.

There have been many studies of metal containing free radicals in the gas phase over many years by a variety of techniques. A summary of all the findings for short-lived diatomic molecules up to the mid 1970's can be found in a comprehensive review by Huber and Herzberg.[8] Much of the early work on metal containing free radicals was performed using flame studies, flash photolysis, shock tubes or arc techniques. However in 1975 the introduction of the Broida oven provided a more convenient technique for preparing metal containing diatomics. Much more recently laser ablation has been used.

Recently there have been a number of comprehensive reviews on the work performed on metal containing free radicals[9-15] to which the interested reader is referred. The focus of the work presented in this thesis is on group 2 metal containing radicals of the form ML where M is a metal and L an organic ligand. Therefore below is a very brief summary of some of the previous work on this type of species. Some of the first studies on the alkaline earth monohydroxides using a Broida oven were carried out by Harris *et al.*[16-18] The spectra were highly congested due to the high internal temperatures generated by the Broida oven and therefore detailed assignment of the spectra was not possible. The early work by Harris and

co-workers using the Broida oven was built upon by Bernath *et al.*, who have made detailed and extensive studies of the group 2 polyatomic molecules, including species such as MOH, MCH_3, MNC and MNH_2.[13]

Laser ablation is a much more convenient method of forming metal-containing free radicals. High boiling point metals can be ablated as easily as lower boiling point metals using a focused laser beam. Also laser ablation can be readily combined with a supersonic jet nozzle, allowing species to be produced with far lower temperatures than is possible with a Broida oven. Far more information can be extracted from the better resolved spectra that result. Whitham *et al.* were the first to employ this technique to study alkaline earth ML type molecules. They recorded the spectra of a series of calcium radicals, CaOH, CaCCH, $CaNH_2$ and CaCN.[19]

Metal containing free radicals have also been investigated by combining laser ablation with supersonic cooling. Ellis and co-workers have investigated a wide range of species using these techniques such as MgCCH,[12,20,21] $MgC_5H_4CH_3$ and MgC_4H_4N,[22] CaNC,[11,23] SrOH,[9,24] SrNC,[11,23] SrCCH[11,25] and BaOH.[9,21,26] Some work on the group 2 metal containing radicals has also be done by Brown *et al.*, with investigations of radicals such as $CaOCH_3$,[27] and in collaboration with Steimle, CaCl and SrF.[28] Steimle has performed many studies on radicals involving the group 2 metals, mainly with laser electronic and microwave spectroscopies. Steimle have also employed Stark spectroscopy to determine dipole moments of small metal-containing molecules. Examples of species that Steimle and co-workers have studied include, MgNC and MgCN,[29,30] $CaOCH_3$,[31] $CaCH_3$,[32] $CaNH_2$,[33] CaCCH,[34] CaNC and CaCN,[35-39] CaSH,[40] CaOH,[41-43] CaH,[44] SrOH[42,45] and SrH.[44] Coxon *et al.* have investigated the Renner-Teller effect with high resolution

electronic spectroscopy in the same types of species, such as CaCCH,[46,47] CaOH[48,49] and SrOH.[50]

There are observations of metal containing free radicals in a rare gas matrix, but they have been detected mainly by spectroscopic techniques other than LIF. For a comprehensive review of metal-containing intermediates in matrices the interested reader should consult reference (51) for IR studies, (52,53) for ESR studies, and (5) for LIF. For example, the CaCl radical has been observed in a matrix. However this was observed by Guo *et al.*[54] by chemiluminescence and not LIF. A number of electronic states were identified, but the number of different electronic and vibrational energy levels that are accessible via chemiluminescence is of course limited by the states that are excited via the reaction(s) used.

McKinley *et al.* observed $MgCH_3$ in various isotopic forms in a neon matrix via ESR spectroscopy. The assignments of the spectra acquired were aided by *ab initio* calculations. Due to the relatively large number of electrons in $MgCH_3$ only relatively undemanding calculations could be used. A model of the bonding in the $MgCH_3$ radical was determined, and this was in turn compared to other related radicals such as MgH, MgOH, $CdCH_3$, $ZnCH_3$ and $BaCH_3$.

$GaCH_3$ has been observed by Pollard *et al.*[51] via FTIR in an argon matrix, and by A. J. Downs *et al.*[55,56] Pollard *et al.* identified two of the ground state vibrational frequencies of $GaCH_3$. *Ab initio* calculations were performed to aid in interpretation and to predict the likely positions of the other ground state vibrational frequencies.

1.2.4 Ab initio calculations on weakly bonded complexes.

Performing meaningful *ab initio* calculations on species bound only by weak forces is much more challenging than for chemically bound molecules. Very accurate total energies are required to prevent huge errors in the very small binding energies calculated. The binding energy is simply

$$E_{BE} = E_{AB} - E_A - E_B \qquad (1.1)$$

where E_{BE} is the binding energy of species AB, E_{AB} is the total energy of AB, and E_A and E_B are the total energies of fragments A and B, respectively. The accuracy with which binding energies and potential energy surfaces can be calculated for weakly bound molecules has increased over time, mainly due to the increase in computing power available. New methods (*e.g.* coupled cluster method) and improved basis sets have also played a role.

The noble gas dimers are classic van der Waals complexes. Calculations on these dimers have been included in this work. A brief summary of the previous work on the three homonuclear dimers included in this work goes some way to representing the advances that have been made over the years toward accurately calculating binding energies of weakly bound molecules.

Ab initio calculations on noble gases have been performed for many years. The first reported calculations on He dimer were in 1928 by Slater,[57] and calculations are still reported today.[58-61] An historical overview for He_2 up to 1993 has been included in the paper by Anderson and co-workers.[62] Estimates of the helium binding energy have increased over this time from approximately 6 cm^{-1} to 7.7 cm^{-1} today. The very first calculations used HF calculations with small basis

sets.[63-69] Some of the early HF calculations did yield reasonable potential wells depending on the size of the basis set used. This turned out to be fortuitous, since the basis set superposition error provided the attractive component. At the HF limit (complete basis set) He_2 is unbound because it is held together by dispersive forces, which require allowance for electron correlation. Since then the accuracy of the helium potential has been improved upon by various methods including, configuration interaction (CI), Møller-Plesset perturbation theory[70-78], quantum Monte Carlo (QMC) calculations[62,79,80] and most recently coupled cluster (CC) theory[81]. In each case (except QMC) the size of the basis set used has increased over time with the consequence of a more accurate prediction of the energy. In 1976[74,82] the effect of basis set superposition error (BSSE) was illustrated and accounted for for the first time.

More recently there has been several very accurate calculations on He_2, although there is currently still some uncertainty as to the exact binding energy. A number of authors[83-85] have agreed on the value of 7.65 cm^{-1}, although the value of 7.69 cm^{-1} has also been proposed.[86,87] Indeed the accuracy of *ab initio* calculations on He_2 is approaching $\pm$ 0.01 cm^{-1}, an accuracy that Aziz *et al.*[88] have shown to be sufficient to calibrate laboratory apparatus that measure transport properties. Finally and most recently, van Mourik and Dunning[61] have used CC theory with full inclusion of triple excitations (CCSDT) to provide what may be the most accurate estimate yet for the binding energy of helium dimer.

The larger number of electrons in neon and argon dimers compared to helium makes them more demanding computationally and hence the accuracy for these two dimers has tended to lag behind that of helium. Previous calculations have shown that larger basis sets, including considerably higher polarization functions than

employed for He_2 are required for calculations on neon and argon. Most recently van Mourik *et al.*[60] and Cybulski *et al.*[59] have reported some of the most accurate estimates of the Ne_2 binding energy. Van Mourik *et al.* have used a variety of methods, but their most accurate potential used CCSD(T) with the very large d-aug-cc-pV6Z basis set that includes two sets of diffuse functions and i-type polarization functions. This yielded a binding energy of 28.31 cm^{-1}. Cybulski *et al.*[59] also used CCSD(T) with a very large basis set, aug-cc-pV5Z with an additional set of bond functions (3s3p2d2f1g). Bond functions are not centred on an atom but placed on the bond between the two atoms to improve the description of this important area. This approach yielded a value for the neon binding energy of 28.6 cm^{-1}, which is quite similar to the van Mourik *et al.* study. In comparison to these two studies, Aziz *et al.*[89] reported a semi-empirical study that yielded a value of 29.4 cm^{-1}. Recently there have also been a number of other semi-empirical and *ab initio* studies using a variety of less accurate methods and smaller basis sets.[90-94]

Calculations on Ar_2 have historically tended to underestimate the well depth due to a lack of higher order functions in the basis set. For example the MP4 calculations of Chalasinski *et al.*[95] performed in 1987 with a relatively small basis set, underestimate the binding energy by approximately 25 %. Only a small number of studies have successfully estimated the well depth to within 90 % of the experimental value (99.5 cm^{-1} [96,97]). Tao and Pan[98] achieved approximately 92 % using MP4 and a large basis set with additional bond functions. Two further works by Woon[99] and by van Mourik *et al.*[60] estimate 94.4 and 96.2 cm^{-1} respectively. Both studies use CCSD(T) and the largest available augmented correlation consistent basis sets. The most recent study on argon dimer is by Cybulski *et al.*[59] using

CCSD(T) and the aug-cc-pV5Z basis set with a large set of additional bond functions predicts a well depth of approximately 97 cm^{-1}.

This brief review of the past work on the noble gas dimers highlights the difficulty in performing accurate calculations on van der Waals species. The weak interaction between the species necessitates the use of both a large flexible basis set and method that recovers a large proportion of the electron correlation energy. In addition to this the basis set superposition energy must also be corrected for. Even for the small clusters discussed above this can make meaningful calculations exceedingly expensive.

Extrapolation schemes offer an alternative to large basis sets to estimate the complete basis set (CBS) limit. The results of calculations performed using a sequence of calculations employing increasingly larger basis sets, can be extrapolated to estimate the CBS limit. A discussion of extrapolation schemes is given in Chapter 5. However extrapolation schemes themselves can be problematic. One of the difficulties with extrapolations is the slow convergence with basis set size, meaning that large basis sets calculations are often required for a useful extrapolation. This problem is exacerbated for van der Waals clusters because additional functions must be included in the basis set to account for the long-range attractive forces. Thus an expensive set of calculations is often required before the extrapolation can be performed. In contrast to this, an extrapolation scheme is presented in Chapter 5 that makes use of relatively small basis sets to estimate the CBS limit. This extrapolation scheme (the modified Truhlar extrapolation) is applied to van der Waals clusters.

1.3 OUTLINE OF THIS THESIS

Chapter 2 provides a brief introduction to the experimental apparatus and techniques used in the gas phase laser spectroscopy carried out in this work. The explanation is biased toward the observation of BaOH, which is discussed in Chapter 3. A brief introduction to the theory behind *ab initio* calculations on small atoms or molecules is provided in Chapter 4. In Chapter 5 a new extrapolation technique for *ab initio* calculations (the modified Truhlar extrapolation) is described and the results of calculations on rare gas complexes and related species with well known binding energies are presented. The calculations allow the performance of the modified Truhlar extrapolation to be assessed. The modified Truhlar extrapolation is also used in Chapter 6 to produce the most accurate and detailed set of calculations on the HRgF series of molecules yet reported (where Rg = He, Ne or Ar). Partial potential energy surfaces have been mapped out and vibrational frequencies calculated. More calculations have been performed with the modified Truhlar extrapolation in Chapter 7. The previously uninvestigated RgCC series of complexes (where Rg = He, Ne or Ar) has been investigated. Potential energy surfaces and vibrational frequency calculations have again been performed. Finally, Chapter 8 describes the development of a new matrix isolation rig for the observation of free radicals trapped in inert matrices by laser spectroscopy.

1.4 REFERENCES

1. J. M. Hollas, *Modern spectroscopy*, (1996) Wiley.
2. A. Kantrowitz and J. Grey, *Rev. Sci. Instr.*, **22** (1951) 328
3. V. E. Bondybey and L. E. Brus, *Adv. Chem. Phys.*, **41** (1980) 269.
4. S. Cradock and A. J. Hinchcliffe, *Matrix Isolation*, Cambridge University Press, 1975.
5. V. E. Bondybey, A. M. Smith and J. Agreiter, *Chem. Rev.*, **96** (1996) 2113.
6. W. E. Moerner and T. Basche, *Angew. Chem.*, **32** (1993) 457.
7. W. E. Moerner, *Science*, **265** (1994) 46.
8. K. P. Huber and G. Herzberg, *Molecular spectra and molecular structure. IV. Constants of diatomic molecules.* (1979) Van Nostrand Reinhold.
9. M. S. Beardah, *PhD thesis* (1999), University of Leicester.
10. A. M. Beardah, *PhD thesis* (1999), University of Leicester.
11. G. M. Greetham, *PhD thesis* (2000), University of Leicester.
12. G. K. Corlett, *PhD thesis* (1997), University of Leicester.
13. P. F. Bernath, *Science*, **254** (1991) 665.
14. A. M. Ellis, *Int. Rev. Phys. Chem.* **20** (2001) 551.
15. A. M. Ellis, E. S. J. Robles and T. A. Miller, *J. Phys. Chem.* **97** (1993) 5809.
16. R. F. Wormsbecher, M. Trkula, C. Martner, R. E. Penn and D. O. Harris, *J. Mol. Spec.*, **97** (1983) 29.
17. R. C. Hilborn, Q. Zhu and D. O. Harris, *J. Mol. Spec.*, **97** (1983) 73.
18 J. Hakagawa, R. F. Wormsbecher and D. O. Harris, *J. Mol. Spec.*, **97** (1983) 37.
19. C. J. Whitham, B. Soep, J-P. Visticot and A. Keller, *J. Chem. Phys.*, **93** (1990) 991.

20. G. K. Corlett, A. M. Little and A. M. Ellis, *Chem. Phys. Lett.*, **249** (1996) 53.

21. M. S. Beardah and A. M. Ellis, *J. Chem. Phys.*, **74** (1999) 863.

22. E. S. J. Robles, A. M. Ellis and T. A. Miller, *J. Phys. Chem.*, **96** (1992) 8791.

23. G. M. Greetham and A. M. Ellis, *J. Chem. Phys.*, **113** (2000) 8945.

24. M. S. Beardah and A. M. Ellis, *J. Chem. Phys.*, **110** (1999) 11244.

25. G. M. Greetham and A. M. Ellis, *J. Mol. Spec.*, **206** (2001) 198.

26. S. J. Pooley, M. S. Beardah and A. M. Ellis, *J. Elec. Spec. Rel. Phen.*, **97** (1998) 77.

27. C. J. Whitham, S. A. Beaton, Y. Ito and J. M. Brown, *J. Mol. Spec.*, **191** (1998) 286.

28. J. M. Brown, D. J. Milton and T. C. Steimle, *Faraday Discuss.*, **71** (1981) 151.

29. T. C. Steimle and R. R. Bousquet, *J. Chem. Phys.*, **115** (2001) 5203.

30. M. A. Anderson, T. C. Steimle and L. M. Ziurys, *Astrophys. J.*, **429** (1994) 41.

31. K. C. Namiki, J. S. Robinson and T. C. Steimle, *J. Chem. Phys.*, **109** (1998) 5283.

32. A. J. Marr, F. Grieman and T. C. Steimle, *J. Chem. Phys.*, **105** (1996) 3930.

33. A. J. Marr, M. Tanimoto, D. Goodridge and T. C. Steimle, *J. Chem. Phys.*, **103** (1995) 4466.

34. A. J. Marr, J. Perry and T. C. Steimle, *J. Chem. Phys.*, **103** (1995) 3861.

35. C. T. Scurlock, R. D. Suenram and F. J. Lovas, *J. Chem. Phys.*, **100** (1994) 3497.

36. T. C. Steimle, D. A. Fletcher, K. Y. Jung and C. T. Scurlock, *J. Chem. Phys.*, **100** (1994) 4025.

37. T. C. Steimle, S. Saito and S. Takano, *Astrophys. J*, **410** (1993) 49.

38. T. C. Steimle, D. A. Fletcher, K. Y. Jung and C. T. Scurlock, *J. Chem. Phys.*, **97** (1992) 2909.

39. C. T. Scurlock, D. A. Fletcher and T. C. Steimle, *J. Chem. Phys.*, **101** (1994) 7255.

40. C. T. Scurlock, T. Henderson, S. Bosely, K. Y. Jung and T. C. Steimle, *J. Chem. Phys.*, **100** (1994) 5481.

41. C. T. Scurlock, D. A. Fletcher and T. C. Steimle, *J. Mol. Spec.*, **159** (1993) 350.

42. T. C. Steimle, D.A. Fletcher, K. Y. Jung and C. T. Scurlock, *J. Chem. Phys.* **96** (1992) 2556.

43. C. W. Bauschlicher, C. R. Langhoff, T. C. Steimle and J. E. Shirley, *J. Chem. Phys.*, **93** (1990) 4179.

44. T. C. Steimle, T. P. Meyer, Y. Alaramadin and P. Bernath, *J. Mol. Spec.*, **125** (1987) 225.

45. D. A. Fletcher, K. Y. Jung, C. T. Scurlock and T. C. Steimle, *J. Chem. Phys.*, **98** (1993) 1837.

46. M. G. Li and J. A. Coxon, *J. Mol. Spec.*, **180** (1996) 287.

47. M. G. Li and J. A. Coxon, *J. Mol. Spec.*, **176** (1996) 206.

48. M. G. Li and J. A. Coxon, *Can. J. Phys.*, **72** (1994) 1200.

49. M. G. Li and J. A. Coxon, *J. Chem. Phys.*, **102** (1995) 2663.

50. P. I. Presunka and J. A. Coxon, *Chem. Phys.*, **190** (1995) 97.

51. B. J. Pollard, *PhD thesis* (1999), University of Leicester.

52. A. P. Williams, R. J. Van Zee and W. Weltner, *J. Am. Chem. Soc.*, **118** (1996) 4498.

53. L. B. Knight, B. Gregory, J. Cleveland and C. A. Arrington, *Chem. Phys. Letts.*, **204** (1993) 168.

54. S. W. Guo, J. W. Chang and Y. P. Lee, *J. Chin. Chem. Soc.*, **32** (1985) 215.

55. H. J. Himmel, A. J. Downs, T. M. Greene and L. Andrews, *Organometallics*, **19** (2000) 1060.

56. H. J. Himmel, A. J. Downs, T. M. Greene and L. Andrews, *Chem. Comm.*, **22** (1999) 2243.

57. J. C. Slater, *Phys. Rev.*, **32** (1928) 349.

58. R. Specchio, A. Famulari and M. Raimondi, *J. Molec. Struc.*, **549** (2001) 77.

59. S. M. Cybulski and R. F. Toczylowski, *J. Chem. Phys.*, **111** (1999) 10520.

60. T. V. Mourik, A. K. Wilson and T. H. Dunning, *Molec. Phys.*, **96** (1999) 529.

61. T. van Mourik and T. H. Dunning, *J. Chem. Phys.*, **111** (1999) 9248.

62. J. B. Anderson, C. A. Traynor and B. M. Boghosian, *J. Chem. Phys.*, **99** (1993) 345.

63. G. Gentile, *Z Phys.*, **63** (1930) 795.

64. H. Margenau, *Phys. Rev.*, **56** (1939) 1000.

65. V. Griffing and J. F. Wehner, *J. Chem Phys.*, **23** (1955) 1024.

66. M. Sakamoto and E. Ishiguro, *Prog. Theor. Phys. (Japan)*, **15** (1956) 37.

67. S. Huzinaga, *Prog. Theor. Phys. (Japan)*, **17** (1957) 512.

68 S. Huzinaga, *Prog. Theor. Phys. (Japan)*, **18** (1957) 139.

69. T. Hashino and S Huzinaga, *Prog. Theor. Phys. (Japan)*, **20** (1958) 201.

70. N. Lynn, *Proc. Phys. Soc.*, **72** (1958) 201.

71. P. E. Phillipson, *Phys Rev.*, **125** (1962) 1981.

72. N. R. Kestner, *J. Chem. Phys.*, **48** (1968) 252.

73. P. J. Bertoncini and A. C. Wahl, *Phys. Rev Lett.*, **25** (1970) 991.

74. P. D. Dacre, *Chem. Phys. Lett.*, **50** (1977) 147.

75. J. Sauer, P. Hobza, P. Carsky and R. Zahradnik, *Chem. Phys. Lett.*, **134** (1987) 553.

76. G. Chalasinski and M. M. Szczesniak, *Mol. Phys.* **63** (1988) 205.

77. J. H. V. Lenthe, R. J. Vos, J. G. C. M. van Duijneveldt van-de Rijdt and F. B. van Dunijneveldt, *Chem. Phys. Lett.*, **143** (1988) 435.

78. F. Tao and Y. Pan, *J. Chem. Phys.* **97** (1992) 4989.

79. D. M. Ceperley and H Partridge, *J. Chem. Phys.*, **84** (1986) 820.

80. R. L. Coldwell and R. E. Lowther, *Int. J. Quant. Chem. Symp.*, **12** (1978) 329.

81. S. Rybak, K. Szalewicz, B. Jeziorski and M. Jaszunski, *J. Chem. Phys.*, **86** (1987) 5652.

82. N. S. Ostlund and D. L. Merrifield, *Chem. Phys. Lett.*, **39** (1976) 612.

83. W. Klopper and J. Noga, *J. Chem. Phys.*, **103** (1995) 6127.

84. R. Bukowski, B. Jeziorski and K. Szalewicz, *J. Chem. Phys.*, **104** (1996) 3306.

85. T. van Mourik, R. J. Vos, J. H. van Lenthe and van Duijneveldt., *Intl. J. Quantum Chem.*, **63** (1997) 806.

86. T. Korona, H. Williams, R. Bukowski, B. Jeziorski and K. Szalewicz, *J. Chem. Phys.*, **106** (1997) 5109.

87. A. R. Janzen and R. A. Aziz, *J. Chem. Phys.*, **107** (1997) 914.

88. R. A. Aziz, A. R. Janzen and M. R. Moldover., *Phys. Rev. Lett.*, **74** (1995) 1586.

89. R. A. Aziz and M. J. Slaman, *Chem. Phys.*, **130** (1989) 187.

90. R. A. Aziz, W. J. Meath and A. R. Allnatt., *Chem. Phys.*, **78** (1983) 295.

91. F. M. Tao and Y. K. Pan, *Chem. Phys. Lett.*, **194** (1992) 162.

92. R. Eggenberger, S. Gerber, H. Huber and D. Searles, *J. Chem. Phys.*, **96** (1992) 6104.

93. F. M. Tao and Y. K. Pan., *J. Phys. Chem.*, **96** (1992) 6105

94. F. M. Tao and Y. K. Pan., *J. Phys. Chem.*, **95** (1991) 9811.

95. G. Chalasinski, D. J. Funk, J. Simons and W. H. Breckenridge. *J. Chem. Phys.*, **87** (1987) 3569.

96. P. R. Herman, P. E. LaRocque and B. P. Stoicheff, *J. Chem. Phys.*, **89** (1988) 4535.

97. R.A. Aziz, *J. Chem. Phys.*, **99** (1993) 4518.

98. F. M. Tao and Y. K. Pan, *Molec. Phys.*, **81** (1994) 507.

99. D. E. Woon, *J. Chem. Phys.*, **100** (1994) 2838.

CHAPTER 2

Experimental

2. EXPERIMENTAL

2.1 INTRODUCTION

The experimental apparatus and procedure used to observe BaOH (Chapter 3) is described briefly below. This is essentially an abridged version of more detailed accounts given in previous PhD theses from the University of Leicester spectroscopy group, and so for a more detailed description the reader is referred to those earlier publications.[1-3] Many of the processes and much of the apparatus described here is also relevant to the matrix isolation experiments described in Chapter 8. The specific experimental arrangement and procedure for the matrix isolation work is described separately in Chapter 8.

2.2 EXPERIMENTAL DETAILS

2.2.1 Overview

Figure 2.1 provides an outline diagram of the main features of the gas phase laser spectroscopy apparatus.[1-5] A brief overview of the experimental procedure is given here before parts are discussed in more detail. The heart of the apparatus is the vacuum chamber, where the molecules (usually free radicals) to be investigated are produced, and observed via laser spectroscopy.

Metal-containing free radicals were produced by laser ablation of a metal target by a pulsed excimer laser and simultaneous photolysis of an organic precursor by the same excimer laser. These free radicals were entrained in a high pressure inert carrier gas and expanded through a nozzle into a vacuum chamber to yield a supersonic jet. Downstream of the nozzle the jet is intersected by a tuneable dye laser beam. The dye laser may excite species within the jet of gas, and in turn these

excited species may fluoresce at a characteristic wavelength. A photomultiplier tube (PMT) attached to the vacuum chamber will detect the fluorescence emitted. This PMT signal is recorded by a PC and, by tuning the wavelength, a spectrum is ultimately generated.

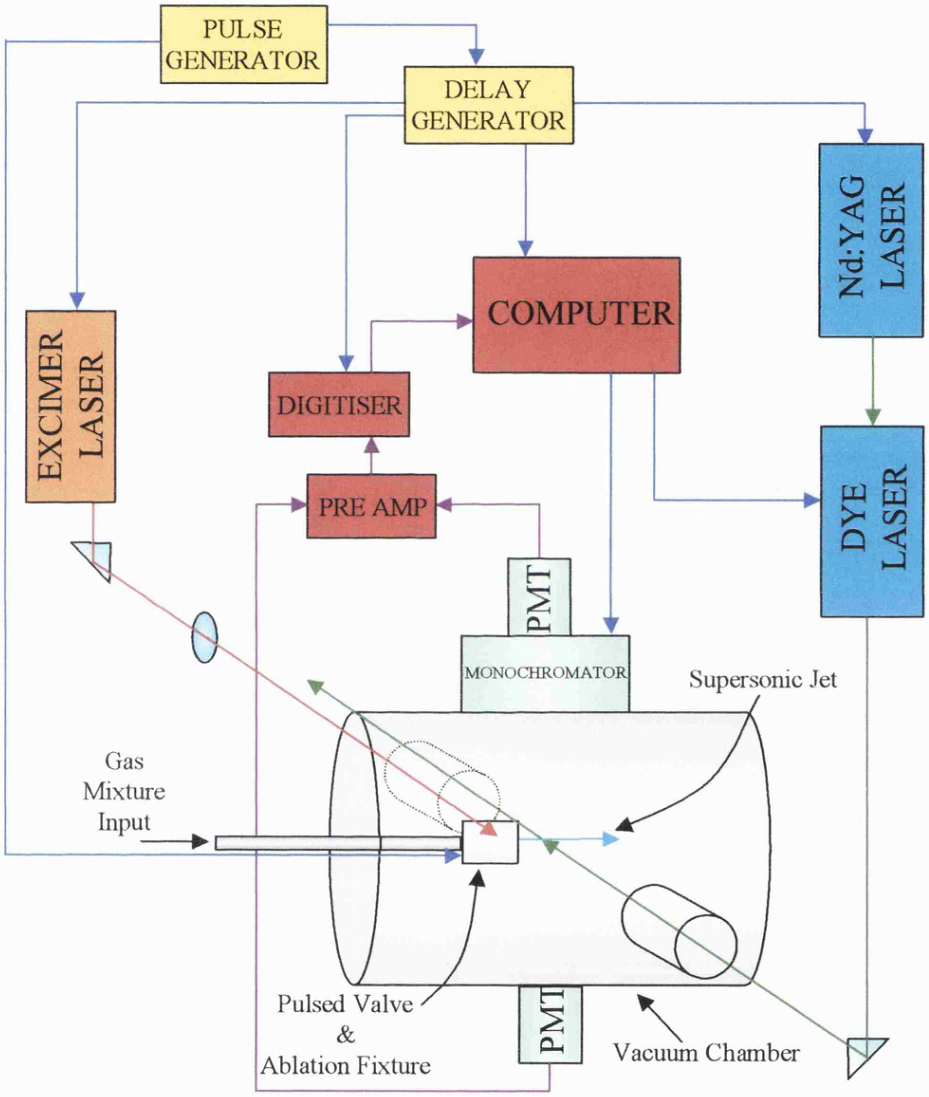

Figure 2.1. Schematic diagram of the laboratory layout for gas phase experiments.

2.2.2 Radical production

Metal-containing free radicals are very short lived under normal laboratory conditions. Thus in order to perform spectroscopy on such species it is necessary to create a situation in which they survive long enough to enable spectroscopy to be performed.

In the specific case of BaOH,[6] laser ablation is employed to produce Ba atoms. To generate OH, hydrogen peroxide vapour is used as the precursor. BaOH could be formed by direct reaction of photolytically generated OH or, conceivably, by reaction between electronically excited Ba and H_2O_2.

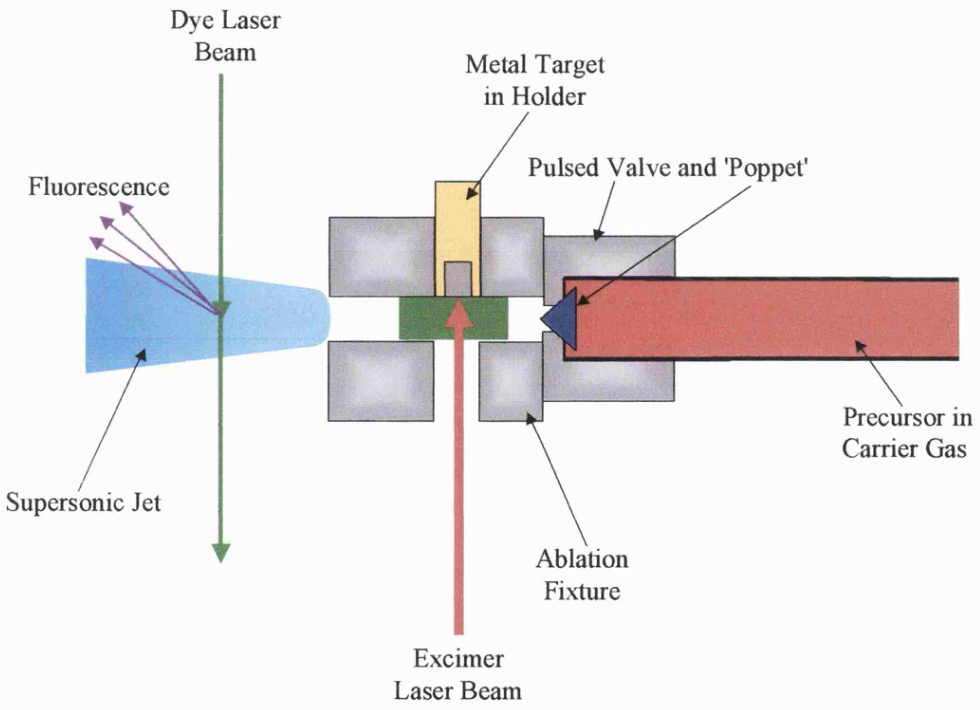

Figure 2.2. Schematic diagram of ablation fixture showing the progress of the gas through the fixture (red to green to blue).

The specific experimental arrangement for the radical source is shown in Figure 2.2. The chemistry takes place in an aluminium 'ablation fixture', which is attached to a pulsed valve. A mixture of H_2O_2 vapour and inert gas, usually at a total gas pressure of several bar, is supplied to the pulsed valve. The valve is opened for a

short period of time (~500 μs) to allow a slug of gas to into the ablation fixture, where it flows over the surface of a solid barium target.

Laser ablation is achieved by the use of an excimer laser operating with either ArF (193 nm) or KrF (248 nm) fills; both were employed in the BaOH experiments, although primarily ArF was used. The excimer laser pulse was focused on to the metal sample and timed to coincide with the arrival of the pulse of gas emitted from the pulsed valve. Due to barium being relatively soft and easy to vaporise, the excimer beam was softly focused onto the metal at a relatively low beam pulse energy (20-70 mJ/pulse). The laser pulse simultaneously ablates the surface of the metal target generating metal atoms AND can photolyse the precursor molecule to produce reactive fragments.[7] A plethora of chemical species will be produced in the ablation/photolysis process and indeed this is the primary advantage of this type of source. However with a barium target and hydrogen peroxide of the more abundant species is likely to be BaOH. Importantly a major dissociation channel of H_2O_2 upon photolysis by an ArF excimer laser is to form OH radicals by fission of the O-O bond.[8]

The gas mixture consists of a precursor and a carrier gas. The carrier gas, at high pressure (several bar), transports the precursor from a sample bomb to the metal target. The proportion of precursor in the gas mixture is important. This can be controlled by heating or cooling of the sample bomb. A typical H_2O_2/carrier gas ratio employed was 1:1000.

2.2.3 Supersonic jet expansion

Once the radicals have been formed the pulse of gas is emitted from the ablation fixture into the vacuum chamber and forms a supersonic jet. The supersonic jet has

two properties that are important for these experiments. Firstly it provides a nearly collisionless environment, which prevents the radicals reacting further. Secondly, it vibrationally and rotationally cools the radicals. Vibrational and rotational cooling of the target species is important as cooler molecules produce simplified spectra compared with room temperature samples, which significantly aids interpretation. With a reasonably high backing pressure the rotational temperature will fall to ≤ 10 K after only ~10 nozzle diameters.[9]

2.3 LASER INDUCED FLUORESCENCE SPECTROSCOPY

Laser induced fluorescence spectroscopy was performed on the radicals present in the supersonic jet by crossing it with a tuneable dye laser beam. At resonant wavelengths the dye laser beam can electronically excite molecules within the jet, and subsequently these may relax down to a lower energy state by emitting a photon (fluorescing). There are various non-radiative processes that compete with fluorescence, such as internal conversion, intersystem crossing, predissociation and collisional relaxation (limited in a supersonic jet). In many relaxation schemes both radiative and non-radiative processors occur in sequence to allow the excited species to relax down to its ground state.[10-12]

2.3.1 Excitation spectroscopy

The principles of excitation spectroscopy are illustrated in Figure 2.3. The dye laser wavelength is scanned and, when resonant with a transition in the atom or molecule, excitation occurs to an excited energy level. To detect the occurrence of absorption, the total fluorescence (or a subset of the total fluorescence) is detected. [4,13]

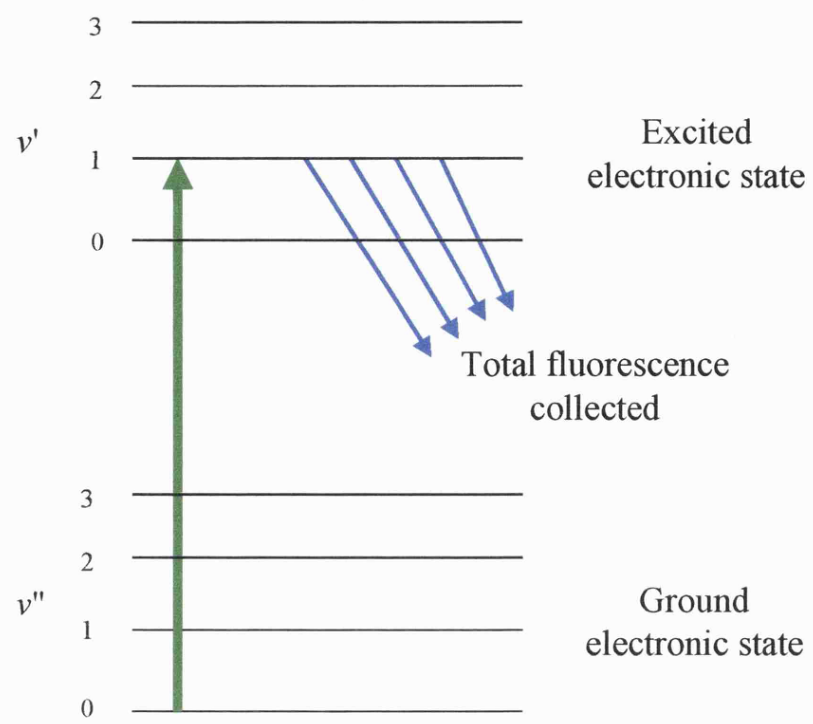

Figure 2.3 Diagram illustrating laser-induced fluorescence excitation spectroscopy. The excitation laser wavelength is scanned and when absorption occurs this is detected by monitoring fluorescence.

A fluorescence excitation spectrum therefore consists of a plot of the intensity of fluorescence versus the laser wavelength. The information obtained is equivalent to that which would be obtained from a conventional absorption spectrum, although the fluorescence excitation spectrum also depends on the fluorescence quantum yield of the excited state. LIF is much more sensitive than a conventional absorption experiment because the signal collected is compared to a background that is close to zero and therefore the signal to noise ratio is much larger. Filtering of the light prior to detection can dramatically increase the signal to noise ratio in an LIF spectrum by removing scattered laser light.

The spectral resolution in excitation spectroscopy is determined by several factors. One factor is the dye laser linewidth.[14,15] In the BaOH work a Sirah Cobra Stretch dye laser was employed with a linewidth of 0.075 cm^{-1}.[16] This is sufficient

for many small molecules to achieve at least partial rotational resolution. For the matrix isolation work discussed in Chapter 8 a different dye laser was used, a Lambda Physik Scanmate with a linewidth of 0.3 cm^{-1}.

The resolution achieved in a spectrum is dependent upon other factors as well as the laser linewidth.[10,11] Doppler broadening is significantly reduced in the supersonic jet compared with normal gases because the molecules within the jet are all moving at a narrow range of speeds and approximately in the same direction (orthogonal to the laser beam). Pressure broadening is also significantly reduced by the supersonic jet because the molecules are in an almost collisionless expansion where the dye laser beam crosses. The natural linewidth, will of course, be present. However the largest effect on the spectral resolution in this type of experiment (depending on the laser linewidth) is often power broadening. In the BaOH experiments a very low laser intensity was required to reduce power broadening effect down to an acceptable level.

2.3.2 Dispersed fluorescence spectroscopy

In dispersed fluorescence spectroscopy (see figure 2.4) the laser wavelength is fixed at a value that is known to correspond to a transition in the desired species.[4, 13] A specific excited state is populated by this process and the spectrum of the fluorescence subsequently produced is recorded. This yields an emission spectrum from a specific excited state. One way of obtaining such a spectrum, a dispersed fluorescence spectrum, is to use a scanning monochromator. The resulting plot of fluorescence intensity versus observed wavelength provides information on the lower (often ground) state of the molecule, the state to which the molecule relaxes by emission.

The resolution in the dispersed fluorescence experiments was limited by the monochromator. The monochromator used in this work was an Acton research SpectraPro 275, with 0.3 m optical path length. The best resolution was 0.1 nm. However, for acceptable entrance and exit slit sizes (adjustable) the actual resolution was worse, typically 0.25-0.5 nm in the work reported in this thesis.

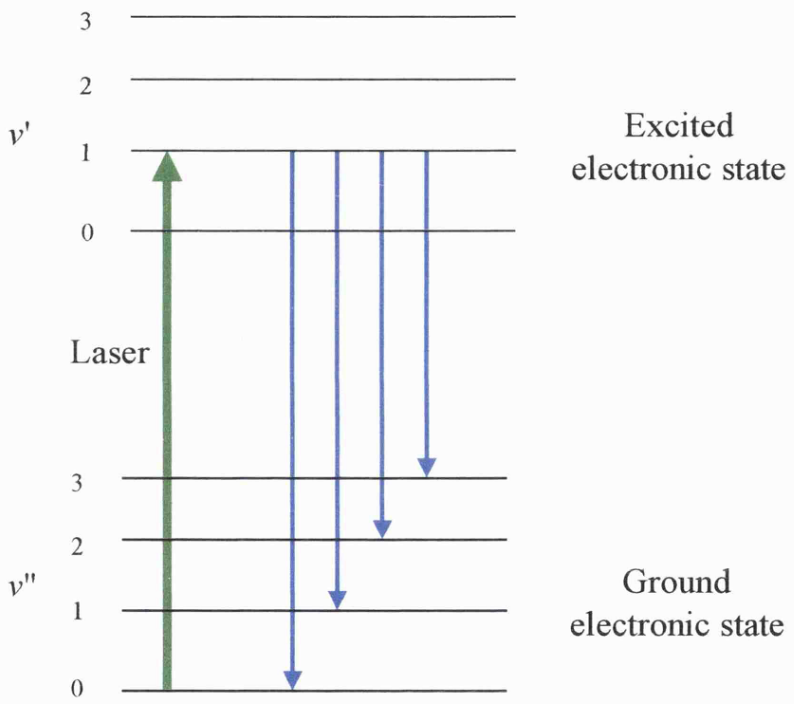

Figure 2.4 Diagram illustrating dispersed fluorescence spectroscopy.

2.3.3 Detection

The pulsed nature of the experiments causes complications associated with synchronisation of the gas and laser pulses. The timing of all the pulsed aspects of

the experiment must be controlled very precisely. The relative timing sequence for a typical experiment is shown in Figure 2.5.

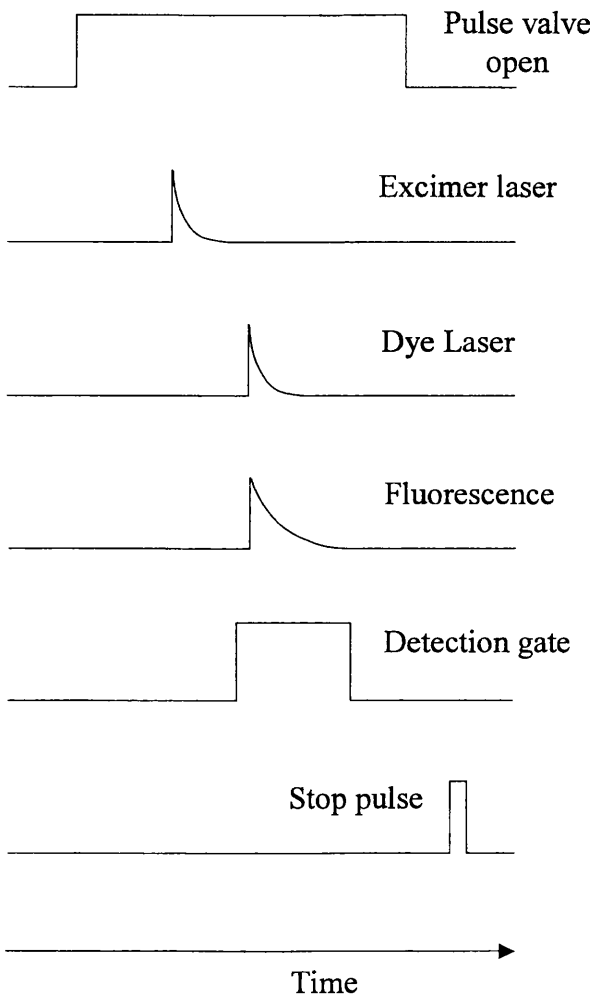

Figure 2.5. Timing sequence (not to scale) used in the gas phase laser spectroscopy experiments. See text for details.

The pulsed valve is usually opened for ~500 μs. The excimer laser pulse is timed to fire when the middle portion of the slug of gas from the valve passes over the metal target. After a suitable delay to allow the gas mixture to leave the ablation fixture and expand into vacuum, the dye laser is fired.

The detection gate shown in figure 2.5 indicates the period of time chosen during each pulse sequence in which signals from the PMT are stored on the PC. By

a judicious choice of gate position and length, a suitable portion of the fluorescence decay curve can be selected for recording. The gate in the figure 2.5 has been chosen to encompass all of the fluorescence, although this need not be the case. Sometimes, if multiple species are fluorescing, a narrower gate appropriately placed may bias the signal from one species at the expense of another. Finally a stop pulse is provided to indicate to the computer the end of the timing sequence. The whole sequence is repeated at a set rate, usually 10 Hz.

The signal from the PMT is amplified and digitised before being fed into the PC. Using software written in-house, the fluorescence signal is integrated within the chosen detection gate on a shot-by-shot basis. To construct an actual spectrum, the signal is averaged over a number of shots at each wavelength position, typically 15-40 shots, to improve the signal to noise ratio. To construct a spectrum the laser (or monochromator) is then stepped to another wavelength and the whole process is repeated until the desired wavelength range has been covered.

2.4 REFERENCES

1. M. S. Beardah, *PhD thesis* (1999), University of Leicester.
2. A. M. Beardah, *PhD thesis* (1999), University of Leicester.
3. G. M. Greetham, *PhD thesis* (2000), University of Leicester.
4. D. H. Levy, *Ann. Rev. Phys. Chem.*, **31** (1980) 197.
5. M. S. Beardah, A. M. Ellis, *J. Chem. Technol. Biotechnol.* **74** (1999) 863.
6. S. J. Pooley, M. S. Beardah and A. M. Ellis, *J. Elec. Spec. Rel. Phen.* **97** (1998) 77.
7. M. F. Cai, T. A. Miller and V. E. Bondybey, *Chem. Phys. Lett.*, **158** (1989) 475.
8. A. Schiffman, D. D. Nelson, D. J. Nesbitt, *J. Chem. Phys.* **98** (1993) 6935.
9. T. A. Miller, *Science*, **223** (1984) 545.
10. J. M. Hollas, Modern spectroscopy, (1996) Wiley.
11. J. M. Hollas, High resolution spectroscopy, (1982) Butterworth.
12. P. W. Atkins, Physical Chemistry, (1994) Oxford University Press.
13. J. L. Kinsey, *Ann. Rev. Phys. Chem.*, **28** (1977) 349.
14. J. Hecht, *Lasers and Applications*, **July** (1984) 53.
15. T. F. Johnston, *Ency. Phys. Sci. Tech.*, **14** (1987) 96.
16. Sirah Cobra Stretch dye laser service manual.

CHAPTER 3

Electronic Spectroscopy in the $\widetilde{C} - \widetilde{X}$ Region of BaOH

3. ELECTRONIC SPECTROSCOPY IN THE $\tilde{C}$-$\tilde{X}$ REGION OF BaOH

3.1 INTRODUCTION

The well-known green emission when barium salts are introduced into flames is the result of fluorescence from both BaO and BaOH. In the case of BaO a single electronic band system, the $A^1\Sigma^+$- $X^1\Sigma^+$ system, is responsible. The properties of these electronic states of BaO have been well established from earlier spectroscopic studies.[1] In marked contrast, the contribution from the BaOH free radical is poorly understood.

BaOH is a highly ionic molecule whose electronic structure is easily envisaged by assuming that an electron is fully transferred from the metal atom to the OH group. In the resulting Ba^+OH^- an unpaired electron remains on the barium atom and it is this electron that is involved in the lowest lying electronic transitions in this molecule. This simple picture is remarkably successful for explaining the electronic spectra of a wide variety of related alkaline earth containing molecules, such as MX (X = halide), MOH, MNC and MCH_3.[2,3]

In BaOH the four lowest energy electronic states are the $\tilde{X}^2\Sigma^+$, $\tilde{A}^2\Pi$, $\tilde{A}'^2\Delta$, and $\tilde{B}^2\Sigma^+$ states. In the $\tilde{X}^2\Sigma^+$ state the unpaired electron resides in a σ orbital which is primarily an *sp* hybrid orbital on the metal polarised away from the OH group. The three excited states are formed from the 5*d* orbitals on barium, although the $\tilde{A}^2\Pi$ and $\tilde{B}^2\Sigma^+$ states also contain a contribution from 6*p* orbitals. Transitions to these excited states from the $\tilde{X}^2\Sigma^+$ state have been reported previously, and in all three cases the spectra fall in the near infrared.[4,5]

Far less is known about the higher lying electronic states of BaOH responsible for the green emission in flames. In fact there have been only two previous studies of

electronic spectra of BaOH in the visible region. Haraguchi and co-workers applied laser-induced fluorescence (LIF) spectroscopy to barium containing flames in an effort to identify the various species present.[6] In addition to contributions from BaO, two broad bands were observed, one at approximately 19500 cm^{-1} and the other at 20500 cm^{-1}, which were attributed to BaOH. However, the resolution was poor and the assignment to BaOH could not be confirmed. More recently, Pooley, Beardah and Ellis carried out the first spectroscopic study BaOH in the visible region using a supersonically cooled sample.[7] The $\widetilde{D}^2\Sigma^+ - \widetilde{X}^2\Sigma^+$ system, which is found in the blue, was readily characterised in that work. At longer wavelengths a complex band system was discovered spanning 455-505 nm (21980-19800 cm^{-1}). This system, which peaks in the green at approximately 485 nm (20620 cm^{-1}) and is the one responsible for the flame emission, proved difficult to assign despite the dramatic improvement in resolution attained from jet-cooling. Nevertheless, tentative vibrational assignments were proposed. Furthermore, on the basis of rotational contours of the strongest bands in the excitation spectrum, it was suggested that two electronic transitions, both $\widetilde{C}\,^2\Pi$- $\widetilde{X}\,^2\Sigma^+$, were responsible for many of the features. Unfortunately, in that earlier work the spectral resolution was insufficient to confirm or disprove these assignments. In addition, many medium intensity and weak bands were ignored.

This study is concerned with a more detailed investigation of the green system of BaOH, including higher resolution scans of many bands. The earlier suggestion that $\widetilde{C}\,^2\Pi$- $\widetilde{X}\,^2\Sigma^+$ transitions form the basis of the observed structure is shown to be correct, although errors in the earlier assignments have been found. However, it has also been discovered that this is a remarkably complex spectral region that does not

seem to be amenable to a simple analysis. The findings from this work are presented here.

3.2 EXPERIMENTAL

A more detailed description of the experimental set up can be found in Chapter 2. Briefly, BaOH free radicals were generated in a pulsed supersonic jet by excimer laser ablation of barium in the presence of a gaseous mixture of hydrogen peroxide and argon. The stagnation pressure of the gas behind the pulsed nozzle (General Valve) was typically 10 bar. A pulsed Sirah Cobra-Stretch dye laser (0.05 cm^{-1} linewidth) pumped by a Nd:YAG laser was used for probing the radicals 20 mm downstream of the nozzle. Laser-induced fluorescence (LIF) excitation spectra were obtaining by scanning the laser wavelength and imaging the fluorescence onto a photomultiplier tube (PMT). Scattered laser light was removed using appropriate optical filters in front of the PMT.

Dispersed fluorescence (DF) spectra were obtained by exciting BaOH transitions using the amplified output of the dye laser. The fluorescence was focussed onto the entrance slits of a scanning monochromator (Acton SpectraPro 275) equipped with a PMT at the exit slit. The resolution attained in the DF experiments was ~20 cm^{-1}. Excitation and DF spectra presented in this work are typically averages of up to 50 laser shots per discrete wavelength point in a spectrum.

3.3 RESULTS AND DISCUSSION

A survey laser excitation scan covering 20300-21000 cm^{-1} is shown in Figure 3.1. This is a spectrum with much improved jet-cooling compared with the earlier study.[7] Bands attributable to BaOH have been observed outside of the region shown in

Figure 3.1 (both to the immediate red and blue). However, these additional bands are mainly weak and will be discussed later. Overall, as will be seen, the spectroscopy of BaOH in this region is complex. To keep the problem tractable, we decided to initially focus on a sub-set of bands, specifically those between 20500 and 21000 cm^{-1}. Detailed studies of the bands in this region were carried out, including dispersed fluorescence and rotationally resolved work. Thereafter, the work was broadened to include many other bands, although these were studied in less detail.

The findings from the study of the 20500-21000 cm^{-1} region are presented first. The discussion is then extended to include other bands.

Table 3.1. List of all the bands discussed in this chapter.

Band number	Position / cm^{-1}
1	19892
2	19992
3	20107
4	20179
5	20276
6	20356
7	20387
8	20467
9	20533
10	20550
11	20608
12	20931
13	20940
14	20971
15	20986

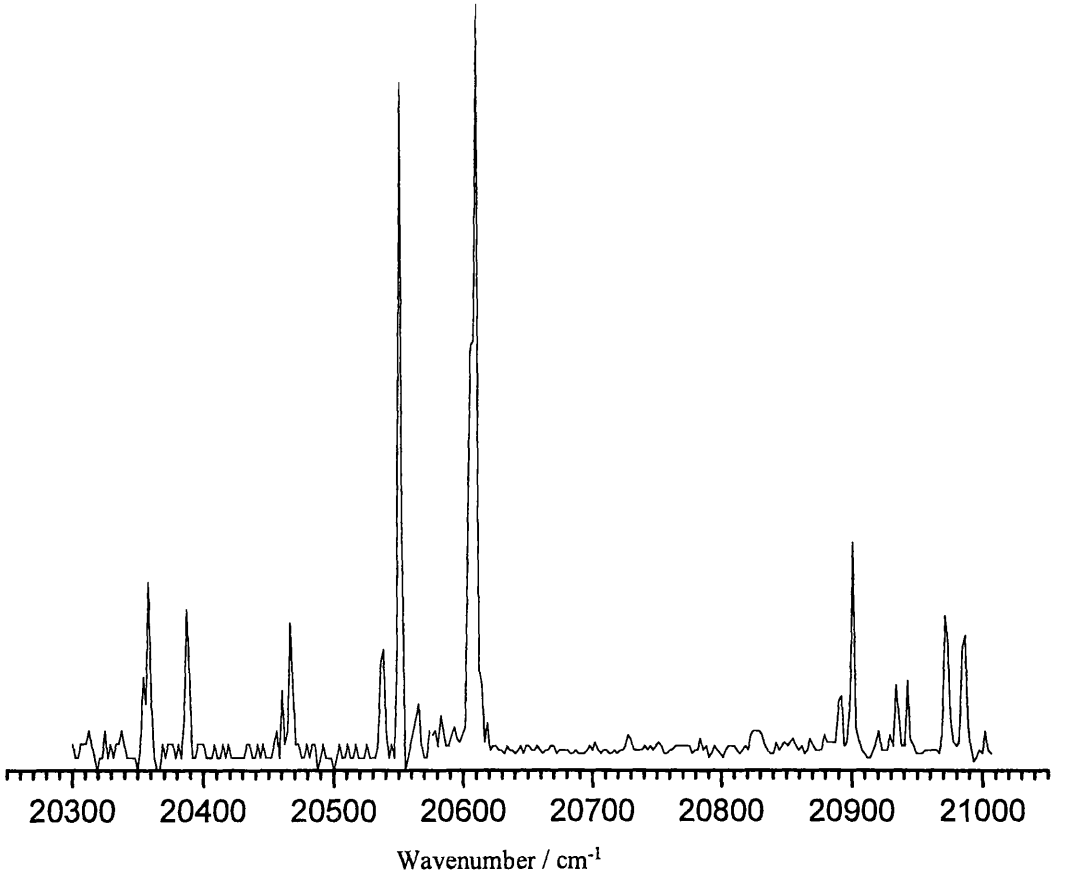

Figure 3.1. Laser excitation spectrum of jet-cooled BaOH from 20300-21000 cm^{-1}. This is a composite of two separate scans recorded with the same laser dye; no correction has been made for variation in dye laser pulse energy as a function of wavelength.

Table 3.2 and Figure 3.9 at the end of the results section provide a detailed summary of band positions and the assignments discussed in the following sections.

3.3.1 Electronic origin

The two strongest bands in the laser excitation spectrum are those centred at 20550 and 20608 cm^{-1}. Repeated scans have shown that these bands have similar intensities. One possible assignment is therefore that they form a spin-orbit doublet, and that the transition responsible is from the $\tilde{X}^2\Sigma^+$ state of BaOH to a $^2\Pi$ excited electronic state. To test this proposition both dispersed fluorescence and rotationally resolved studies were carried out.

The dispersed fluorescence spectrum obtained by laser exciting the 20550 cm^{-1} transition is shown in Figure 3.2. The vibrational frequencies of both the Ba-O-H bending ($2\nu_2$ = 661.1 cm^{-1}) and Ba-O stretching (ν_3 = 492.4 cm^{-1}) modes in the ground electronic state are well known from previous work by Kinsey-Nielson and co-workers.[4] It is therefore a simple matter to assign the short vibrational progression observed, and one finds that even quantum number excitation of the bending mode is responsible. The Ba-O-H bending mode is a non-totally symmetric vibrational mode and therefore single quantum excitation of this mode is forbidden in the Frank-Condon limit.

A higher resolution scan of the first member of the bending progression reveals two peaks separated by approximately 30 cm^{-1}. These can be attributed to the two vibrational angular momentum states $l_2'' = 0$ and $l_2'' = 2$, arising from $v_2'' = 2$. l_2 is the vibrational angular momentum quantum number of the bending vibration. These two states have Σ and Δ symmetries, as shown in Figure 3.3, and both are optically accessible from a $^2\Pi$ excited electronic state. The two vibrational angular

momentum states have different energies by virtue of the $g_{22}l^2$ term appearing in the vibrational term value (with respect to the zero point level)

$$G_0(0,v_2,0) = \omega_2 v_2 + x_{22}v_2^2 + g_{22}l_2^2 \qquad (3.1)$$

where ω_2 and x_{22} are respectively the harmonic frequency and diagonal anharmonicity constants for the bending mode.[8] It has been shown previously that g_{22} in the ground electronic state of BaOH is *ca.* 8 cm^{-1}.[7] The magnitude of the $g_{22}l^2$ splitting in dispersed fluorescence spectra proved to be an important aid in assigning vibrational quantum numbers for several transitions and will be encountered again later.

The dispersed fluorescence spectrum obtained by laser exciting at 20608 cm^{-1} is virtually the same as that shown in Figure 3.2. This is consistent with this band being the spin-orbit partner of the 20550 cm^{-1} band. The lack of extensive vibrational structure, coupled with the absence of any bands to the blue of the laser wavelength (not shown in Figure 3.2), suggests that these bands might form the origin (0_0^0) of a $^2\Pi - \widetilde{X}\,^2\Sigma^+$ electronic system.

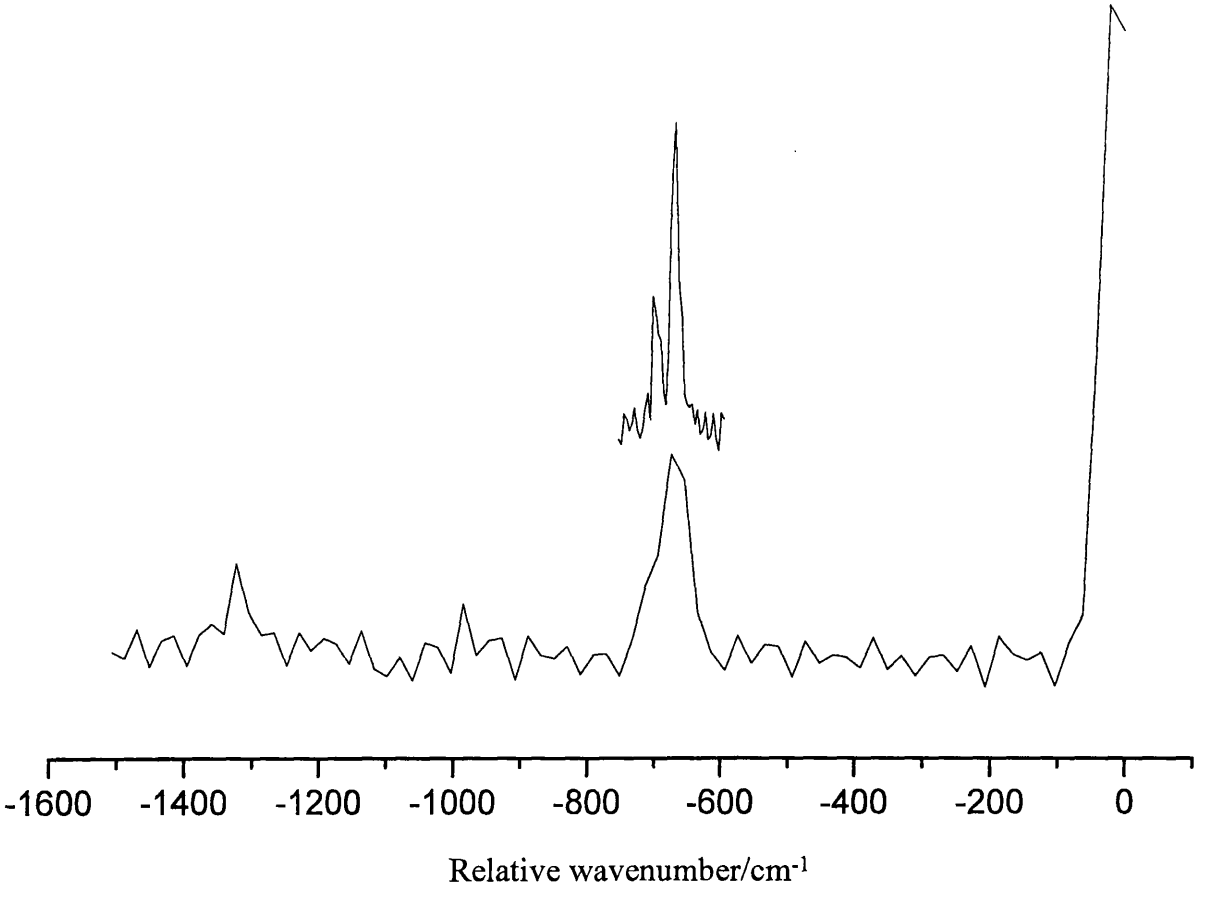

Figure 3.2. Dispersed fluorescence spectrum of BaOH obtained by fixing the dye laser at 20552 cm^{-1}. Above the survey scan is a portion of the spectrum with higher resolution and more laser shots.

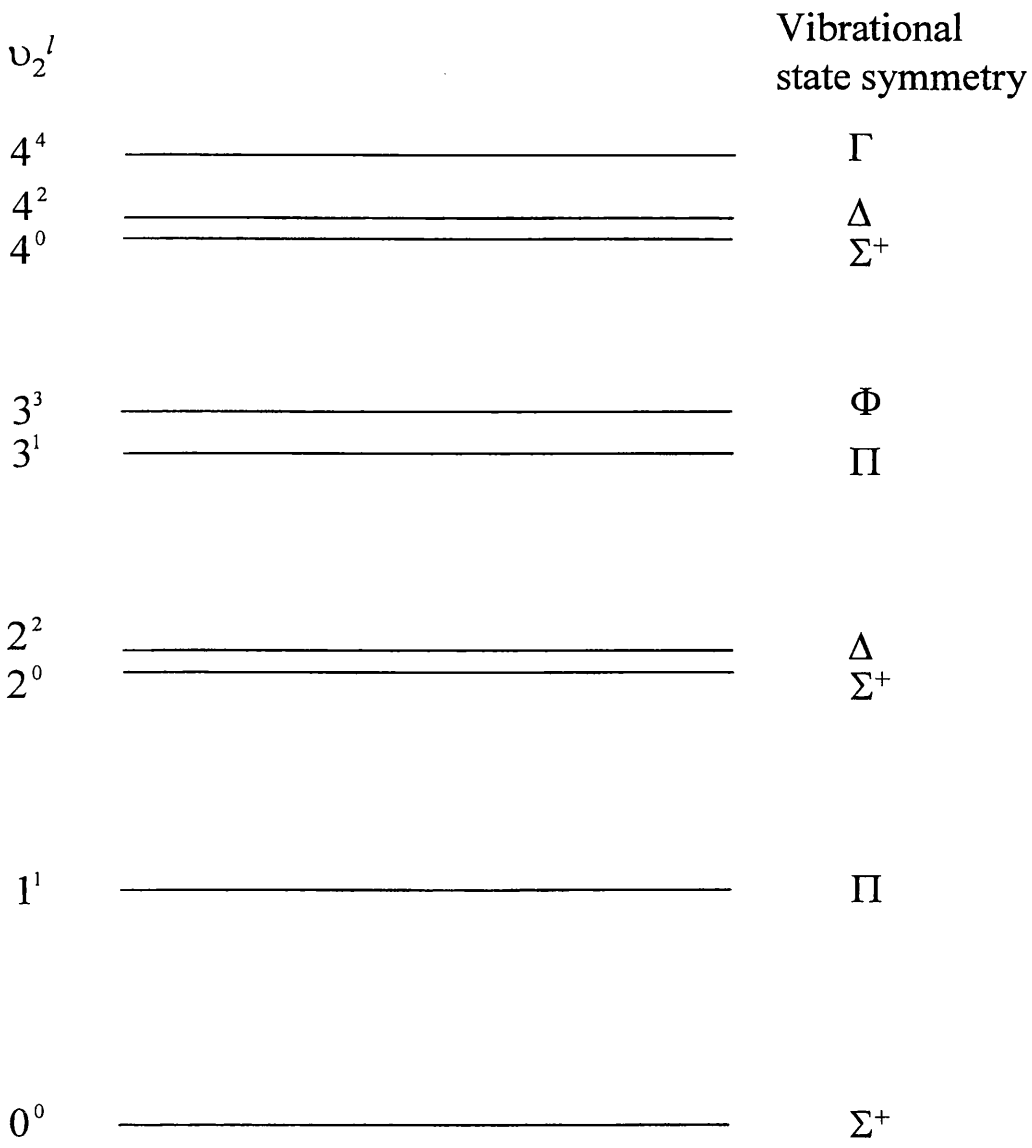

Figure 3.3. Illustration of the bending vibrational manifold in the ground electronic state of BaOH. The splitting of excited levels caused by different vibrational angular momenta is clearly shown, as are the resulting vibrational state symmetries.

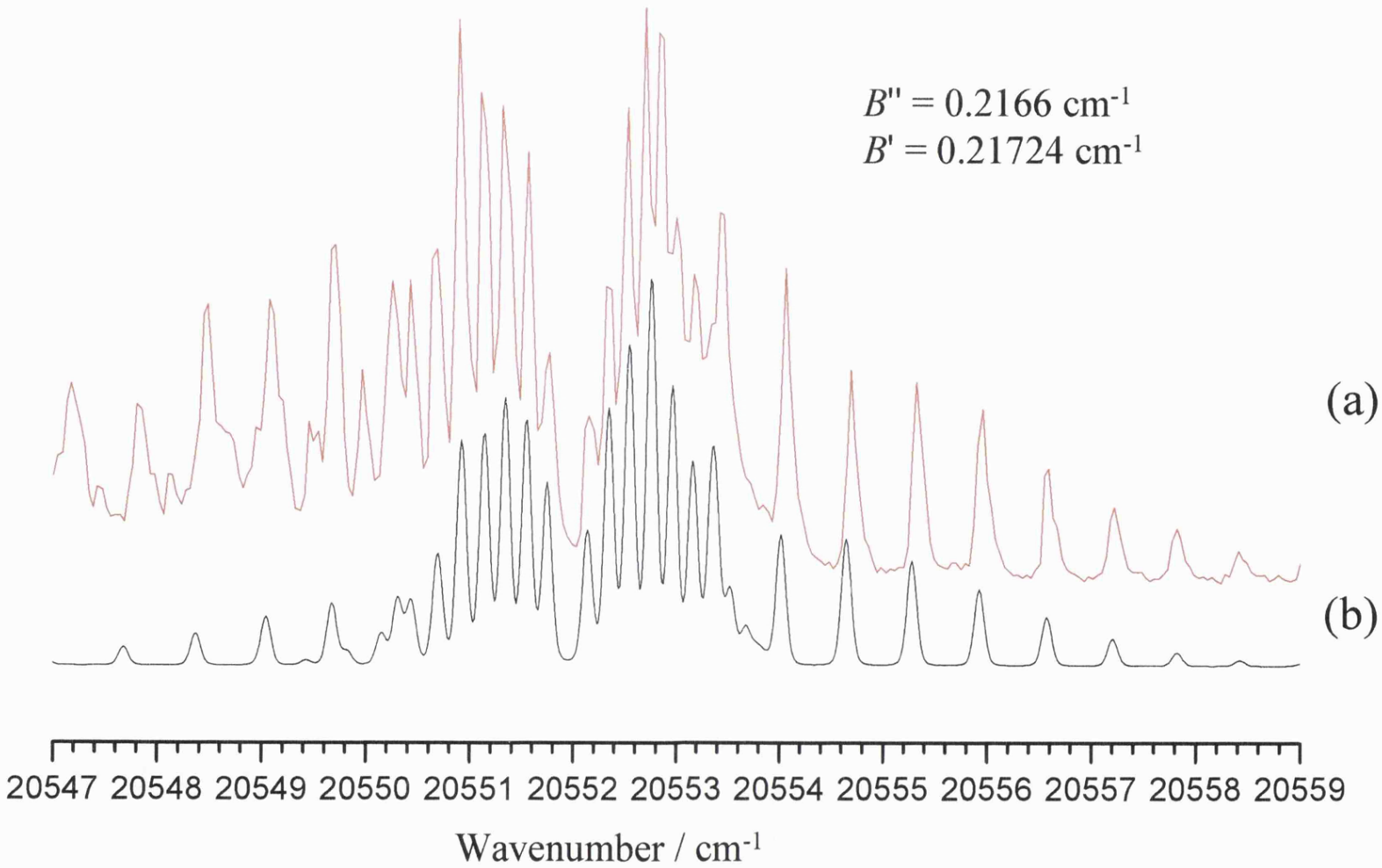

Figure 3.4 (a) Laser excitation spectrum of the 20550 cm^{-1} band. (b) Simulation assuming a $^2\Pi_{1/2}$-$^2\Sigma^+$ transition and B'' = 0.2166 cm^{-1}, B' = 0.21724 cm^{-1}. A temperature of 8 K was assumed in the simulation.

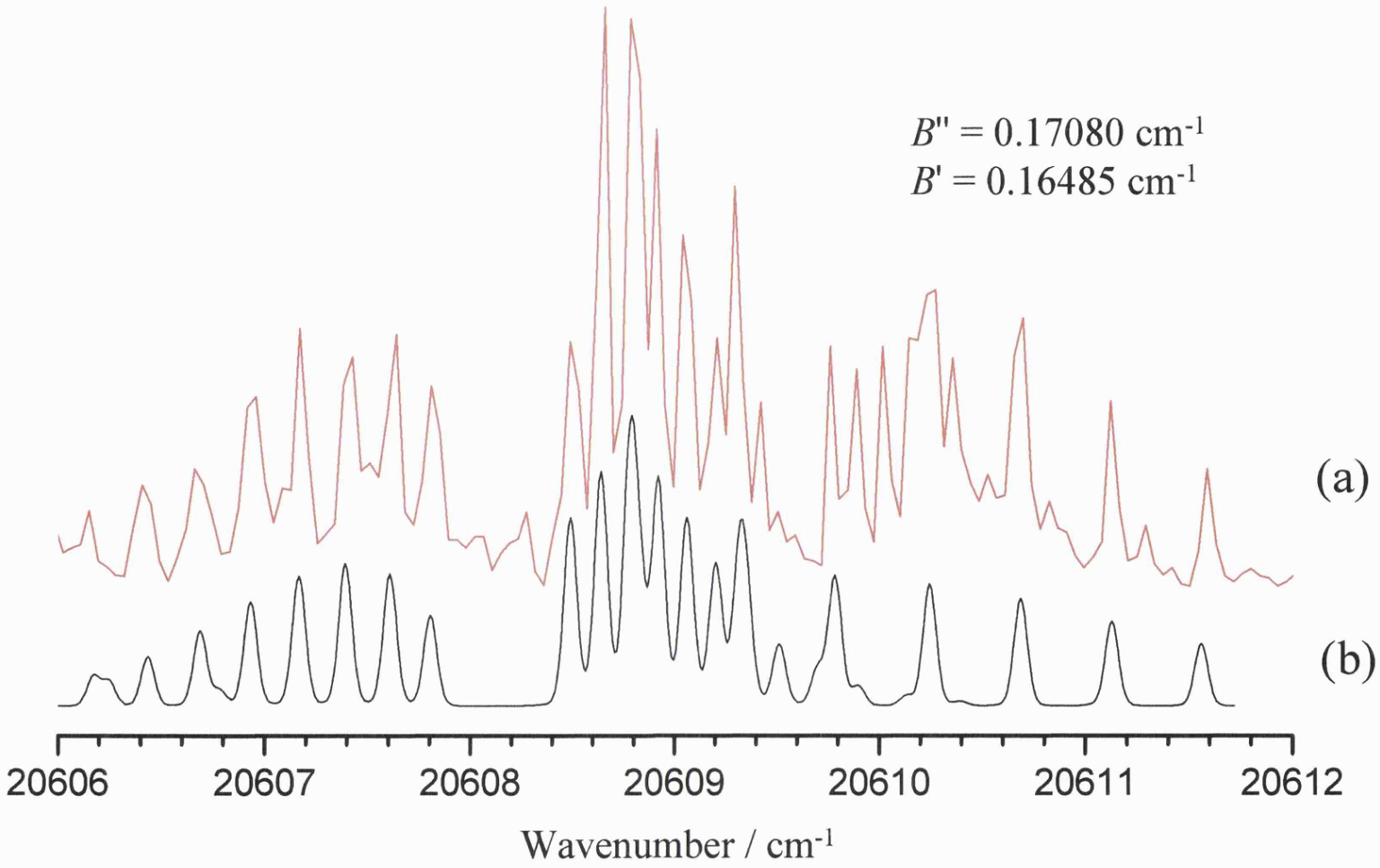

Figure 3.5. (a) Laser excitation spectrum of the 20608 cm^{-1} band. (b) Simulation assuming a $^2\Pi_{3/2}$-$^2\Sigma^+$ transition and B'' = 0.17080 cm^{-1}, B' = 0.16485. A temperature of 8 K was assumed.

To obtain further information, rotationally-resolved excitation spectra were recorded (see Figures 3.4 and 3.5). For a $\widetilde{C}^2\Pi$-$\widetilde{X}^2\Sigma^+$ transition, each spin-orbit component will consist of six rotational branches. However, only four branches were observed in this work because the spin-rotation splitting in the ground electronic state is too small for its effects to be resolved. Moving from low to high wavenumber, the four resolved branches give separations of approximately $3B$, B, B, and $3B$, respectively, between adjacent members where B is the rotational constant. The 20550 and 20608 cm^{-1} bands both show exactly this type of structure.

In the earlier study by Pooley *et al.*[7] the resolution was sufficient to partly resolve the outer ($3B$) branches, but not the inner (B) branches. In the present work, carried out with a dye laser of narrower linewidth, the B structure is almost fully resolved. This makes it possible to measure the zero gap and therefore establish Ω', the quantum number for the projection of total electronic angular momentum onto the internuclear axis in the excited state. We find that $\Omega' = 1/2$ for the 20550 cm^{-1} band. It is more difficult to measure the zero gap for the 20608 cm^{-1} band, despite recording several different spectra. The spectrum appears to show an anomalous peak within the zero gap, which may or may not be due to BaOH. Measurement of the two possible zero gap spacings yields $4.0\,\overline{B}$ or $2.8\,\overline{B}$, where $\overline{B} = (B'+B'')/2$. It therefore seems likely that $\Omega' = 3/2$ and not 1/2. This is consistent with the assignment of the 20550 and 20608 cm^{-1} bands as spin-orbit partners, and if correct they constitute a *regular* spin-orbit doublet, as expected for a $^2\Pi$ state of BaOH in which a single electron resides in the outermost π orbital. Notice that this assignment reveals an error in the previous work on BaOH.[7] In the absence of full rotational resolution, Pooley *et al.* tentatively assigned the 20550 cm^{-1} band to a $\widetilde{C}^2\Pi_{3/2}$-$\widetilde{X}^2\Sigma^+$ transition, with the other spin-orbit partner assumed to be at much lower wavenumber (20270

cm^{-1}). The spectrum in Figure 3.4 clearly shows the earlier assignment to be incorrect.

We have attempted to extract spectroscopic constants from the rotationally resolved bands in Figures 3.4 and 3.5. Least squares fits were carried out using the program PGopher.[9] Unfortunately, it proved impossible to obtain satisfactory fits by using the same rotational constants for the two bands. In fact, as will be seen shortly, dramatically different constants were required in the two cases. For the 20550 cm^{-1} band, a good fit could be obtained by fixing the ground state constants (B'' and γ'') to values previously determined by Kinsey-Nielson and co-workers,[4] which were confirmed in a later millimetre wave study.[10] The rotational constants obtained from the fit are summarised on the spectrum. The rotational constant in the $^2\Pi_{1/2}$ excited state is virtually unchanged from that in the ground electronic state. This finding, which suggests that the Ba-O bond length is unaltered by the electronic transition, is consistent with the absence of observable structure in the Ba-O stretching mode in the dispersed fluorescence spectrum.

The rotational structure for the $\widetilde{C}\,^2\Pi_{3/2}$-$\widetilde{X}\,^2\Sigma^+$ band at 20608 cm^{-1} is more puzzling. Despite repeated efforts, we have not been able to obtain an acceptable fit by fixing the ground state rotational constants at their known values. The simulation in Figure 3.5 looks quite reasonable, but was obtained with a physically unreasonable set of constants, notably B'' = 0.17080(38) and B' = 0.16485(43) cm^{-1}. Introduction of lambda doubling parameters and centrifugal distortion constants did not significantly improve the fit. We have not been able to obtain a satisfactory explanation for this finding. However, it does throw serious doubt on the assignment of this band to the spin-orbit partner of the 20550 cm^{-1} band.

3.3.2 Cluster of bands in 20900-21000 cm^{-1} region

Four bands attributable to BaOH were observed in this region. The relative intensities suggest two closely spaced pairs, 20931/20940 and 20971/20986 cm^{-1}. This division into pairs is somewhat arbitrary and is only supported by dispersed fluorescence spectra for the 20971/20986 cm^{-1} pair. Despite repeated attempts, a satisfactory DF spectrum could not be obtained for the 20931 cm^{-1} band because of insufficient intensity. The DF spectrum of the 20940 cm^{-1} band is dominated by a progression in even quanta of the bending mode, with both $-2v_2''$ and $-4v_2''$ bands having substantial intensities. This indicates that the corresponding excitation transition involves $\Delta v_2'' \neq 0$. In addition, the $-2v_2''$ band is resolved into two components separated by approximately 86 ± 10 cm^{-1}. Within experimental error, this is the $g_{22}l^2$ splitting expected between l = 4 (Γ) and l = 2 (Δ) vibrational levels in the ground electronic state. Since even l values only arise for even v_2, this proves that v_2'' is even in both the upper and lower states of the excitation transition, since $\Delta v_2''$ = even transitions dominate. Furthermore, the upper state must have $^2\Phi$ vibronic symmetry in order for allowed transitions to occur to $^2\Gamma$ and $^2\Delta$ levels in the ground electronic state. The most likely assignment is a transition from $v_2'' = 2$, although $v_2'' = 4$ cannot be ruled out at this stage. In other words, the transition must be a hot band.

To obtain further information, rotationally resolved spectra were recorded. The spectrum for the 20940 cm^{-1} band is very similar to that shown in Figure 3.6 for the 20936 cm^{-1} band. The structure is markedly different from that seen in Figures 3.4 and 3.5, showing a far larger zero gap between the +B and -B branches. The

magnitude of the zero gap is consistent with a transition to an $\Omega' = 5/2$ state. A state of Δ vibrational symmetry is formed by $v_2'' = 2$, so the rotational structure supports the earlier DF evidence pointing towards a $^2\Delta$ lower state and a $^2\Phi$ excited state.

The rotational structure of the 20931 cm^{-1} band indicates that the upper state in this case also has $\Omega' = 5/2$. Without a DF spectrum it is not possible to firmly assign the vibrational levels involved. If this band is assumed to be part of the same electronic system as the 20550/20608 'origin' transitions, then sequence transitions, such as 2_1^1 or 2_2^2, can be disregarded, since these should be quite close to the 0_0^0 transitions. However the band clearly originates from a vibrationally excited lower state since the lower state symmetry is not Σ. One possible assignment is to a $^2\Delta_{5/2} - \widetilde{X}\,^2\Sigma(^2\Pi)\,2_1^3$ transition, although an alternative assignment to $^2\Phi_{5/2} - \widetilde{X}\,^2\Sigma(^2\Delta)2_2^4$ must also be considered. The notation $\widetilde{X}\,^2\Sigma(^2\Pi)$ indicates that the ground electronic state has $^2\Sigma$ symmetry, but the ground vibronic state has $^2\Pi$ symmetry. This notation will be used throughout the remainder of this chapter to distinguish the ground vibronic symmetry from the ground state electronic symmetry.

In a least squares fit of the 20931 cm^{-1} spectrum, both B' and B'' were floated, since the transition no longer takes place from the ground vibrational state. The rotational constants obtained were $B'' = 0.20562(46)$ cm^{-1} and $B' = 0.20614(48)$ cm^{-1}. Rotational constants have been determined for several vibrational levels of BaOH in its ground electronic state by Ziurys and co-workers using millimetre wave spectroscopy.[11] For the (010) level they found B'' to be 0.21633 cm^{-1}, somewhat smaller than the value for the zero point level (0.21661 cm^{-1}). The rotational constants obtained from the least squares fit in the present work are of insufficient precision to be able to use the Ziurys data as an aid in assigning v_2''.

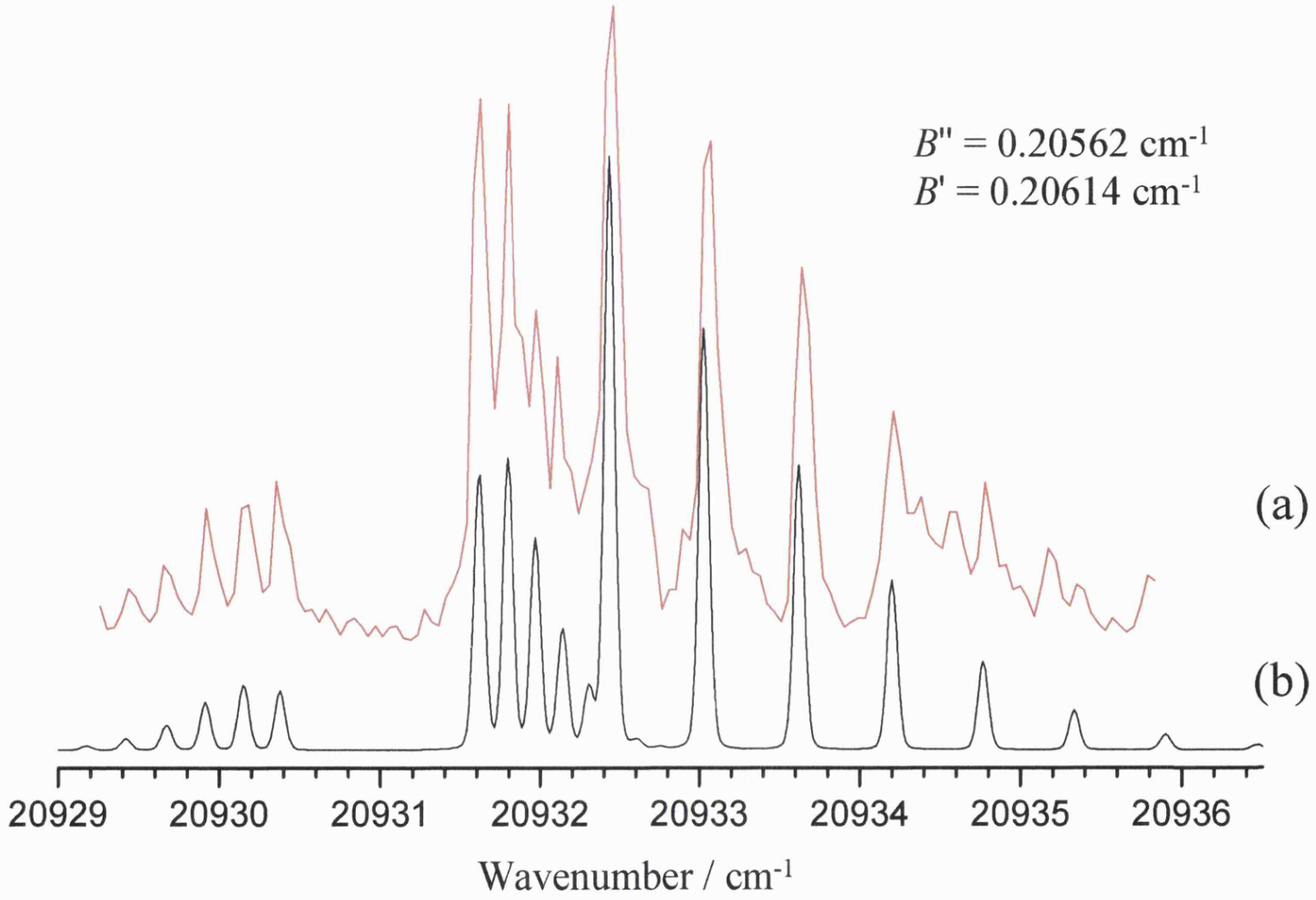

Figure 3.6. (a) Rotationally-resolved laser excitation spectrum of the 20931 cm^{-1} band. (b) Simulation assuming a $^2\Delta_{5/2}$-$^2\Pi$(b) transition and B'' = 0.20562 cm^{-1}, B' = 0.20614 cm^{-1}. A temperature of 8 K was assumed in the simulation.

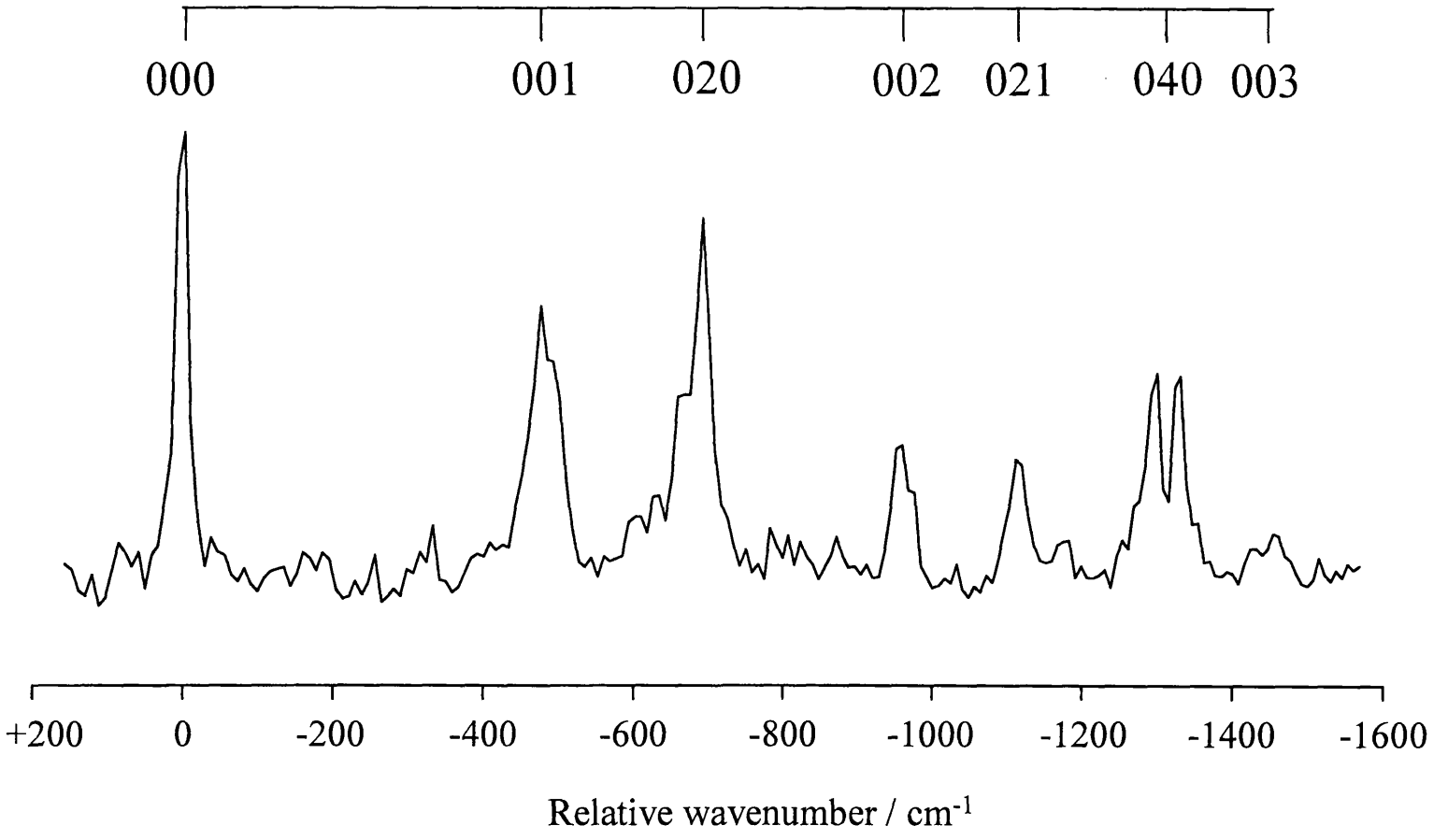

Figure 3.7. Dispersed fluorescence spectrum of BaOH obtained by fixing the dye laser at 20971 cm^{-1}. The quantum numbers v_1, v_2 and v_3 referred to in the labels (v_1 v_2 v_3) are for the O-H stretching, Ba-O-H bending, and Ba-O stretching modes, respectively, in the ground electronic state.

Turning now to the 20971 and 20986 cm^{-1} bands, the dispersed fluorescence spectra obtained by exciting these two transitions were very similar. In both cases $\Delta v_2'' = +2$ and $\Delta v_2'' = +4$ bands were prominent, just as for the lower energy (20940 cm^{-1}) band described above. However, an important difference was the observation of substantial activity in the Ba-O stretch, as can be seen in Figure 3.7. This contrasts with dispersed fluorescence spectra from other bands, where only weak $-\nu_3$ bands have been seen. The vibrational structure suggests that the pump transition combines 2_0^2 and 3_0^1 character. However it is not believed that this is a $2_0^2 3_0^1$ combination transition because this would be expected to occur in a totally different position in the overall electronic band system. Instead it is likely that the upper state is one component of the Fermi resonance doublet formed by anharmonic coupling of the (020) and (001) vibrational levels. The activity in ν_3 would then be obtained by intensity 'stealing' from the much stronger $\Delta\nu_2 = 2$ transition.

The rotationally resolved excitation spectra of the 20971 and 20986 cm^{-1} bands, shown in Figures 3.8 and 3.9, reveal that these bands are due to $^2\Pi_{1/2} - \tilde{X}^2\Sigma^+$ and $^2\Pi_{3/2} - \tilde{X}^2\Sigma^+$ vibronic transitions, respectively. Clearly the proximity of these bands is inconsistent with the tentative spin-orbit splitting (56 cm^{-1}) reported earlier for the 0_0^0 transition. However, excitation of the bending mode in the $^2\Pi$ excited electronic state introduces Renner-Teller coupling, which complicates the vibronic energy level structure. An illustration of the effect on vibronic levels in the v_2' manifold is shown in Figure 3.10. For $v_2' = 2$ there are four resulting $^2\Pi$ vibronic states, which divide into a lower and upper $^2\Pi_{1/2}/^2\Pi_{3/2}$ pair which, following the notation introduced by Hougen,[12] are distinguished by attaching the additional labels

μ and κ. One doublet has the regular ordering (μ) of spin-orbit sub-states, the other is inverted (κ). The regular ordering observed in the spectrum, the $^2\Pi_{1/2}$ state lying beneath $^2\Pi_{3/2}$, is consistent with an assignment to the $\mu^2\Pi$ pair. The separation of these two states is expected to be quite small, and we therefore tentatively assign the 20971 and 20985 cm^{-1} bands to $\mu^2\Pi_{1/2}/^2\Pi_{3/2}$-$\tilde{X}^2\Sigma^+$ vibronic transitions of mixed $2_0^2/3_0^1$ character.

Interestingly, the $^2\Pi_{3/2}-\tilde{X}^2\Sigma^+$ transition at 20986 cm^{-1} shows similar behaviour to the $^2\Pi_{3/2}-\tilde{X}^2\Sigma^+$ transition nominally associated with the electronic origin (20608 cm^{-1}), namely anomalously low rotational constants are required to obtain a satisfactory simulation of the rotational structure. This may indicate that a strong perturbation acting on $^2\Pi_{3/2}$ states in this region is in operation.

3.3.3 20276/20356 cm^{-1} bands

Of the next pair of bands to be considered, those at 20276 and 20356 cm^{-1}, only the latter is included in the survey scan in Figure 3.1. These two bands were originally assigned to origin transitions to two different $^2\Pi_{1/2}$ excited states by Pooley *et al.*[7] It is clear from the excitation spectra that the 20276 cm^{-1} band has a zero gap of approximately $2\overline{B}$ and the 20356 cm^{-1} band, Figure 3.11, has a larger zero gap of approximately $4\overline{B}$. It would therefore initially appear as though these two bands form a spin-orbit doublet. However, there are a number of features in the DF spectra that cast some doubt on this.

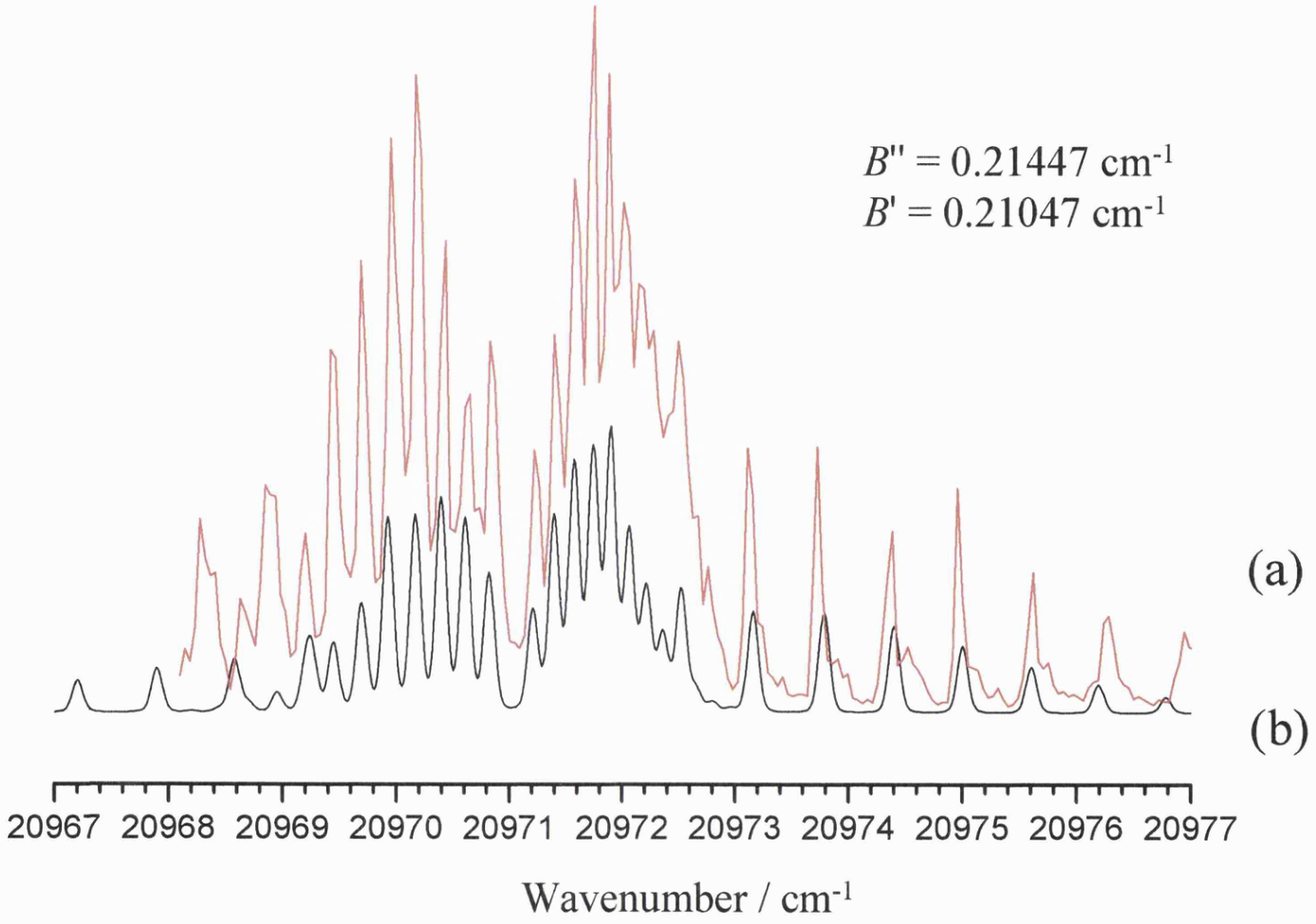

Figure 3.8. (a) Laser excitation spectrum of the 20971 cm^{-1} band of BaOH. (b) Simulation assuming a $^2\Pi_{1/2}$-$^2\Sigma^+$ transition and B'' = 0.21447 cm^{-1} and B' = 0.21047 cm^{-1}. A temperature of 8 K was assumed in the simulation.

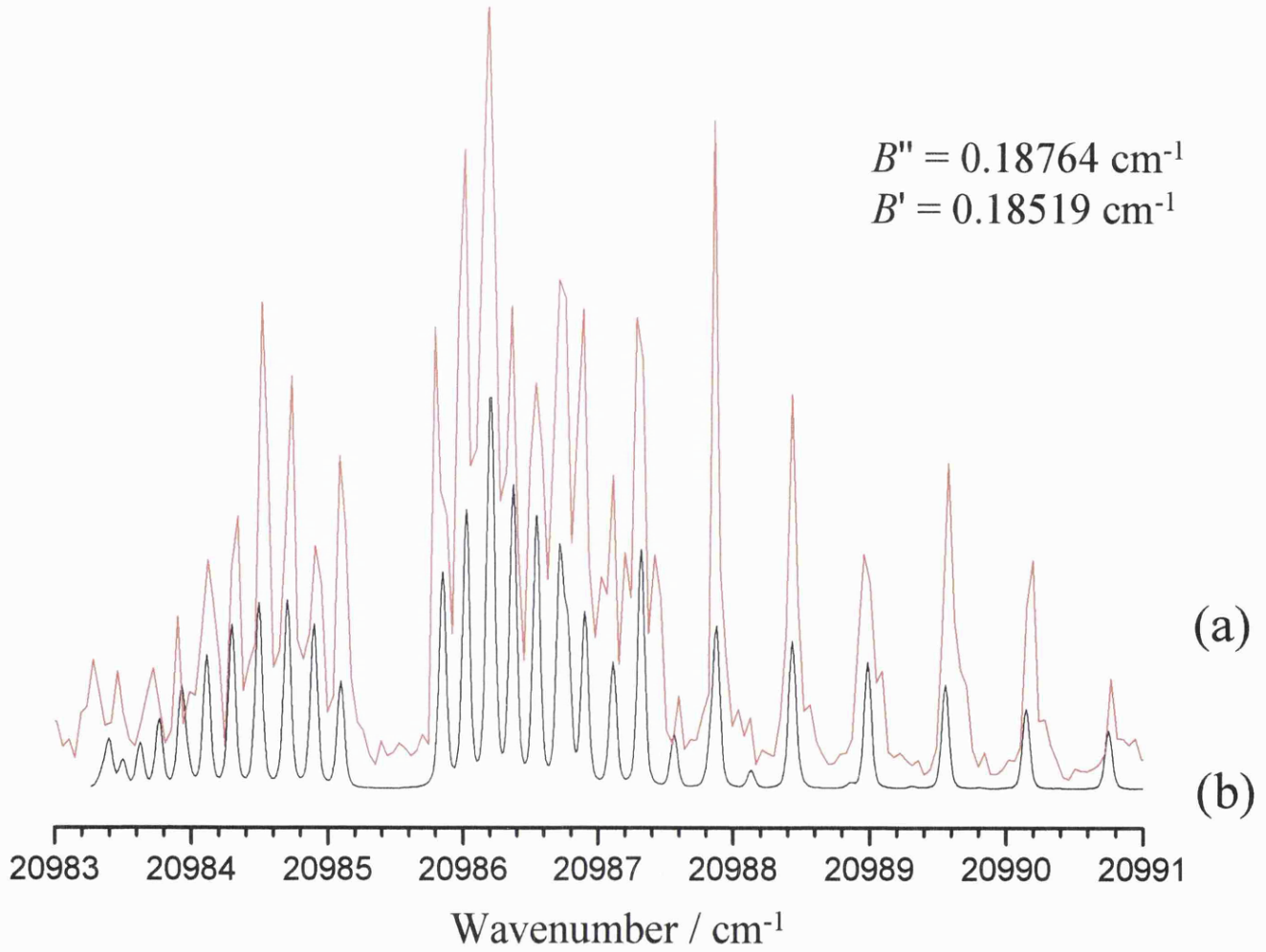

Figure 3.9. (a) Laser excitation spectrum of the 20986 cm^{-1} band of BaOH. (b) Simulation assuming a $^2\Pi_{3/2}$-$^2\Sigma^+$ transition B'' = 0.18764 cm^{-1} and B' = 0.18519 cm^{-1}. A temperature of 8 K was assumed in the simulation.

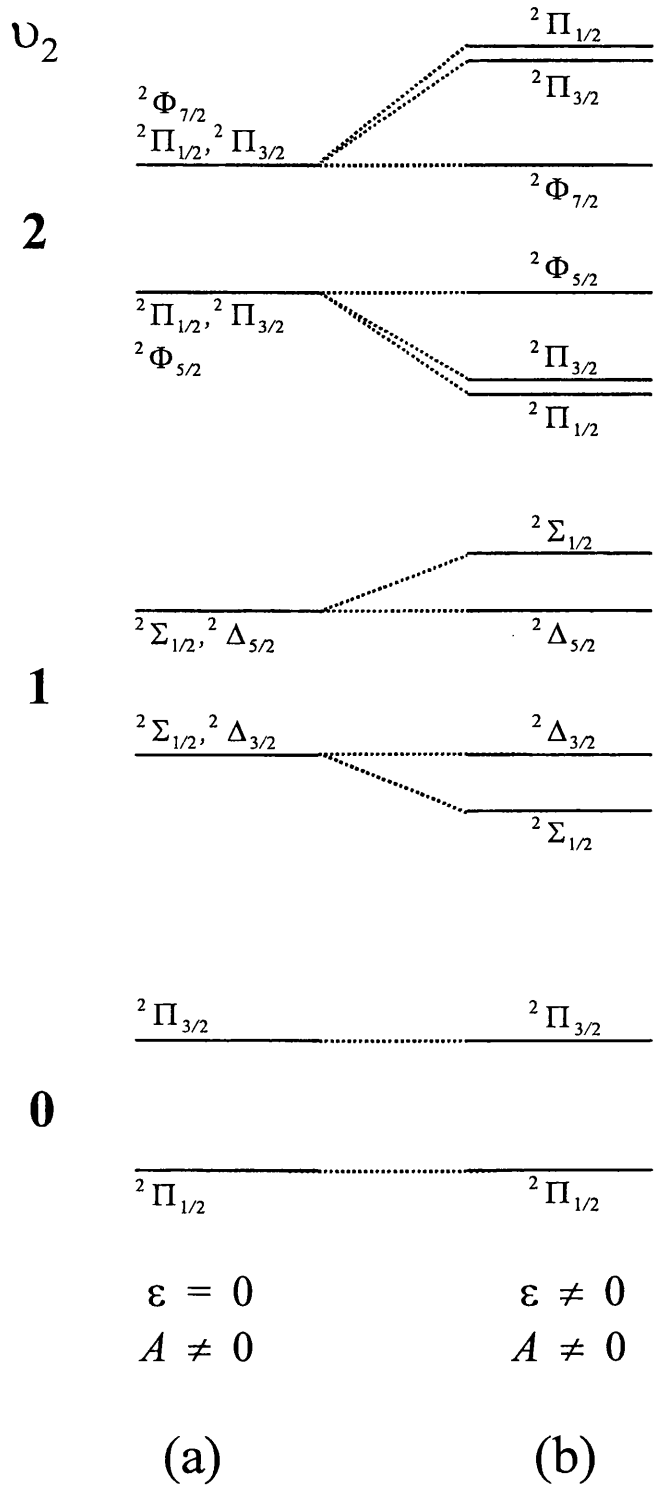

Figure 3.10. Illustration of the pattern of vibronic energy levels in the ν_2' manifold of a $^2\Pi$ electronic state with spin-orbit coupling constant A for (a) no Renner-Teller effect ($\varepsilon = 0$) and (b) with Renner Teller effect.

The DF spectra for both bands show the characteristic progression in Δv_2" = even. Excitation of the 20356 cm^{-1} transition shows a progression containing two members, $\Delta v_2'' = -2$ and $\Delta v_2'' = -4$, and as seen for the 'origin' transitions at 20550 and 20608 cm^{-1} the first member shows a splitting due to vibrational angular momentum of ~30 cm^{-1}. Additionally, no emission is observed to the blue of the pump position. given the substantial progression in v_2" to the red of the pump position, emission to the blue of the pump position would be expected if the 20356 cm^{-1} band was due to a hot band transition. The observed spectra suggest that this band is most likely to be a $^2\Pi_{3/2} - \widetilde{X}^2\Sigma^+ 0_0^0$ transition. The DF spectrum of the 20276 cm^{-1} band does not show the second member of the progression in v_2", nor does it show any splitting to due vibrational anharmonicity. There is however a relatively strong single member of a progression in v_3", the Ba-O stretch. The observation of activity in the stretch indicates that this may be a combination band. However if this were the case the position of the band in the overall spectrum would be expected to be shifted considerably. A more suitable alternative, is that intensity stealing similar to that proposed earlier for the 20971 and 20986 cm^{-1} bands accounts for the v_3" character. The absence of observed emission to the blue of the pump position in DF suggests that this band is an origin band, however the v_3" character and lack of vibrational harmonic splitting in Δv_2" contradict this. Therefore this band is tentatively assigned to an origin $^2\Pi_{1/2} - \widetilde{X}^2\Sigma^+ 0_0^0$ band at present because it is not possible with the present information to identify the vibronic levels involved that account for the observation of the stretch in DF. An alternative assignment is discussed later in section 3.4.

A satisfactory simulation of the rotational structure is only available for the 20356 cm^{-1} band and this adds more confusion to the assignment. A good fit could only be achieved if the ground state rotational constants are varied considerably from those determined by Kinsey-Nielson.[4] However, the simulation does suggest very similar rotational constants for the ground and excited states, B'' = 0.2407 and B' = 0.2419 cm^{-1}.

If these bands are a spin-orbit pair it is clear that one band is perturbed quite considerably compared to the other. Once again this could be an example of Ω' = 3/2 state being perturbed. If these bands are also 'origin' transitions, as the DF spectra indicate (if the activity in v_3 is ignored), then there must be two excited $^2\Pi$ states present in close proximity in BaOH, in agreement with the tentative conclusion made previously be Pooley, Beardah and Ellis.[7] However, information on the orbital characteristics of these states, which might indicate why two $^2\Pi$ states should be in such close proximity, is not forthcoming from the present analysis.

3.3.4 20467/20533 cm^{-1} bands

The next pair of bands meriting detailed discussion appear at 20467 and 20533 cm^{-1}. The DF spectra from both bands are very similar. Both show structure in v_2'', consisting of one member at $\Delta v_2''$ = -2. No emission is detected to higher energy than the pump position. The single observed peak (aside from emission at the excitation wavelength) is sharp and there is no evidence of a splitting due to vibrational angular momentum.

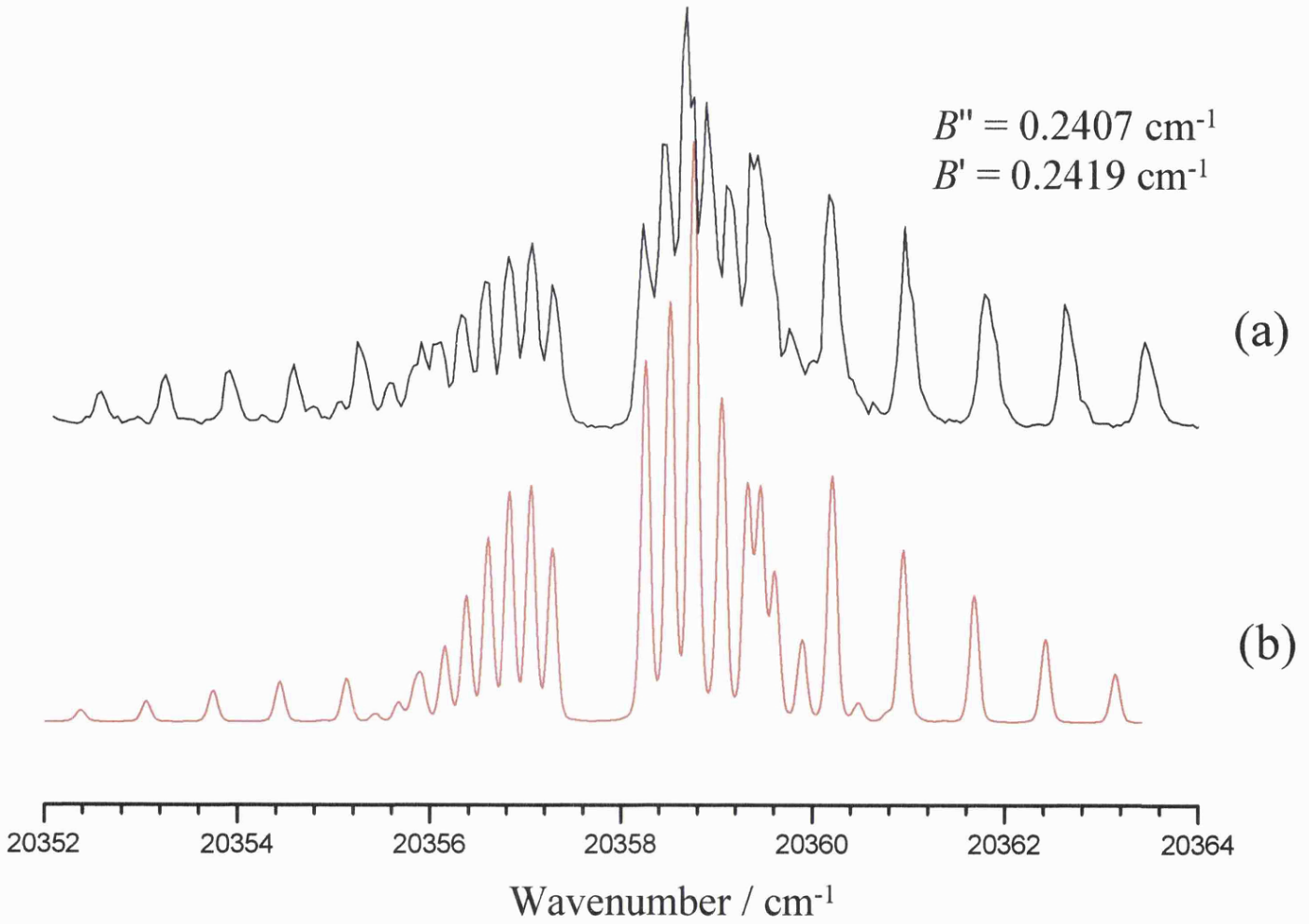

Figure 3.11. (a) Laser excitation spectrum of the 20356 cm^{-1} band of BaOH. (b) Simulation assuming a $^2\Pi_{3/2}$-$^2\Sigma^+$ transition and B'' = 0.2407 and B' = 0.2419. A temperature of 8 K was assumed in the simulation.

Both excitation bands are quite weak and this detracts from the quality of the rotationally resolved excitation spectra. The 20533 cm^{-1} band has a large zero gap, approximately $6B$, and therefore signifies $\Omega' = 5/2$. The excitation spectrum for the 20467 cm^{-1} band is more confusing. B is easily deduced to be ~0.2 cm^{-1} from the $3B$ structure, the same as for the 20533 cm^{-1} band. However there appears to be a weak peak in the zero gap region that raises doubt as to whether the gap is $2B$ or $4B$, thus indicating either $\Omega' = 1/2$ or 3/2 state.

If the 20467 and 20533 cm^{-1} bands are spin-orbit partners then Ω' must equal 3/2 for the 20467 cm^{-1} band. Assuming this is the case, the vibronic transition must be $\Delta \leftarrow \Pi$. In the DF spectra, no peaks to the blue of the pump position were observed. If $v_2'' = 2$ or higher then peaks to the blue of the pump position in DF would be expected. Consequently, the DF spectra indicate that these bands are excited from $v_2'' = 0$ or 1 in the ground state. However the ground state vibronic symmetry is only correct for a $\Delta \leftarrow \Pi$ transition if v_2'' = odd, *i.e.* $v_2'' = 1$.

If the bands are connected with either of the two pairs of 'origin' transitions tentatively identified earlier then presumably $v_2' = 1$ in the upper vibronic state, indicating the 20467 and 20533 cm^{-1} bands to be due to ${}^2\Delta_{3/2} - \widetilde{X}\,{}^2\Sigma({}^2\Pi)\,2_1^1$ and ${}^2\Delta_{5/2} - \widetilde{X}\,{}^2\Sigma({}^2\Pi)\,2_1^1$ sequence transitions, respectively. However this would indicate quite a large change in the vibrational frequency from the ground to the excited state, whichever pair of 'origin' bands relate to these bands. It has already been established that $v_2' < v_2''$, therefore the only 'origin' bands that match this observation are the 20550/20608 pair. Therefore the 20467/20533 bands may be part of the same electronic band system.

3.3.5 20107 and 20179 cm^{-1} bands.

These two bands are reasonably intense and produce some very clear and simple excitation spectra. They fall outside the region of the survey scan shown in Figure 3.1. Despite repeated attempts a good quality, clear survey scan of the entire region proved difficult to acquire. Instead survey scans were done in sections; indeed Figure 3.1 is an amalgamation of two scans.

Both bands show well resolved $3B$ structure and the 20107 cm^{-1} band also shows partly resolved B structure (see Figure 3.12). The B structure of the 20179 cm^{-1} band is very limited on account of the large $6B$ zero gap, clearly indicating an $\Omega' = 5/2$ state. The zero gap of the 20107 band is also very easily determined to be $4B$, indicating an $\Omega' = 3/2$ state. In both bands the rotational constant is ~0.2 cm^{-1}, similar to several of the other bands already discussed.

The DF spectra of both bands are very revealing. As seen in many earlier spectra, a band, due to $\Delta v_2'' = -2$ is observed. However, in this band a vibrational angular momentum splitting of 67 ± 10 cm^{-1} was observed. Within experimental error, this is the separation expected between the Π (l=1) and Φ (l=3) levels in v_2'' = odd (≥3) states. However, there is also a very weak peak at roughly +480 cm^{-1} in the DF spectra for both bands, as well as a much stronger peak at -476 cm^{-1} seen when the 20107 cm^{-1} transition was pumped. This suggests that in the excitation transition $v_3'' = 1$.

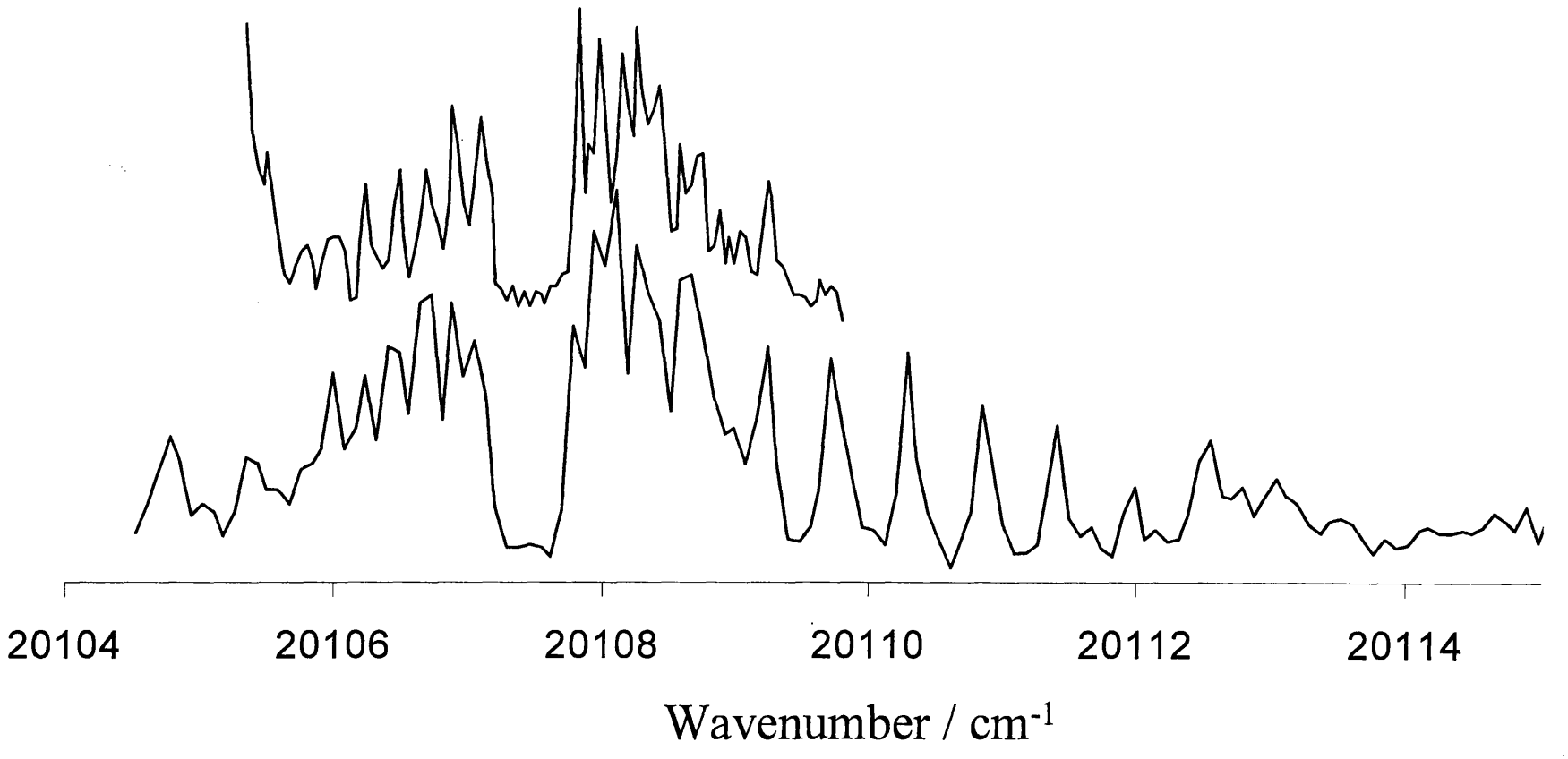

Figure 3.12. (a) Rotationally-resolved laser excitation spectrum of the 20107 cm^{-1} band of BaOH. The upper spectrum has been recorded with smaller step sizes than lower spectrum.

The position of these two bands within the overall electronic band system indicates that they might be either $2_3^1 3_1^1$ transitions associated with the 20550/20608 cm^{-1} origin, or $2_1^1 3_1^1$ sequence transitions associated with the 20276/20356 cm^{-1} origin. Therefore the most likely assignment for the 20107 and 20178 cm^{-1} bands is that they are $^2\Delta_{3/2}$ - $\tilde{X}\,^2\Sigma(^2\Pi)$ $2_x^1 3_1^1$ and $^2\Delta_{5/2}$ - $\tilde{X}\,^2\Sigma(^2\Pi)$ $2_x^1 3_1^1$ transitions, respectively, where x = 1 or 3.

3.3.6 19892 cm^{-1} band

The DF spectrum obtained by pumping the 19892 cm^{-1} transition shows structure only in v_2. A band is seen due to $\Delta v_2'' = 2$, but there is also a band to the blue of pump position, of roughly equal intensity, due to $\Delta v_2'' = -2$. This shows that the 19892 cm^{-1} transition is a hot band. The excitation spectrum shows a small but clear zero gap of $2B$, indicating $\Omega' = 1/2$. The rotational constant has been calculated to be approximately 0.2 cm^{-1} from the $3B$ structure. It would therefore appear probable that this band is due to a $^2\Pi_{1/2}$ - $\tilde{X}\,^2\Sigma^+$ 2_2^0 transition. The band at 19892 cm^{-1} is very likely to be associated with the same state as the 'origin' transitions at 20550/20608, because the 19892 cm^{-1} transition lies at the expected position for a 2_2^0 hot band relative to the 20550 0_0^0 band.

Despite extensive searching, the spin-orbit partner to the 19892 cm^{-1} band (correlating with the 20608 cm^{-1} band) could not be observed. This casts further doubt on the assignment of the 20608 cm^{-1} band as the spin-orbit partner to the 20550 cm^{-1} band.

3.3.7 19992 cm^{-1} band

This excitation band is very weak and this has prevented any DF spectra being recorded. However the excitation spectrum is revealing in that it shows the characteristic PQR branches of a $\Sigma \leftarrow \Pi$ transition (see Figure 3.13). The rotational constant estimated from the spectrum is ~0.2 cm^{-1}, consistent with most other bands already discussed. The location of the band indicates that it is probably a hot band with $\Delta v_2 = -2$ and, consequently, the most likely vibrational assignment is 2_3^1 because ground vibronic states of Π symmetry are only available for odd quanta of v_2". Excitation from $v_2" = 5$ or higher cannot be ruled out without DF spectra, although they are highly unlikely because of the temperature required for significant population of such levels. Consequently, the most likely assignment for this band is a $^2\Sigma - \widetilde{X}^2\Sigma(^2\Pi)\,2_3^1$ transition. The $v_2' = 1$ level, when split by spin-orbit interaction and the Renner-Teller effect, yields two Σ vibronic states, one above (denoted κ) and one below (denoted μ) the $^2\Delta$ pair also arising from $v_2' = 1$. Without associating the 19992 cm^{-1} band with a particular spin-orbit pair of Δ states, it is not possible to assign a μ or κ label.

3.3.8 20387 cm^{-1} band

This band is similar to the 19992 cm^{-1} band discussed above, *i.e.* corresponds to a $^2\Sigma \leftarrow ^2\Pi$ transition. However a simulation indicates a rotational constant in the excited state of 0.1724(17) cm^{-1}, and a much smaller $B"$ than might be expected, namely 0.1803(14) cm^{-1}.

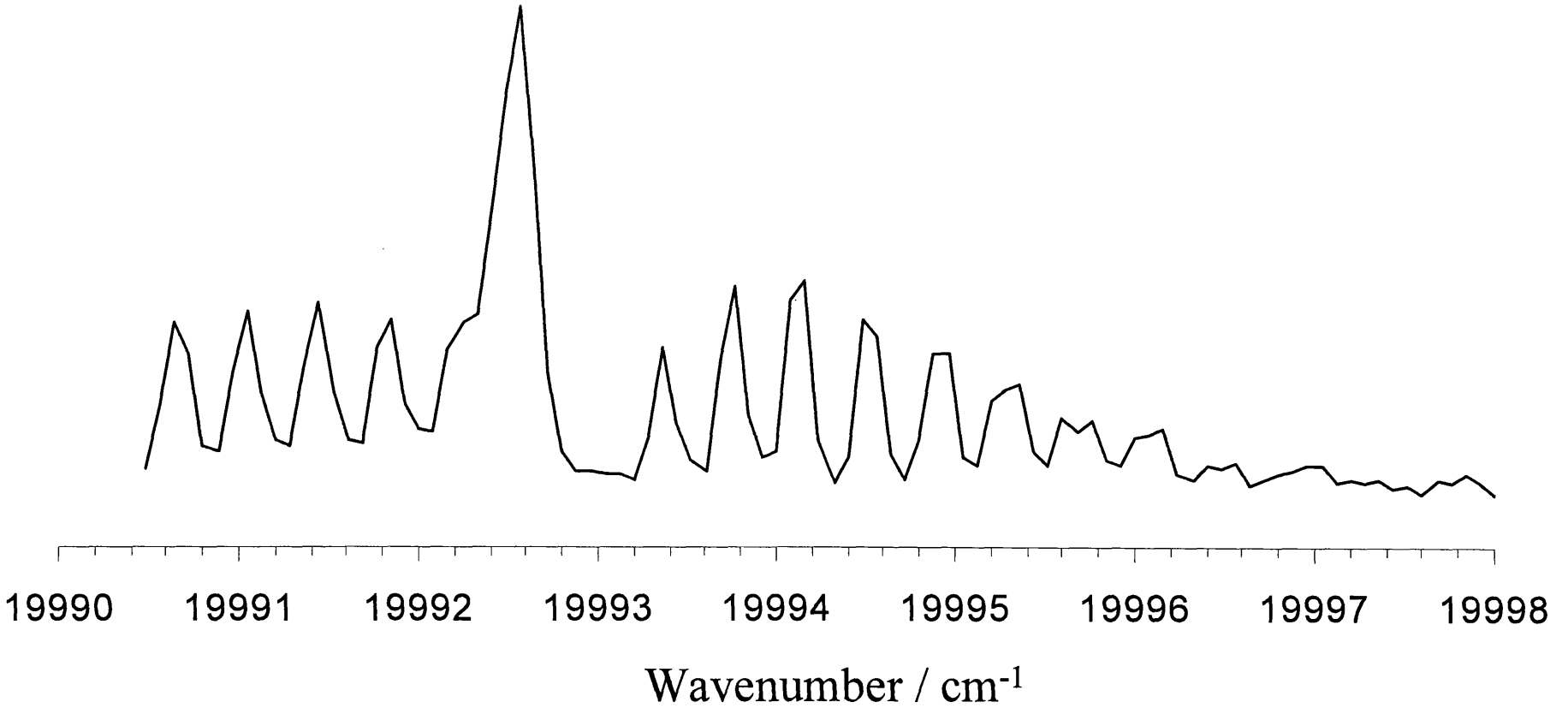

Figure 3.13. (a) Rotationally-resolved laser excitation spectrum of the 19992 cm^{-1} band of BaOH.

A DF spectrum has been recorded with a rather poor signal/noise ratio but which clearly shows peaks at -493 and -640 cm^{-1} from the pump position. corresponding to $\Delta v_3'' = 1$ and $\Delta v_2'' = 2$, respectively. The $\Delta v_2'' = 2$ peak is sharp and does not show any indication of splitting due to vibrational angular momentum. The presence of a $\Delta v_3 = 1$ transition with significant intensity indicates that the 19992 cm^{-1} band may be a sequence or combination band involving excitation of v_3. The combined evidence from the DF spectrum and the rotational structure, coupled with the position of this band in the overall excitation spectrum, suggests that this band may be a 2_1^1 sequence band with unassigned activity in v_3. The close proximity of this band to the 20467/20533 cm^{-1} pair, which were tentatively assigned to $^2\Delta - \tilde{X}^2\Sigma(^2\Pi)\,2_1^1$ transitions, raises the question; is the 20387 band part of the same electronic band system as this pair? It is therefore very tentatively suggested that this band is due to a $\mu\,^2\Sigma^+ - \tilde{X}^2\Sigma(^2\Pi)\,2_1^1$ transition. The μ label has been assigned assuming that this band is associated with the 20467/20533 spin-orbit pair of Δ states. However this assignment indicates a large Renner-Teller splitting, and does not account for the observed activity in v_3.

3.3.9 Summary of findings acquired for all 15 bands.

Table 3.2 contains a summary of all the possible assignments discussed in the sections above and some of the data acquired. Figure 3.14 shows a pictorial representation of the excitation spectrum of BaOH studied in this work together with the most likely assignments.

Table 3.2. A summary of the data acquired and possible assignments for all bands.

Position /cm-1	LIF[a] Data (cm^{-1}) measured from spectra	B from simulation / cm^{-1}. [b]	DF v'' (cm^{-1}) / Vibrational anharmonicity (cm^{-1})	Most likely assignment[c]	Notes and other likely assignments
19892	$\overline{B} = 0.21$ ZG = $1.62\,\overline{B}$	N/A	+662 / -640 0	$\tilde{C}'^{2}\Pi_{1/2} - \tilde{X}^{2}\Sigma^{+}\ 2_2^0$	
19992	$\overline{B} = 0.20$ no ZG	N/A	no DF	$\tilde{C}^{2}\Sigma - \tilde{X}^{2}\Sigma(^{2}\Pi)\ 2_3^1$	μ or $\kappa^{2}\Sigma$
20107	$\overline{B} = 0.20$ ZG = $3.65\,\overline{B}$	N/A	+476?, -667 67	$\tilde{C}^{2}\Delta_{3/2} - \tilde{X}^{2}\Sigma(^{2}\Pi)\ 2_x^1 3_1^1$	$x = 1$ or 3
20179	$\overline{B} = 0.20$ ZG =$6.25\,\overline{B}$	N/A	+480?, -476, -667 67	$\tilde{C}^{2}\Delta_{5/2} - \tilde{X}^{2}\Sigma(^{2}\Pi)\ 2_x^1 3_1^1$	$x = 1$ or 3
20276	$\overline{B} = 0.21$ ZG = $2\,\overline{B}$	N/A	-467, -667 0	$\tilde{C}''^{2}\Pi_{1/2} - \tilde{X}^{2}\Sigma^{+}\ 2_0^0$	Some v_3 character
20356	$\overline{B} = 0.26$ ZG = $4.1B'$	$B'' = 0.2407$ $B' = 0.2419$	-685, -1303 31	$\tilde{C}''^{2}\Pi_{3/2} - \tilde{X}^{2}\Sigma^{+}\ 2_0^0$	
20387	$\overline{B} = 0.22$ no ZG	$B'' = 0.1803(14)$ $B' = 0.1724(17)$	-493, -640 0	$\tilde{C}\mu\,^{2}\Sigma_{1/2} - \tilde{X}^{2}\Sigma(^{2}\Pi)\ 2_1^1$	μ or $\kappa^{2}\Sigma$, some v_3 character

20467	$\overline{B}$ = 0.2 ZG = ~2 or ~4 $\overline{B}$	N/A	-640 0	$\tilde{C}'^2\Delta_{3/2} - \tilde{X}^2\Sigma(^2\Pi)\,2_1^1$	
20533	$\overline{B}$ = 0.20 ZG = 6 $\overline{B}$	N/A	-640 0	$\tilde{C}'^2\Delta_{5/2} - \tilde{X}^2\Sigma(^2\Pi)\,2_1^1$	
20550	$\overline{B}$ = 0.21 ZG = 1.24 B''	B'' = 0.2166 B' = 0.21724(82)	-667 30	$\tilde{C}'^2\Pi_{1/2} - \tilde{X}^2\Sigma^+\,0_0^0$	
20608	$\overline{B}$ = 0.17 ZG = 4.1 B' or 2.9 B'	B'' = 0.17080(38) B' = 0.16485(43)	-667, -1293 35	$\tilde{C}'^2\Pi_{3/2} - \tilde{X}^2\Sigma^+\,0_0^0$	or $\tilde{C}\,^2\Pi_{1/2}$
20931	$\overline{B}$ = 0.21 ZG = 6.1 B'	B'' = 0.20562(46) B' = 0.20614(48)	no DF	$\tilde{C}'x\,^2\Delta_{5/2} - \tilde{X}^2\Sigma(^2\Pi)\,2_1^3$	or $2_2^4\tilde{C}'x\,^2\Phi_{5/2} - \tilde{X}^2\Delta$ $x = \mu$ or κ
20940	$\overline{B}$ = 0.23 ZG = 6.1 $\overline{B}$	N/A	-667, -1267 86	$\tilde{C}'^2\Phi_{5/2} - \tilde{X}^2\Sigma(^2\Delta)\,2_2^4$	μ or $\kappa\,^2\Phi$
20971	$\overline{B}$ = 0.20 ZG = 1.9B'	B'' = 0.21447(98) B' = 0.21047(60)	-480, -699, -969, -1467 30 31	$\tilde{C}'\mu\,^2\Pi_{1/2} - \tilde{X}^2\Sigma^+\,2_0^2$	some ν_3 character
20986	$\overline{B}$ = 0.19 ZG = 3.8 B'	B'' = 0.18764(56) B' = 0.18519(82)	-493, -693, -1320 0	$\tilde{C}'\mu\,^2\Pi_{3/2} - \tilde{X}^2\Sigma^+\,2_0^2$	some ν_3 character

Notes for Table 3.2

(a) ZG = Zero gap measured from the spectrum. The width as a function of B assumes the value of B' determined by simulation where available. Alternatively $\overline{B}$ estimated from the spectrum has been used.

(b) N/A = simulation has not been performed.

(c) All suggested assignments should be viewed as tentative.

(d) The $\widetilde{C}$ state has been given three designations in Table 3.2:

(i) $\widetilde{C}'$, indicating the band is most likely part of an electronic band system with 'origin' transitions at 20550/20608 cm^{-1}.

(ii) $\widetilde{C}''$, indicating the band is most likely part of an electronic band system with 'origin' transitions at 20276/20356 cm^{-1}.

(iii) $\widetilde{C}$, indicating the band could be part of either the $\widetilde{C}'-\widetilde{X}$ or $\widetilde{C}''-\widetilde{X}$ systems.

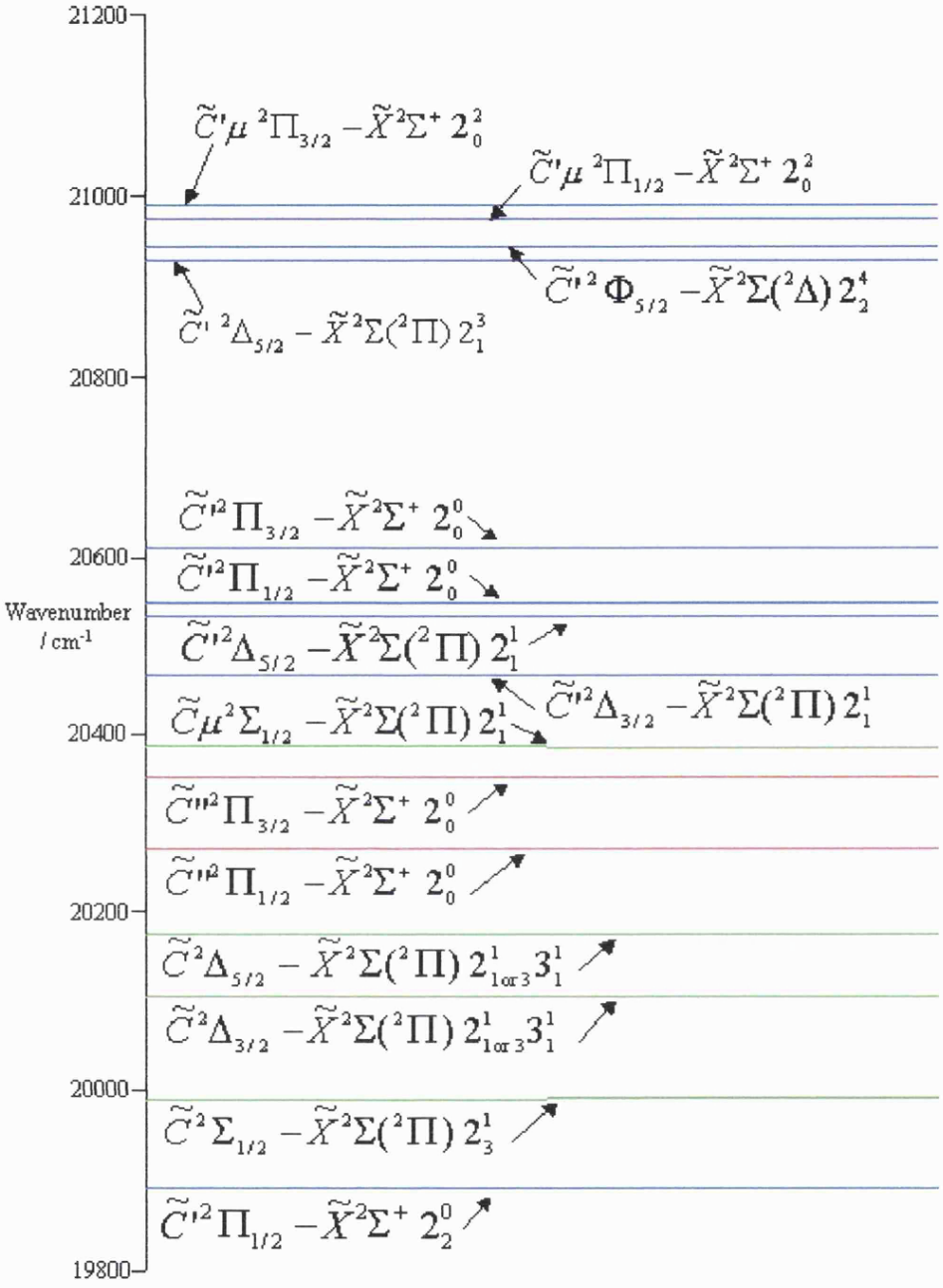

Figure 3.14. Summary of the excitation transitions and their most likely assignments. Blue indicates association with the $\tilde{C}'$ state and red with the $\tilde{C}''$ state. Green indicates the band could be associated with either $\tilde{C}'$ or $\tilde{C}''$ state. See footnotes to Table 3.2 for further information.

3.4 EXCITED ELECTRONIC STATE(S)

The electronic structure of BaOH should be similar to that of the barium monohalides. Electronic transitions for the latter in the same spectral region as that investigated in the present work are well-known.[1] The transitions responsible are the $C\,^2\Pi$-$X\,^2\Sigma^+$ transitions and so one would expect the analogous transition in BaOH to be observed. Many of the bands seen in this work are consistent with a $^2\Pi$-$^2\Sigma^+$ electronic transition, and there is no doubt that the $\widetilde{C}^2\Pi - \widetilde{X}^2\Sigma^+$ system is responsible for much of the structure.

The Renner-Teller effect will add considerable complexity to the vibronic structure in the $\widetilde{C}^2\Pi$ manifold of BaOH. Attempts have been made to use well-known perturbation theory expressions for the Renner-Teller effect to develop an assignment of the spectrum that is consistent with all, or at least most, of the fifteen observed bands. Unfortunately, such an analysis has proved elusive. This may partly be the result of a large Renner-Teller effect, for which the standard perturbation theory expressions will fail. However, there is also the possibility that other electronic states contribute to this spectral region, either indirectly through perturbations or directly through overlap with another optically accessible electronic band system. There is no evidence for the latter in the electronic spectra of BaF and BaCl, where the $\widetilde{C}\,^2\Pi$ state is isolated by several thousand cm^{-1} from the known electronic states immediately above and below. However, in BaF and BaCl no $^2\Delta$ electronic states have been observed. In BaOH, oscillator strength in a $^2\Delta$-$\widetilde{X}\,^2\Sigma^+$ electronic transition could be induced by vibronic coupling, and so it is possible that such a transition might be contributing to the spectra reported in this chapter.

In addition to these possibilities, there is evidence from some bands for Fermi resonance between ν_2 and ν_3. There is also evidence for two pairs of 'origin' spin-

orbit doublets, which would seem to indicate two electronic $\widetilde{C}$ states. However the evidence presented here is in no way conclusive and other possible explanations may be found.

For example, if a transition to a $^2\Delta$ electronic state gained intensity by vibronic coupling then one of the previously identified 'origin' pairs could be due to excitation to this electronic state. A pair of Π vibronic states arise in the v_2'=odd bending vibration of a $^2\Delta$ electronic state. The 20276/20356 cm^{-1} 'origin' pair are the most likely candidates because no other bands in the excitation spectrum have conclusively been associated with them. Whereas for the 20550/20608 cm^{-1} state, it has been possible to tentatively assign seven other bands as part of the same electronic band system.

3.5 CONCLUSIONS

The green electronic band system of BaOH has been investigated in detail for the first time using rotationally-resolved laser excitation spectroscopy and dispersed fluorescence spectroscopy. There is clear evidence that the $\widetilde{C}^2\Pi - \widetilde{X}^2\Sigma^+$ electronic transition is responsible for most if not all of the fifteen bands observed between 19850 and 21000 cm^{-1}. The origin of this system is probably centred at ~22580 cm^{-1}. Although the symmetries of the upper and lower states have been identified for many other bands, in most cases the vibrational assignments are only tentative.

The Renner-Teller effect is presumed to be in operation in the $\widetilde{C}^2\Pi$ state but the Renner parameter (ε) has not been determined. It does not appear that the $\widetilde{C}^2\Pi - \widetilde{X}^2\Sigma^+$ band system is amenable to a standard Renner-Teller analysis. This may be due in part to the magnitude of the Renner parameter which, if large, would

make the standard perturbation theory expressions for the vibronic energy levels inapplicable. However, it is unlikely that a large ε alone is responsible for the inability to satisfactorily explain most of the spectral features. It is also likely that extensive perturbations are active which, to unravel, would require a more detailed and higher resolution study than that carried out here.

3.6 REFERENCES

1. K. P. Huber and G. Herzberg, *Molecular Spectra and Molecular Structure. IV. Constants of Diatomic Molecules* (Van Nostrand Reinhold, New York, 1979).
2. P. F. Bernath, pp.1-62 in *Advances in Photochemistry*, Vol. 23, eds D. C. Neckers, D. H. Volman, and G von Bünau (Wiley, 1997).
3. A. M. Ellis, *Int. Rev. Phys. Chem.* **20**, 551 (2001).
4. S. Kinsey-Nielson, C. R. Brazier, and P. F. Bernath, *J. Chem. Phys.* **84**, 698-708 (1986).
5. W. T. M. L. Fernando, M. Douay, and P. F. Bernath, *J. Mol. Spectrosc.* **144**, 344-351 (1990).
6. H. Haraguchi, S. J. Weeks, J. D. Winefordner, *Spectrochim. Acta A* **35**, 391 (1979).
7. S. J. Pooley, M. S. Beardah, and A. M. Ellis, *J. Elec. Spec. Rel. Phen.* **97**, 77-88 (1998).
8. G. Herzberg, *Molecular Spectra and Molecular Structure. III. Electronic Spectra and Electronic Structure of Polyatomic Molecules* (Krieger, Florida, 1966).
9. Dr Colin Western, personal communication.
10. M. A. Anderson, M. D. Allen, W. L. Barclay Jr, and L. M. Ziurys, *Chem. Phys. Lett.* **205**, 415-422 (1993).
11. L. M. Ziurys, D. A. Fletcher, M. A. Anderson, and W. L. Barclay Jr, *Astrophys. J. Suppl. Series* **102**, 425-434 (1996).
12. J. T. Hougen, *J. Chem. Phys.* **36**, 519-534 (1962).

CHAPTER 4

Background Theory

4. BACKGROUND THEORY

4.1 Schrödinger Equation

In quantum mechanics the Schrödinger equation provides the means for determining the wave function ψ of a particle, or a collection of particles, and the various energy states it (they) can occupy. The time-independent Schrödinger equation can be written in the deceptively simple form

$$H\Psi = E\Psi \qquad (4.1)$$

where H is the Hamiltonian, a differential operator representing the energy, and E is the energy of the system.

In the case of molecules the Hamiltonian is composed of potential and kinetic energy terms for both the nuclei and the electrons in the system. Thus the Schrödinger equation may be written as

$$[T_{\text{nuc}}(R) + T_{\text{el}}(r) + V_{nn}(R) + V_{ne}(R,r) + V_{ee}(r)]\Psi = E_{tot}\Psi(R,r) \qquad (4.2)$$

where $T_{nuc}(R)$ and $T_{el}(r)$ are the kinetic energy operators for the nuclei and electrons, respectively, and R and r are the corresponding nuclear and electron spatial coordinates. $V_{nn}(R)$, $V_{ne}(R, r)$, $V_{ee}(r)$ are the electrostatic potential energies arising from the nucleus-nucleus, nucleus-electron and electron-electron interactions, respectively.

The Schrödinger equation in equation (4.2) cannot be solved exactly for a multi-electron system. However, approximate solutions can be obtained by making a

number of assumptions. First of all, according to the Born-Oppenheimer approximation, the disparity in nuclear and electron masses allows the electron and nuclear motions to be treated independently. This has the effect of removing the nuclear kinetic energy term (nuclear motion is dealt with subsequently if necessary) and calculations can then be performed at fixed nuclear configurations. This approximation, which is usually a very good one, leads to the concept of *potential energy surfaces*.

Secondly, although means are available for including the effects of relativity, it is often acceptable to ignore relativistic effects. This is a good approximation for molecules composed of first and second row atoms and is employed throughout this thesis.

For the electronic part of the wavefunction ($\Phi(R, r)$), the Schrödinger equation reduces to

$$[T_{el}(R) + V_{ne}(R,r) + V_{ee}(r)]\Phi(R,r) = E(R)\Phi(R,r) \qquad (4.3)$$

and the motion of nuclei is governed by the Schrödinger equation

$$[T_{nuc}(R) + V_{nn}(R) + E(R)]\chi(R) = E_{tot}\chi(R) \qquad (4.4)$$

where χ represents the nuclear wavefunction. The nuclear Schrödinger equation (4.4) contains the potential energy term $V_{nn}(R) + E(R)$, which is the potential energy surface of the system. $E(R)$ is the electronic energy obtained by solving the electronic Schrödinger equation, and so the electronic Schrödinger equation must be solved at a range of positions in nuclear coordinate space *before* the nuclear Schrödinger

equation can be solved. Thus solving the electronic Schrödinger equation is the key to all *ab initio* calculations on molecules.[1, 2]

For any given system containing n electrons of mass m_e, charge e, and N nuclei each with charge Z_α, the explicit form of the electronic Schrödinger equation is

$$\left(-\frac{h^2}{8\pi^2 m_e}\sum_{i=1}^{n}\nabla_i^2 - \sum_{i=1}^{n}\sum_{\alpha=1}^{N}\frac{Z_\alpha e^2}{4\pi\varepsilon_0 r_{i\alpha}} + \sum_{i<}\sum_{j}\frac{e^2}{4\pi\varepsilon_0 r_{ij}}\right)\Phi(R,r) = E(R)\Phi(R,r) \qquad (4.5)$$

where the summation indices i and α extend over all electrons and nuclei respectively, $r_{i\alpha}$ is the distance between electron i and nucleus α, r_{ij} is the distance between electrons i and j, and ∇^2 is the Laplacian ($\partial^2/\partial x^2 + \partial^2/\partial y^2 + \partial^2/\partial z^2$). The first two terms describe the electron kinetic energies and the electron-nuclear electrostatic potential energies, respectively. The third term, which describes the repulsion between the electrons, prevents the separation of this equation into n one-electron equations that would be exactly solvable. Consequently, for two or more electron systems, the electronic Schrödinger equation cannot be solved exactly.[1, 2]

4.2 HARTREE-FOCK METHOD

In order to solve the Schrödinger equation for a system containing two or more electrons a further approximation is required. This can be achieved through the concept of *orbitals*, which is a crucial foundation in the current understanding of atomic and molecular structure. In the orbital approximation it is assumed that the overall electronic wavefunction can be expressed as a product of one-electron functions even though, strictly speaking, this is incorrect because of the electron-electron repulsion terms in the Hamiltonian. It is important to recognise that electron-

electron repulsion is *not* ignored by this approximation. Instead, each electron moves under the influence of the average electrostatic field due to the nuclei and all other electrons.

A one-electron function, or orbital, for an electron in an atom or molecule is a function of its position in Cartesian coordinates (x, y and z) and the electron spin (ξ), *i.e.* the wavefunction for an electron is $\psi(x,y,z,\xi)$. ψ^2 represents the probability distribution of the electron in spatial and spin space. Hartree suggested that the wavefunction for an n-electron system may now be formed from the product of the orbitals[1,2]

$$\Psi_{\text{product}} = \psi_1(1)\psi_2(2)...\psi_n(n) \quad . \tag{4.6}$$

Although convenient, the Hartree product wavefunction has a serious deficiency, namely that it does not satisfy the Pauli exclusion principle.

The Pauli exclusion principle states that fermions (such as electrons) must be represented by wavefunctions that are antisymmetric to exchange, *i.e.* no two electrons may be identical. Given that there are only two possible electron spins, this is the reason why there is a maximum of two electrons per orbital. The Pauli exclusion principle may be satisfied by using a determinantal form for the wavefunction, an idea first introduced by Slater.[3, 4]

$$\Psi = \frac{1}{\sqrt{(n!)}} \begin{vmatrix} \psi_1(1)\alpha(1)\psi_1(1)\beta(1) & \psi_2(1)\alpha(1)\cdots\cdots\psi_{n/2}(1)\alpha(1) \\ \psi_1(2)\alpha(2)\psi_1(2)\beta(2) & \psi_2(2)\alpha(2)\cdots\cdots\psi_{n/2}(2)\alpha(2) \\ & \vdots \\ \psi_1(n)\alpha(n)\psi_1(n)\beta(n) & \psi_2(n)\alpha(n)\cdots\cdots\psi_{n/2}(n)\alpha(n) \end{vmatrix} \tag{4.7}$$

In (4.7) Ψ is the total electronic wavefunction, $\psi_i(j)$ is a molecular spin orbital for electron j, α and β represent the two possible electron spins, and n is the total number of electrons. The Slater determinant is convenient because it allows retention of the orbital concept whilst simultaneously satisfying the Pauli principle. Each electron is represented by a row in the Slater determinant and interchange of any two rows, which is equivalent to exchanging two electrons, results in a change of sign of the wavefunction, thus satisfying the Pauli principle. The factor $(n!)^{-1/2}$ preceding the determinant is a normalisation constant.

Hartree-Fock theory is derived from the variation theorem. In the context of molecular orbital theory the variational theorem states that the lowest energy determinantal wavefunction will be closest to the true wavefunction for any given basis set. Thus a method that is said to be variational will never produce an energy lower (more negative) than the energy of the true wavefunction. Thus if a wavefunction is chosen as a starting point, the molecular orbital expansion coefficients (see below) can be optimised until the lowest possible energy is attained. This will give the best approximation to the true solution possible for the trial wavefunction.

In an extension of the earlier work by Hartree, Fock applied the variational theorem to the Slater determinant description of electronic wavefunctions. Differential equations were derived (the Hartree-Fock equations) that have the general form[1, 2, 5]

$$F\psi_i = \varepsilon_i\psi_i \qquad (4.8)$$

where ψ_i represents the ith spin orbital of energy ε_i and F is known as the Fock operator. While the HF equations are solvable, the calculation process is complicated by the fact that F and ψ_i are dependent on one another. In other words it is not possible to determine F without first knowing ψ_i, and vice versa.

The only way to solve the HF equations is by an iterative approach. A guess is made at the orbital wavefunction, which in turn allows the Fock operator to be determined, which in turn allows a new wavefunction to be determined by solving equation (4.8) for each orbital, and so forth. The iteration procedure continues until there is no significant change from one iteration to the next. Because the HF method is variational, the lowest energy is always closest to the true energy. The process is said to converge to a self-consistent field (SCF), hence the whole process is usually referred to as the "SCF procedure".

Electron correlation

The HF method provides a surprisingly accurate description of many different chemically bound species at their equilibrium structures. However, it does have serious weaknesses outside of this regime. The HF method treats electron-electron interactions by the mean field approach, *i.e.* each electron experiences an average repulsive potential created by the averaged positions of the n-1 other electrons. This approach leads to electrons being allowed to approach each other more closely than in reality. In other words the exact wavefunction has a much reduced electron density around the instantaneous position of each electron (a Coulomb hole).[6] This deficiency in the HF description is referred to as electron correlation. Since the true energy of the system is lower than that obtained from the HF method, the difference is referred to as the correlation energy.

Any description of electron correlation must account for both long-range and short-range electron-electron interactions. Most post-HF methods (see below) provide a reasonable description of the long-range effects. However the short-range correlation effects prove to be much more difficult to describe accurately. The short-range (dynamic) electron correlation usually makes up the majority of the electron correlation. The long-range (static) electron correlation can prove to be very important if an electronic state is not adequately described by a single Slater determinant. This usually arises because of the near degeneracy of two or more electronic states.[6]

4.3 POST HARTREE-FOCK METHODS

There are many different methods available that provide a more accurate description of electron-electron interactions than the HF method. The post-HF method used in this work is the coupled cluster method because it provides one of the best computationally viable descriptions of both static and dynamic electron correlation.[6] Discussion in this section will focus entirely on the coupled cluster method.

4.3.1 Coupled cluster (CC)

The coupled cluster method is capable of recovering a large proportion of the electron correlation energy, and is the most accurate correlation method in common use today. The fundamental equation of CC theory is [7-10]

$$\psi_{CC} = e^{\hat{T}}\psi_{HF} \qquad (4.9)$$

where ψ_{CC} is the correlated molecular electronic wavefunction, ψ_{HF} is the normalised HF wavefunction and the exponential $e^{\hat{T}}$ is defined by a Taylor series expansion

$$e^{\hat{T}} = 1 + \hat{T} + \frac{\hat{T}^2}{2!} + \cdots = \sum_{k=0}^{\infty} \frac{\hat{T}^k}{k!} \tag{4.10}$$

$\hat{T}$ is a global electron excitation operator defined as a sum of n-tuple excitation operators

$$\hat{T} = \hat{T}_1 + \hat{T}_2 + \hat{T}_3 + \cdots + \hat{T}_n \tag{4.11}$$

where the maximum value of n is the number of electrons, *i.e.* the maximum number of electrons that can be excited is all of them. It is, however, impractical to excite to a large value of n and thus it is usually kept at 3 or less. The effect of $e^{\hat{T}}$ is to allow all possible combinations of excitations of electrons from occupied to virtual orbitals, restricted by the truncation of $\hat{T}$ (at 3 or less).

$\hat{T}_n$ converts the reference Slater determinant into a linear combination of all singly excited Slater determinants according to variable coefficients, called amplitudes. The aim of a CC calculation is to solve the non-linear equations for the amplitudes contained in each $\hat{T}_n$. Once these are determined, the multideterminantal, many-electron wavefunction is known. Equation (4.11) generates a multideterminantal, many-electron wavefunction, and the exponential form of ψ_{CC} ensures that all higher excitations are included in the wavefunction, although they may be restricted to products of lower order excitations.

There are two features of coupled cluster theory that are particularly worth noting. First, CC theory is size extensive at any given level of truncation. In other words, the method scales correctly with the number of particles in the system. Secondly, CC theory is not variational. A method that is variational (*e.g.* HF) will never underestimate the energy of the wavefunction, whereas this is possible in CC calculations.

When both single and double electron excitations are included in CC theory it is referred to as CCSD, and this results in a reasonable description of electron correlation energy, typically recovering 95 % of the correlation energy. However, including triple excitations (CCSDT) results in a much improved description of electron correlation, typically recovering 99 % of the correlation energy. However it does so at a much increased computational cost.[11] CCSDT calculations are currently just about feasible for systems composed of two or three light atoms. A very useful compromise between the accuracy of CCSDT and the much reduced computational cost of CCSD is to treat the triple order excitations by lowest order perturbation theory and add the resulting terms noniteratively. Denoted CCSD(T), the noniterative, perturbative treatment for the effect of the connected triples provides a computationally cost effective way of achieving an accuracy close to CCSDT.[6]

The CCSD(T) method provides a good description of both static and dynamic electron correlation. The intrinsic error in calculated binding energies of the CCSD(T) method is estimated to be approximately 1 % for chemically bound molecules and up to 3 % for rare gas dimers.[11]

In all of the calculations carried out in this work the so called frozen core approximation has been implemented.[5,12] This means that correlation of the core (non-valence) electrons is not included. The frozen core approximation rests on two

assumptions, namely that the interaction between core and valence electrons is approximately the same in all electronic states and that the interaction between the core and valence electrons can be treated adequately by a mean field approach. This is normally a very good approximation.

4.4 BASIS SETS

The HF equations can be solved either numerically or by basis set expansion techniques. The numerical approach is very accurate but is computationally intractable for all but atoms and small linear molecules, because of the large number of grid points that must be employed. Consequently, all traditional quantum chemical calculations (HF, MP, CC, *etc.*) start with the selection of a one-electron basis set. The quality and accuracy of an *ab initio* calculation depends very highly upon the choice of basis set employed.

A very useful method of describing the many electron wavefunction in a molecule is via molecular orbitals, each of which may be expanded as a number of atom-centred one-electron wavefunctions. This linear combination of atomic orbitals (LCAO) is the starting point for most electronic structure calculations on molecules. An individual molecular orbital ψ_i is expanded as

$$\psi_i = \sum_{\mu=1}^{N} c_{\mu i}\phi_\mu \qquad (4.12)$$

where ϕ_μ is a basis function, N is the number of functions and $c_{\mu i}$ is the molecular orbital expansion coefficient. If an infinite number of functions is used the expansion will be infinitely flexible and an exact description of the molecular orbital is possible.

This limit is known as the complete basis set (CBS) limit. In reality of course a finite number of basis functions must be used and one of the key aspects of *ab initio* calculations is to make a judicious choice of this *basis set.*

In principle the atomic orbitals of the actual atoms in a molecule would be used as the basis functions in (4.12). However for many-electron atoms it is not possible to obtain an exact functional form for atomic orbitals, so an alternative approach must be used. The approach taken is to employ basis functions that have radial and angular properties similar to the orbitals of hydrogenic (1-electron) atoms. In general each basis function is atom centred and the most common are gaussian functions. Gaussian functions are powers of x, y and z multiplied by an $\exp(-\alpha r^2)$, where α is a constant determining the size or radial extent of the function. For example, s and p_x type gaussian functions (4.13 and 4.14 respectively) take the general form[1]

$$g_s(\alpha,r)=\left(\frac{2\alpha}{\pi}\right)^{3/4}\exp(-\alpha r^2) \qquad (4.13)$$

$$g_x(\alpha,r)=\left(\frac{128\alpha^5}{\pi}\right)^{1/4} x\exp(-\alpha r^2) \qquad (4.14)$$

A single gaussian function is often a poor representation of an atomic orbital. Consequently, a single basis function will normally consist of a linear combination of gaussian functions to provide a much improved description of the atomic orbital.[1,2,13] In general the more functions included in a basis set the better the description of the wavefunction and hence the more realistic any calculations carried out with it are

likely to be. The number of basis functions employed per occupied atomic orbital determines the size of the basis set. For example a basis set that uses two basis functions per occupied orbital is termed a double zeta (DZ) basis set. A triple zeta (TZ) basis set has three functions per occupied orbital. In reality these basis sets by themselves are unsuitable for many calculations and additional functions are required to allow the molecular orbitals more flexibility for describing the electron density.

4.4.1 Polarisation functions

Polarization functions can be added to a basis set to allow additional angular flexibility of the orbitals. Polarization functions represent atomic orbitals with higher angular momentum than in the occupied valence atomic orbitals in the ground state of an atom. Thus a suitable polarization function for second row atoms would be a *d* function. In some situations it is necessary to add *f*, *g* or even *h* functions to provide an adequate description of the electron density in a molecule.[1, 2, 5]

4.4.2 Diffuse functions

Diffuse functions can be added to a basis set to allow additional radial flexibility of the atomic orbitals. Diffuse functions represent orbitals of the same angular momentum as the highest occupied atomic orbital in a ground state atom, but are larger radially than functions used to describe the valence orbitals. Diffuse functions are particularly useful in accounting for long-range interactions where it is important to be able to represent the electron density far from the nucleus.[1, 2, 5]

4.4.3 Correlation consistent basis sets

Small basis sets generally lead to a poor description of the dynamic (short range) electron correlation. This results in slow convergence toward the CBS limit as the size of the basis set is increased. This problem can be remedied by the use of very large basis sets with a large number of functions but this, of course, requires enormous computer resources.

Another approach is to develop a series of basis sets designed to systematically approach the CBS limit, thus allowing extrapolation to the CBS limit from computations with smaller basis sets. Dunning *et al.*[11, 14-16] have developed a series of so-called correlation consistent basis sets that do just this by only including functions within a given basis set that lower the correlation energy by at least a set amount.

These basis sets are denoted cc-pV*X*Z, where *X* is the cardinal number of the basis set (*X*=2 for double zeta, 3 for triple zeta, etc.). Polarization functions are automatically included in these basis sets. If desired, a set of standard diffuse functions can be added; these are referred to by an "aug" prefix. The correlation consistent basis sets have been developed up to the very large aug-cc-pV6Z basis set. There are many different extrapolation schemes that have been proposed for this series of basis sets. These are discussed in some detail in Chapter 5. In general these extrapolation schemes use results from calculations using three or four of the largest available cc-pV*X*Z basis sets in the extrapolation procedure. Tests have shown that extrapolations of this kind do indeed produce energies very close to the CBS limit. However they still require the use of large basis sets, which is computationally very expensive. In Chapter 5 a procedure is described which uses only double and triple zeta basis sets and yet still approaches the CBS limit.

4.4.4 Basis set superposition error

Calculations carried out on a molecular system allow total energies to be calculated. In order to calculate the binding energy for a bond or a collection of bonds in a molecule (or complex) the difference between the total energy of the molecule (complex) and the fragments at infinite separation must be carried out. For a diatomic system AB the binding energy ΔE is

$$\Delta E = E_{AB} - E_A - E_B \qquad (4.15)$$

where E_{AB}, E_A and E_B are the energies of the molecule, fragment A and fragment B, respectively.

This simple calculation results in binding energies containing an error known as the basis set superposition error (BSSE). BSSE arises due to the incompleteness of the basis sets used in the calculation. During calculation of the total energy of the complex AB, basis functions from A are superimposed on to those of B in the complex and thus improve the description of both A and B. The BSSE arises because the superposition of functions does not take place for A and B at infinite separation.

A common method to remove the majority of the BSSE is to use the counterpoise procedure, which was developed by Boys and Bernardi.[17] The counterpoise procedure corrects for the BSSE, by using the same superposition of functions as occurred in the complex when calculating the energies of the individual fragments. This is achieved by using a 'ghost' fragment. A 'ghost' of fragment A consists of identical basis functions to fragment A but there are no charges due to the nuclei or electrons present. A 'ghost' fragment therefore consists of mathematical functions only and has no physical interpretation.

Thus the calculation of the counterpoise corrected total energy of fragment B consists of a calculating the total energy of fragment B with the inclusion of a 'ghost' fragment A at the same position it occupied in the complex.[17,18] The total energy of fragment A may be calculated in a similar way.

The binding energy (ΔE^{CP}) of the complex without BSSE may now be calculated as the total energy of the complex (E_{AB}), minus the energies of the fragments ($E_{A(B)}$, $E_{(A)B}$) calculated using the counterpoise procedure.

$$\Delta E^{CP} = E_{AB} - E_{A(B)} - E_{(A)B} \qquad (4.16)$$

In strongly bound molecules the effect of BSSE is usually quite small. However for weakly bound molecules and clusters BSSE can be very significant. It is worth noting that as the size of the basis set increases the BSSE will decrease because the basis sets are approaching the CBS limit.

4.5 CALCULATIONS ON VAN DER WAALS CLUSTERS

Ab initio calculations on van der Waals and other weakly bonded species are challenging because of the weak binding and unusual interactions that dominate the bonding. The total energy of the cluster and of the individual fragments will generally be much larger than the energy of binding (in the order of 10^7 times larger). Therefore even very small percentage errors in calculating the energy of the cluster and fragments will have an enormous effect on the calculated binding energy.[11]

In the case of van der Waals interactions the attractive forces are principally one or more of electrostatic, induction and dispersion forces. Electrostatic interactions occur between two permanent multipole moments, such as dipoles.

Induction interactions occur between a multipole moment and a charge-induced (transient) dipole moment. Dispersion interactions occur between a transient dipole and a much weaker transient dipole induced by the first transient dipole. Electrostatic and induction forces are, to some extent, described in HF calculations. However, dispersion is an electron correlation phenomenon and can only be accounted for in post-HF methods.

Clearly it is imperative to accurately calculate energies in order to describe weak interactions. This is achieved by using a method that provides a good account of electron correlation and by making a careful choice of basis set. A basis set for performing calculations on weakly bound clusters should be as large as is feasible given the computational resources available. Equally important is the inclusion of one or more sets of polarization functions to provide angular flexibility, and one or more sets of diffuse functions for radial flexibility to account for the long range interactions. In work on van der Waals clusters in this thesis the correlation consistent aug-cc-pV*X*Z series of basis sets have been chosen. Further details are provided in Chapter 5.

4.6 VIBRATIONAL FREQUENCY CALCULATIONS (SURVIBTM)

As well as calculating energies, *ab initio* calculations can be used to calculate harmonic vibrational frequencies once a minimum energy structure has been found.

The total energy of a molecule comprising N atoms near its equilibrium structure can be expanded as the truncated Taylor series

$$E = T + V = \frac{1}{2}\sum_{i=1}^{3N} \dot{q}_i^2 + V_{eq} + \frac{1}{2}\sum_{i=1}^{3N}\sum_{j=1}^{3N}\left(\frac{\partial^2 V}{\partial q_i \partial q_j}\right)_{eq} q_i q_j . \qquad (4.17)$$

where V_{eq} is the equilibrium potential energy. The quantity q_i, the mass weighted Cartesian displacement for atom i, with mass m_i, defined in terms of the location (x_i) of the nucleus relative to the equilibrium position, $x_{i,eq}$, is given by

$$q_i = m_i^{1/2}(x_i - x_{i,eq}). \tag{4.18}$$

The classical equations of motion for this system take the form

$$\ddot{q}_j = -\sum_{i=1}^{3N} f_{ij} q_i \qquad j = 1, 2, ..., 3N \tag{4.19}$$

where the quadratic force constants, f_{ij}, are the second derivatives of the potential energy with respect to the mass weighted Cartesian displacements, *i.e.*

$$f_{ij} = \left(\frac{\partial^2 V}{\partial q_i \partial q_j} \right)_{eq}. \tag{4.20}$$

Determination of the force constants is the key information for calculating vibrational frequencies and the f_{ij} may be obtained from *ab initio* calculations. Each f_{ij} may be evaluated by direct analytical second differentiation or by a numerical procedure.

In this work the force constants were extracted from a grid of potential energy points used to define the potential energy surface, which was calculated using Gaussian[5] or Molpro.[12] Using this surface as the starting point, the program SURVIBTM[19] was used to calculate vibrational frequencies. SURVIBTM begins by

fitting the surface using a polynomial function. In particular, a Taylor expansion (the degree is user defined) is used to generate a representation of the potential function in internal coordinates (bond lengths, angles and dihedral angles). From this analytical function, force constants are determined from numerical derivatives. Finally a conventional normal mode analysis is performed (solution of equation (4.19)) to yield vibrational frequencies and vibrational motion eigenvectors.

4.7 REFERENCES

1. W. J. Hehre, L. Radom, P. vR. Schleyer, J. A. Pople, *Ab Initio Molecular Orbital Theory* (1986) Wiley.
2. D. M. Hirst, *A Computational Approach To Chemistry* (1990) Blackwell Scientific.
3. J. C. Slater, *Phys. Rev.*, **34** (1929) 1293.
4. J.C. Slater, *Phys. Rev.*, **35** (1930) 509.
5. Gaussian 94/DFT, Revision B.2, M. J. Frisch, G. W. Trucks, H. B. Schlegel, P. M. W. Gill, B. G. Johnson, M. A. Robb, J. R. Cheeseman, T. Keith, G. A. Peterson, J. A. Montomery, K. Raghavachari, M. A. Al-Laham, V. G. Zakrzewski, J. V. Ortiz, J. B. Foresman, J. Cioslowski, B. B. Stefanov, A. Nanayakkara, M. Challacombe, C. Y. Peng, P. Y. Ayala, W. Chen, M. W. Wong, J. L. Andres, E. S. Replogle, R. Gomperts, R. L Martin, D. J. Fox, J. S. Binkley, D. J. Defrees, J. Baker, J. P. Stewart, M. Head-Gordon, C. Gonzalez and J. A. Pople, Gaussian, Inc., Pittsburgh PA (1995).
6. P Jenson, P. R. Bunker (Eds), *Computational Molecular Spectroscopy* (2000), Wiley.
7. J. Čížek, *J. Chem. Phys.*, **45** (1966) 4526.
8. J. Čížek, *Adv. Chem. Phys.*, **14** (1969) 35.
9. M. Rittby and R. J. Bartlett, *J. Chem. Phys.*, **92** (1988) 3033.
10. J. D. Watts, J. Gauss and R. J. Bartlett, *J. Chem. Phys.*, **98** (1993) 8718.
11. T. H. Dunning, *J. Phys. Chem. A*, **104** (2000) 9062.
12. MOLPRO is a package of *ab initio* programs written by H-J. Werner and P. J. Knowles with contributions from J. Almlof, R. D. Amos, A. Berning, M. J. O. Deegan, F. Eckert, C. Hampel, R. Lindh, W. Meyer, A. Nicklass, K. Peterson,

R. Pitzer, A. J. Stone, P.R. Taylor, M. E. Mura, P. Pulay, M. Schutz, H. Stoll, T. Thorsteinsson and D. L. Cooper.

13. G. H. Grant and W. G. Richards, *Computational Chemistry* (1996), Oxford University Press.

14. T. H. Dunning, *J. Chem. Phys.* **90** (1989) 1007.

15. D. E. Woon and T. H. Dunning, *J. Chem. Phys.*, **98** (1993) 1358.

16. D. E. Woon and T. H. Dunning, *J. Chem. Phys.*, **100** (1994) 2975.

17. S. F. Boys and F. Bernardi, *Molec. Phys.*, **19** (1970) 553.

18. T. V. Mourik, A. K. Wilson, A. Peterson, D. E. Woon and T. H. Dunning, *Adv. Quant. Chem.*, **31** (1999) 105.

19. W. C. Ermler, H. C. Hsieh and L. B. Harding, *Comp. Phys. Comm.*, **51** (1988), 257.

CHAPTER 5

A Modified Form of the Truhlar Extrapolation for Ab Initio Calculations on van der Waals Complexes

5. A MODIFIED FORM OF THE TRUHLAR EXTRAPOLATION FOR *AB INITIO* CALCULATIONS ON VAN DER WAALS COMPLEXES

5.1 INTRODUCTION

Ab initio calculations on van der Waals complexes are notoriously challenging.[1-5] This is particularly so when dispersion is the dominant attractive force. Dispersion is the result of correlated electron motion and cannot be accounted for in a conventional molecular orbital (Hartree-Fock) model. Consequently the weak interaction between the monomers necessitates the use of both a large, flexible basis set and the recovery of a large proportion of the electron correlation energy. Even for relatively small complexes this can make meaningful calculations exceedingly expensive.

Basis set extrapolation schemes offer an alternative and more economic means of approaching the complete basis set limit. These have been widely used for calculations on both chemically bound molecules and more weakly bound species including van der Waals clusters.[6-12] However, one of the difficulties with many basis set extrapolations is the slow convergence with basis set size, which means that large basis sets (quintuple zeta and higher) may be needed to obtain an accurate extrapolation. This is exacerbated for van der Waals clusters since for these species the addition of diffuse functions is essential to describe the long-range attractive forces. Consequently, even if an extrapolation procedure is to be employed, there is the prospect of an expensive set of calculations beforehand.

Recently, Truhlar has described a low cost but highly effective procedure for extrapolating towards the infinite basis set limit.[13] Rather than using

relatively large basis sets to achieve convergence, only the standard correlation consistent double zeta and triple zeta basis sets developed by Dunning and co-workers,[14-16] the cc-pVDZ and cc-pVTZ basis sets, were employed in these calculations. In the original paper the extrapolation procedure was parameterised using two test molecules (H_2O and HF) and an atom (Ne), but a subsequent publication described a far more extensive parameterisation procedure employing 29 small molecules.[17] Truhlar and co-workers found that the bond energies were, on average, within 5 kJ mol^{-1} (420 cm^{-1}) of the complete basis set limit, a result that bettered many calculations performed with sextuple zeta basis sets.

In this work we have investigated the application of Truhlar's extrapolation scheme to van der Waals complexes. The original procedure is found to yield poor results for the van der Waals bond lengths and dissociation energies. However, two alterations to the scheme, (i) addition of a single set of standard diffuse functions to the basis sets, and (ii) inclusion of the counterpoise correction, bring the results into good agreement with complete basis set estimates while imposing only a modest increase in computational expense. The background and results for this work are reported and discussed in this chapter.

5.2 REVIEW OF EXTRAPOLATION PROCEDURES

There are many procedures for extrapolating to the CBS limit from a series of *ab initio* calculations with different basis sets. Most extrapolation schemes extrapolate the correlation part of the energy rather than the total (HF + correlation) energy of the system. Also many extrapolation schemes are designed to be used for a particular chemical system or group of systems. Extrapolation

schemes are nearly always parameterised for a given computational method (e.g. MP2 or CCSD), although many can be reparameterised for an alternative method.

A series of basis sets that converges toward the CBS limit in a smooth manner is clearly best suited for extrapolation. As mentioned previously in Chapter 4, the correlation consistent basis sets introduced by Dunning and co-workers,[14-16] designated (aug)-cc-pV*X*Z and (aug)-cc-CV*X*Z, are known to converge in a smooth and predictable manner toward the CBS limit and are therefore suitable for the application of extrapolation procedures.

There have been several different extrapolation procedures explored for the Dunning basis sets. Halkier *et al.*[18] examined a number of schemes and concluded that one of the most accurate is a least-squares procedure applied to the larger Dunning basis sets. The extrapolation focused on the correlation and extrapolation formulae of the general type,

$$E_X^{corr} = E_\infty^{corr} + AX^{-3} \qquad (5.1)$$

where E_X^{corr} is the correlation energy obtained with the basis set with cardinal number X, and E_∞^{corr} is the basis set limit of the correlation energy. This formula is derived from earlier work[19-21] that relates the highest angular momentum quantum number of a basis set and the correlation energy. In order to apply formula (5.1) to a range of basis sets with consecutive cardinal numbers a least-squares fitting approach was used. Halkier *et al.* used the CCSD(T) method and tested all possible combinations of extrapolations with consecutive Dunning basis sets (which range from $X = 2$ - 6). Their investigation used Ne, H_2O and N_2 as the test species, and for the molecules the structures were fixed at the experimentally

determined values. Estimates of the total energy at the CBS limit determined via CCSD(T)-R12 calculations utilising sextuple zeta basis sets were used as comparisons for extrapolated values. The best extrapolation was found to be the two point fit using the two highest cardinal numbers (5 and 6), giving a standard deviation of 0.52 mE_h in the total energy for the three species considered. The higher the lowest cardinal number used the better the fit. Consequently a five point fit using basis sets with cardinal numbers 2, 3, 4, 5 and 6 was worse than a two point fit using triple and quadruple zeta basis sets. The worst extrapolation of this type was the two point fit using basis sets X=2 and X=3, the standard deviation in that case being 5.22 mE_h. In fact the extrapolations which included the double zeta basis sets were considered to be so poor that Halkier *et al.* recommended that even if calculations with quintuple and sextuple zeta basis sets could not be afforded it was suggested that double zeta results should be omitted from the extrapolation (5.1).

Halkier *et al.* also examined non-linear extrapolations of the general form

$$E_X^{corr} = E^{\infty} + A(X + a)^{-\alpha} \qquad (5.2)$$

where A and α are independent parameters, *i.e.* the value of one has no bearing on the value of the other. This form of extrapolation yielded a better fit to the calculated data but is more complicated because more points are needed and multiple solutions may exist. Halkier and co-workers concluded that the best form of equation (5.2) is very similar to equation (5.1), indicating that a linear fit is nearly optimal. Consequently an extrapolation for the Dunning basis sets of the

form of equation (5.1) with the two largest possible cardinal numbers, avoiding the use $X = 2$.

This type of extrapolation procedure can yield total energies very close to the CBS limit but the use of quintuple and sextuple basis sets means that calculations are computationally very expensive. Such calculations on molecules with a large number of electrons are impractical.

Martin and Taylor[22] investigated three different extrapolation schemes. A Feller-type 3-point extrapolation of the form $E(l) = E_\infty + Ae^{-Bl}$, a 3-point Schwartz-type fit of the form $E = A + B/(l + 0.5)^\alpha$, and a 2-point extrapolation of the form $E = A + B/(l + 0.5)^5$. Here l is the cardinal number of the basis set used and A, B and α are adjustable parameters that must be determined. Their investigation used 15 different species ranging from σ-bonded molecules such as CH_4 through other species with different bonding schemes such as HCN and N_2O, to F_2 which is unbound at the Hartree-Fock (HF) level. The CCSD(T) method was used with augmented and non-augmented cc-pVXZ (X = T, Q and 5) basis sets.

In contrast to the investigation described above by Halkier *et al.*, Martin and Taylor have not only extrapolated the correlation energies but also the HF component of the energy. The convergence behaviour of the HF and correlation energies will, of course be, different and therefore Martin *et al.* used separate extrapolations for each component.

The conclusion reached was that all three extrapolation methods "provide almost identical results", with the Feller-type 3-point extrapolation yielding slightly smaller errors than the other two. The lowest mean absolute error achieved for total atomisation energies was 0.191 mE_h, although the error did vary

for different types of molecule. Noticeably N_2O and F_2 were worst, the error for N_2O being 1.40 mE_h. Again in a similar manner to Halkier, in order to achieve this accuracy the three largest basis sets that were computationally feasible for Martin and Taylor were used (augmented T, Q, and 5 zeta), with geometries optimised using the cc-pVQZ basis set. Use of the aug-cc-pV5Z basis set restricted the size of the molecules that could be investigated; indeed Martin and Taylor were unable to use the quintuple zeta basis set for one of the test species (C_2H_4) for this reason.

Mourik *et al.*[6] investigated the van der Waals rare gas dimers of He, Ne and Ar. As part of that work several extrapolation schemes were investigated as a method for extrapolating their calculated total energies to the CBS limit. CCSD(T) calculations utilising the aug-cc-pV*X*Z series of basis sets were used (*X* = D-6). Mourik *et al.* concluded that extrapolation of the results was possible and that a simple exponential extrapolation of the form $E(n) = E(\infty) + Ae^{-\alpha(X-2)}$ worked best (X is the cardinal number of the basis set, A and α were adjustable parameters to be determined). Again, in order to achieve the highest accuracy Mourik *et al.* recommended omitting the double zeta results and extrapolating only from triple zeta to sextuple zeta.

5.2.1 THE TRUHLAR EXTRAPOLATION

Truhlar[13] has recently reported a new extrapolation procedure for the Dunning basis sets. Truhlar assumed that the total energy converges with basis set size according to

$$E(X) = E^{HF}(X) + E^{cor}(X) = E_{\infty}^{HF} + A^{HF}X^{-\alpha} + E_{\infty}^{cor} + A^{cor}X^{-\beta} \qquad (5.3)$$

where X represents the basis set size ($X = 2$ for double zeta, 3 for triple zeta, etc.). Notice that the above expression includes both the Hartree-Fock and correlation energies. The exponents α and β define the rate of convergence of the Hartree-Fock and correlation energies, E^{HF} and E^{cor} respectively, as a function of basis set size. If E^{HF} and E^{cor} are known for two different basis sets, a simple expression can be derived from (5.1) for the total energy at the infinite basis limit, $E_\infty^{tot} = E_\infty^{HF} + E_\infty^{cor}$. For example, with double and triple zeta basis sets the expression obtained is

$$E_\infty^{tot} = \frac{3^\alpha}{3^\alpha - 2^\alpha} E_3^{HF} - \frac{2^\alpha}{3^\alpha - 2^\alpha} E_2^{HF} + \frac{3^\beta}{3^\beta - 2^\beta} E_3^{cor} - \frac{2^\beta}{3^\beta - 2^\beta} E_2^{cor} \quad (5.4)$$

where E_2 and E_3 are the energies from calculations performed with double and triple zeta basis sets, respectively.

Truhlar selected the two smallest cc-pVXZ basis sets, the double and triple zeta basis sets. The exponents α and β were treated as adjustable parameters in the original paper such that the root mean square difference between the total energy of the complete basis set limit and the value obtained from the above formula was a minimum. Values of α and β were determined as 3.4 and 2.4, respectively, from calculations of the total energies of H_2O, HF and Ne. In a subsequent paper, in which a far larger number of molecules was employed in the parameterisation, the optimum values of α and β were found to be 3.39 and 2.02, respectively, for calculations carried out with the CCSD(T) method.[17] All 29

molecules chosen are chemically bound, *i.e.* weakly bound species were not considered.

In a later paper,[23] Chuang and Truhlar showed that geometries may be optimised at the extrapolated level by extrapolation of the Hessians used to accelerate convergence to a stationary point. This method was applied to H_2O, NH_3 and H_2O_2 using both MP2 and CCSD methods. The procedure was validated by showing that the extrapolated geometries are closer to geometries calculated using a cc-pVQZ basis set than with a cc-pVTZ basis set.

Halkier *et al.*[24] have commented on the above work by Truhlar for extrapolating the Hessians. They note that in some cases for MP2, dissociation energies, bond distances or angles calculated via the Truhlar extrapolation can be further from the aug-cc-pV5Z value than when the cc-pVTZ basis set is used alone. However this is a rather twisted view of the extrapolation procedure as they have not considered CCSD(T) or extrapolation of the total energy, both of which have already been shown to work much better than MP2 calculations where the Hessians have been extrapolated.

5.3 COMPUTATIONAL METHODS

In this work Truhlar's methodology has been applied in calculations on several van der Waals clusters. The CCSD(T) method was chosen for the *ab initio* calculations since it fully accounts for all doubly excited configurations, as well as approximately accounting for triple substitutions. It is therefore expected to recover a large proportion of the correlation energy, an essential prerequisite for calculations on van der Waals clusters. The calculations were carried out using Gaussian 94,[25] and in each calculation only the valence electrons were correlated.

The initial work focussed on Ne_2, NeAr, Ar_2, ArH, ArHF and ArFH. These van der Waals clusters were investigated because comparisons can be made with calculations using very large basis sets performed previously by other workers. Also the five species offer a range of van der Waals binding strengths, thus allowing the flexibility of the Truhlar extrapolation to be tested. Initially the Truhlar approach was employed in its original form, *i.e.* calculations were performed using cc-pVDZ and cc-pVTZ basis sets with α and β equalling 3.4 and 2.4. However, after obtaining very disappointing results (see later), the procedure was altered as follows:

(i) Each basis set was augmented with a single set of standard diffuse functions to give the well-known aug-cc-pVDZ and aug-cc-pVTZ sets.[15]

(ii) A counterpoise correction was applied to the van der Waals interaction energy at both the double and triple zeta levels to account for the basis set superposition error.

Equation (5.4) was then applied to these new data at a specific internuclear separation to generate an extrapolated interaction energy. This was repeated for a series of internuclear separations to generate a numerical van der Waals potential energy curve. Finally, the data were fitted to a polynomial in the van der Waals separation (r-r_e) from which the equilibrium dissociation energy, D_e, and the equilibrium internuclear separation, r_e, were determined.

After obtaining encouraging results, the investigation was extended to nine other van der Waals species, He_2, HeNe, HeAr, HeH, NeH, HeHF, HeFH, NeHF

and NeFH. Dissociation energies and equilibrium bond distances were calculated in the same manner as for the six original test van der Waals species.

5.4 RESULTS

5.4.1 Ne_2, NeAr and Ar_2.

Tables 5.1, 5.2 and 5.3 show the results obtained for Ne_2, NeAr and Ar_2. The CCSD(T) method was used in all calculations. The same trends are present in each table and therefore all three are discussed together. All three tables contain an estimate of the van der Waals dissociation energies and equilibrium bond lengths at the complete basis set (CBS) limit. The CBS values were taken from work by other groups using one or more calculations with very large basis sets.

Inspection of tables 5.1 and 5.3 shows that the original Truhlar extrapolation (denoted "Extrap" in the tables) is a very poor estimate of the CBS limit for D_e of Ne_2 and Ar_2. Indeed for Ne_2 it is actually worse than calculations carried out individually with cc-pVDZ or cc-pVTZ basis sets. For NeAr the standard Truhlar extrapolation D_e gives reasonable agreement with the CBS estimate, but this is taken to be fortuitous given the wild discrepancies for Ne_2 and Ar_2. It is therefore clear from these initial results that the standard Truhlar extrapolation is wholly inadequate for calculations on van der Waals complexes.

Table 5.1. Comparison of calculated dissociation energies (D_e) and equilibrium bond lengths (r_e) for Ne_2.

Basis set / method[a]	D_e / cm^{-1}	r_e / Å
cc-pVDZ	34.07	2.75
cc-pVDZ / c.p.	1.45	3.54
aug-cc-pVDZ	39.35	3.22
aug-cc-pVDZ / c.p.	10.13	3.40
cc-pVTZ	35.80	2.98
cc-pVTZ / c.p.	3.96	3.58
aug-cc-pVTZ	37.75	3.11
aug-cc-pVTZ / c.p.	17.89	3.22
Extrap	46.16	3.00
Extrap / c.p.	5.79	3.54
aug Extrap	37.47	3.05
aug Extrap / c.p.	24.74	3.12
t-aug-cc-pV5Z[b]	48.26	3.03
aug-cc-pV6Z[b]	28.56	3.10
t-aug-cc-pV5Z / c.p.[b]	28.32	3.10
aug-cc-pV6Z / c.p.[b]	26.91	3.11
CBS[b]	28.36	3.10

(a) Original Truhlar extrapolation parameters used, *i.e.* $\alpha = 3.4$, $\beta = 2.4$; c.p. = counterpoise correction; Extrap = Truhlar extrapolation; aug = basis sets that have been augmented with a standard set of diffuse functions.

(b) Data from large basis set calculations in ref. (6). CBS = an estimation of the complete basis set limit by extrapolation of data using very large basis sets.

Table 5.2. Comparison of calculated dissociation energies (D_e) and equilibrium bond lengths (r_e) for NeAr.

Basis set / method[a]	D_e / cm^{-1}	r_e / Å
cc-pVDZ	23.04	3.42
cc-pVDZ / c.p.	1.86	4.25
aug-cc-pVDZ	9.6	3.65
aug-cc-pVDZ / c.p.	16.72	3.83
cc-pVTZ	31.92	3.54
cc-pVTZ / c.p.	6.25	4.09
aug-cc-pVTZ	49.83	3.52
aug-cc-pVTZ / c.p.	30.23	3.62
Extrap	41.49	3.54
Extrap / c.p.	9.85	3.96
aug Extrap	75.80	3.44
aug Extrap / c.p.	41.34	3.51
aug-cc-pV5Z / c.p.[b]	41.35	3.52
aug-cc-pV5Z+bf / c.p. [b], [c]	45.13	3.49
Experimental [d]	45.73	3.46

(a) Original Truhlar extrapolation parameters used, *i.e.* $\alpha = 3.4$, $\beta = 2.4$; c.p. = counterpoise correction; Extrap = Truhlar extrapolation; aug = basis sets that have been augmented with a standard set of diffuse functions.

(b) Data from ref. (26)

(c) bf = indicates basis set is supplemented with a set of bond functions (3s 3p 2d 2f 1g) placed in the middle of the van der Waals bond.

(d) Data from ref. (27).

Table 5.3 Comparison of calculated dissociation energies (D_e) and equilibrium bond lengths (r_e) for Ar_2.

Basis set / method[a]	D_e / cm^{-1}	r_e / Å
cc-pVDZ	19.40	4.15
cc-pVDZ / c.p.	5.48	4.71
aug-cc-pVDZ	77.47	4.02
aug-cc-pVDZ / c.p.	43.34	4.05
cc-pVTZ	37.59	4.07
cc-pVTZ / c.p.	22.16	4.20
aug-cc-pVTZ	94.96	3.81
aug-cc-pVTZ / c.p.	71.29	3.90
Extrap	53.33	3.98
Extrap / c.p.	40.57	3.99
aug Extrap	114.16	3.71
aug Extrap / c.p.	92.46	3.81
t-aug-cc-pV5Z[b]	127.79	3.73
aug-cc-pV6Z[b]	97.85	3.78
t-aug-cc-pV5Z / c.p.[b]	95.37	3.79
aug-cc-pV6Z / c.p.[b]	96.74	3.79
CBS[b]	95.60	3.81

(a) Original Truhlar extrapolation parameters used, *i.e.* $\alpha = 3.4$, $\beta = 2.4$; c.p. = counterpoise correction; Extrap = Truhlar extrapolation; aug = basis sets that have been augmented with a standard set of diffuse functions.

(b) Data from ref. (6). CBS = an estimation of the complete basis set limit by extrapolation of data using very large basis sets.

If the counterpoise correction is introduced the calculated D_e falls dramatically, indicating that a large proportion of the calculated dissociation energy is due to the basis set superposition error. However when counterpoise corrected energies are included in the Truhlar extrapolation, very poor underestimates for D_e are obtained for all three dimers. Clearly these basis sets are simply too deficient for any meaningful extrapolation for van der Waals complexes.

An obvious failing of the cc-pVDZ and cc-pVTZ basis sets is that they do not provide sufficiently diffuse basis functions for calculations on weakly bound species. Diffuse functions are likely to be essential to account for the long range nature of dispersion forces. Consequently, the calculations on Ne_2, NeAr and Ar_2 were repeated using the standard single set of diffuse functions provided within the Dunning correlation-consistent basis sets. For Ne and Ar, this adds three contracted functions at the double zeta level (1s, 1p, 1d), and four at the triple zeta level (1s, 1p, 1d, 1f). These basis sets are referred to as aug-cc-pVDZ and aug-cc-pVTZ, a standard notation.

Without a counterpoise correction, the dissociation energies calculated with these enhanced basis sets are still disappointing (aug-cc-pV*X*Z/c.p. in tables 5.1-5.3). However, when the counterpoise correction is included along with the augmented basis sets then the extrapolation does much better, *i.e.* it is within 15 % of the CBS limit for all three clusters. In other words, the extrapolation is an improvement on the individual aug-cc-pVDZ and aug-cc-pVTZ calculations, as one would hope for an extrapolation procedure. It is also interesting to note that for all three clusters the extrapolation procedure gives dissociation energies below the CBS value, and the D_e for the aug-cc-pVDZ calculation is lower than for

aug-cc-pVTZ calculation. *i.e.* the trend from double zeta through triple zeta to the extrapolated value is to approach from below the CBS value and slightly underestimate it.

The inclusion of a set of diffuse functions to the cc-pVDZ and cc-pVTZ basis sets requires only modest increases in computational resources so the essence of a relatively cheap calculation, the original spirit of the Truhlar extrapolation, is maintained in the augmented scheme.

Considering the very modest basis sets used it is worth making a comparison with calculations done by other workers with much larger basis sets. For Ne_2 the modified Truhlar extrapolation yields a D_e which is only slightly worse than a counterpoise corrected aug-cc-pV6Z calculation, a highly encouraging result. Similar findings are made for NeAr and Ar_2. It is clear from tables 5.1, 5.2 and 5.3 that our modified version of the Truhlar extrapolation, while not yielding dissociation energies quite as good as calculations using augmented quintuple and sextuple basis sets, nevertheless comes close to achieving a comparable accuracy.

Analogous conclusions may be drawn for the equilibrium bond lengths. For all three van der Waals dimers the Truhlar extrapolation in its original form does rather poorly. *i.e.* the accuracy of the bond lengths varies from 0.08 Å to 0.17 Å, as well as both underestimating (Ne_2) and overestimating (NeAr and Ar_2). Counterpoise correction, or augmentation of the basis set with a set of diffuse functions, individually does not always improve the accuracy of r_e. However, when both are included within the Truhlar extrapolation procedure the estimated equilibrium bond distances are always closer to the CBS limit r_e than either of the counterpoise corrected aug-cc-pVDZ or aug-cc-pVTZ basis set calculations. For

Ne_2 and Ar_2, the modified Truhlar extrapolation is the same as the CBS limit to the level of accuracy that the CBS limit has been quoted in the original reference.[6] For NeAr the modified Truhlar extrapolation is 0.05 Å higher than the experimental value.[27]

In the calculation of bond lengths the modified Truhlar extrapolation compares favourably with results from large basis set calculations. For Ne_2 and Ar_2 the modified Truhlar extrapolation is equal to or better than any of the quoted calculations using large basis sets. For NeAr the modified Truhlar extrapolation is of a similar accuracy (0.01 Å better) to a counterpoise corrected aug-cc-pV5Z calculation.

5.4.2 ArH.

As a further test of the Truhlar extrapolation and the modifications described above calculations were extended to include ArH.

ArH has been well studied previously with high level calculations using large basis sets.[7] ArH is an open-shell complex and it is interesting to ascertain whether the modified Truhlar extrapolation provides a satisfactory description of such species.

Table 5.4 shows the results obtained in the present work for ArH together with those from other groups using calculations with large basis sets. The original Truhlar extrapolation parameters of $\alpha = 3.4$ and $\beta = 2.4$ were used. Similar to the situation for Ne_2, NeAr and Ar_2, the Truhlar extrapolation in its original form performs poorly. Counterpoise correction greatly reduces the calculated dissociation energies. Additional diffuse functions on the basis sets by themselves do not produce good estimates of D_e or r_e.

Table 5.4. Comparison of calculated dissociation (D_e) and equilibrium bond lengths (r_e) for ArH.

Basis set / method[(a)]	D_e / cm^{-1}	r_e / Å
cc-pVDZ	4.6	4.14
cc-pVDZ / c.p.	0.55	5.1
aug-cc-pVDZ	-8.24	3.82
aug-cc-pVDZ / c.p.	14.84	3.92
cc-pVTZ	9.47	4.02
cc-pVTZ / c.p.	4.08	4.28
aug-cc-pVTZ	34.22	3.61
aug-cc-pVTZ / c.p.	24.24	3.71
Extrap	13.78	3.92
Extrap / c.p.	8.93	3.96
aug Extrap	63.73	3.50
aug Extrap / c.p.	31.95	3.60
d-aug-cc-pV5Z / c.p.[(b)]	32.40	3.61
aug-cc-pV5Z+bf' / c.p.[(b)]	33.22	3.60
"Best Estimate" [(b)]	33.76	---

(a) Original Truhlar extrapolation parameters used, *i.e.* $\alpha = 3.4$, $\beta = 2.4$; c.p. = counterpoise correction; Extrap = Truhlar extrapolation; aug = basis sets that have been augmented with a standard set of diffuse functions.

(b) Data from ref. (7). CBS = an estimation of the complete basis set limit by extrapolation of data using very large basis sets.
bf' = indicates basis set is supplemented with a set of bond functions (6s, 6p, 6d, 3f, 1g, 1h) placed in between the atoms.

However use of both counterpoise correction and additional diffuse functions along with the Truhlar extrapolation produces a dissociation energy within 2 cm^{-1} (~5 %) of the CBS limit. This value is slightly worse than calculations carried out with counterpoise corrected quintuple basis sets with either two sets of additional diffuse functions or a large set of additional bond functions. The equilibrium bond distance calculated by the modified Truhlar extrapolation is the same (to within 0.01 Å) as the CCSD(T) calculation using an aug-cc-pV5Z basis set with a large number of additional bond functions.

The data presented in table 5.4 for ArH suggests that the Truhlar extrapolation in its modified form is also suitable for calculations on open-shell van der Waals species, although calculations on additional species are required to confirm this.

5.4.3 ArHF and ArFH

ArHF and ArFH are complexes containing a van der Waals bond and the highly ionic H-F bond. They are isomers and are both known to correspond to true minima on the potential energy surface.[8, 28] Use of the modified Truhlar extrapolation to calculate dissociation energies and equilibrium bond distances will provide further robust testing of the reliability of the modified version of the Truhlar extrapolation.

Table 5.5. Comparison of calculated dissociation energies (D_e) and equilibrium bond distances (r_e) for ArFH.

Basis set / method[a]	D_e / cm^{-1}	r_e (Ar-F)/ Å
cc-pVDZ	47.79	3.39
cc-pVDZ / c.p.	8.62	4.07
aug-cc-pVDZ	132.49	3.41
aug-cc-pVDZ / c.p.	48.23	3.57
cc-pVTZ	68.79	3.41
cc-pVTZ / c.p.	16.4	3.4
aug-cc-pVTZ	103.14	3.34
aug-cc-pVTZ / c.p.	74.27	3.42
Extrap	88.50	3.38
Extrap / c.p.	41.43	3.42
aug Extrap	99.72	3.29
aug Extrap / c.p.	92.92	3.34
aug-cc-pVQZ[b]	102.18	3.344
aug-cc-pVQZ / c.p.[b]	86.22	3.374
d-aug-cc-pVQZ / c.p.[b]	92.89	3.369
CBS[b]	94.22	3.367

(a) Original Truhlar extrapolation parameters used, *i.e.* $\alpha = 3.4$, $\beta = 2.4$; c.p. = counterpoise correction; Extrap = Truhlar extrapolation; aug = basis sets that have been augmented with a standard set of diffuse functions. HF bond distance fixed at 0.918 throughout all calculations in this work.

(b) Data from ref. (8). CBS = an estimation of the complete basis set limit by extrapolation of data using very large basis sets. H-F equilibrium distance calculated to be 0.918 Å.

Table 5.6. Comparison of calculated dissociation energies (D_e) and equilibrium bond distances (r_e) for ArHF.

Basis set / method[a]	D_e / cm^{-1}	r_e (Ar-H)/ Å
cc-pVDZ	169.89	2.72
cc-pVDZ / c.p.	57.04	2.95
aug-cc-pVDZ	264.15	2.65
aug-cc-pVDZ / c.p.	124.75	2.8
cc-pVTZ	201.2	2.56
cc-pVTZ / c.p.	99.37	2.75
aug-cc-pVTZ	300.58	2.51
aug-cc-pVTZ / c.p.	181.90	2.61
Extrap	241.76	2.47
Extrap / c.p.	148.18	2.57
aug Extrap	334.66	2.45
aug Extrap / c.p.	228.23	2.51
aug-cc-pVQZ[b], [c]	250.49	2.520
d-aug-cc-pVQZ / c.p.[b], [c]	203.74	2.577
aug-cc-pV5Z / c.p.[b], [d]	206.38	2.56
CBS[b], [d]	210.98	2.56

(a) Original Truhlar extrapolation parameters used, *i.e.* $\alpha = 3.4$, $\beta = 2.4$; c.p. = counterpoise correction; Extrap = Truhlar extrapolation; aug = basis sets that have been augmented with a standard set of diffuse functions. HF bond distance fixed at 0.918 throughout all calculations in this work.

(b) Data from ref. (8). CBS = an estimation of the complete basis set limit by extrapolation of data using very large basis sets.

(c) H-F equilibrium distance calculated to 0.919 Å.

(d) H-F equilibrium distance calculated to be 0.918 Å.

Tables 5.5 and 5.6 show the results of calculations on ArFH and ArHF. The original Truhlar extrapolation parameters of $\alpha = 3.4$ and $\beta = 2.4$ were used. The optimum geometry of the complex was first determined by geometry optimisations using the triple zeta basis set (no extrapolation). These calculations showed the preferred geometry to be linear and the HF bond distance to be 0.918 Å (3 d.p.), in line with the previous calculations using large basis sets.[8] Thus for both ArHF and ArFH the H-F bond distance was fixed at 0.918 Å and the geometry was constrained to be linear. Similar to the findings in the previous sections, the Truhlar extrapolation in its original form performs poorly in terms of calculating van der Waals dissociation energies and bond lengths. However, when a set of standard diffuse functions and the counterpoise correction are both used then the modified extrapolation procedure gives results approaching the CBS limit.

The calculated dissociation energy for ArFH is within 1.5 % (< 2 cm^{-1}) of the CBS limit, which is closer than the only other large basis set calculation available for comparison (counterpoise corrected CCSD(T) calculations with a d-aug-cc-pVQZ basis set). The equilibrium bond distance is actually slightly worse than the quadruple zeta calculation, but is within 0.03 Å of the CBS limit.

For ArHF, the modified Truhlar extrapolation yields worse results than for ArFH. However, the modified Truhlar extrapolation is an improvement on the individual aug-cc-pVDZ and aug-cc-pVTZ calculations. For the dissociation energy the modified Truhlar extrapolation is within approximately 8 % (17.25 cm^{-1}) of the CBS limit. The equilibrium bond distance is within 0.04 Å of the CBS limit. These values for D_e and r_e are actually quite a bit worse than the quintuple zeta (5Z) calculations included in table 5.6 for comparison. Possible

reasons for these slightly larger discrepancies for ArHF compared to ArFH are discussed in detail later.

5.4.4 SENSITIVITY TO β

Since α and β are empirical parameters it is natural to query the effect these have on the calculated results. The values used for α and β in the results presented so far were those taken from the initial study by Truhlar on two chemically bound molecules and 1 atom,[17] yielding values of α = 3.4 and β = 2.4. While these values are optimum for that small set of species, it is not obvious that they will also be optimum for weakly bound species. Since in this work the interest is in binding dominated by dispersion forces, which derive from electron correlation, it is the effect of β on D_e and r_e that has been explored, leaving α at its original value.

Table 5.7 summarises the findings. The value for β is seen to have a substantial effect on the computed parameters. For all of the clusters a decrease in β results in an increase in D_e and a corresponding decrease in r_e. For the rare gas dimers and ArH a choice of β = 2.0 - 2.2 is fairly close to optimum when judged against the CBS limit. This choice is also adequate for ArFH, although a larger β of ~2.35 is optimum. The ArHF isomer is the odd one out amongst the test complexes since, in terms of optimising β alone, a large value, in excess of 3.0, is necessary to bring the extrapolated and CBS dissociation energies into close agreement. This is evidence that, as one might have expected beforehand, a single value of β will not suit all situations.

If the odd result of ArHF is set aside for the moment, the above results suggest that a value for β of around 2.0 - 2.2 would be better than the previously

chosen 2.4. A later study by Fast, Sánchez and Truhlar on 29 chemically bound molecules[17] led to a slight change in the suggested empirical parameters to α = 3.4 and β = 2.0. This is concurrent with our findings that a β value of around 2.0 would suit our test set of van der Waals clusters reasonably well.

The calculations for ArHF are at odds with the above conclusion and require further explanation. In particular when a β = 2.0 is used the modified extrapolation yields a D_e 15% above the CBS limit and is clearly much worse than the other complexes. The reason for the relatively large discrepancy for ArHF is not entirely clear. However, a noteworthy difference between ArHF and the other clusters mentioned above, including the ArFH isomer, is that in ArHF there is a substantial contribution to the binding from induction forces in addition to dispersion.[29] An exact treatment of the electrostatic forces would require a complete description of the permanent electric moments of HF and moments induced in both Ar and HF through the various order polarisabilities. A finite basis set will obviously be deficient in this regard. Furthermore, as shown by Fowler and Buckingham,[30] an incomplete basis set can give rise to a spurious electrostatic interaction caused by use of the counterpoise correction. This effect is due to the artificial dipole moment gained by the argon atom in the presence of the ghost orbitals of HF. Interaction of this dipole moment with HF stabilises the cluster, leading to an overestimate of the binding energy. It therefore seems likely that most of the discrepancy between the dissociation energy of ArHF obtained in this work and the CBS limit results from an inadequate description of the induction energy.

Table 5.7. Dissociation energies (D_e in cm^{-1}) and equilibrium bond lengths (in parentheses; Å) as a function of β.

	β										
	1.8	1.9	2.0	2.1	2.2	2.3	2.4	2.6	3.0	3.4	CBS (a)
Ne_2	29.0 (3.066)	28.0 (3.076)	27.2 (3.086)	26.5 (3.094)	25.8 (3.102)	25.3 (3.109)	24.7 (3.115)				28.4 (3.10)
NeAr		46.6 (3.475)	45.3 (3.485)	44.2 (3.493)	43.1 (3.501)	42.2 (3.508)	41.4 (3.514)				45.2 (3.49)
Ar_2		102.4 (3.772)	99.9 (3.782)	97.7 (3.791)	95.7 (3.799)	94.0 (3.806)	92.4 (3.812)				95.7 (3.81)
ArH		35.8 (3.556)	34.8 (3.567)	34.0 (3.577)	33.2 (3.586)	32.6 (3.594)	32.0 (3.601)				33.5 (3.60)
ArHF		247.0 (2.490)	242.4 (2.497)	238.3 (2.502)	234.5 (2.507)	231.3 (2.512)	228.2 (2.516)	223.1 (2.524)	215.3 (2.536)	209.6 (2.544)	210.9 (2.58)
ArFH		102.0 (3.313)	99.9 (3.320)	98.0 (3.326)	96.3 (3.332)	94.9 (3.338)	93.5 (3.343)				94.2 (3.37)

(a) Estimates for the complete basis set limit. For sources of these data see tables 5.1-5.6.

Table 5.8. Dissociation energies and equilibrium internuclear separations for Ne_2, NeAr, and Ar_2

Cluster	Methodology [a]	D_e/cm^{-1}	r_e/Å
Ne_2	Original Truhlar extrap.	49.8	3.00
	aug-cc-pVDZ + cp	10.1	3.41
	aug-cc-pVTZ + cp	17.9	3.22
	Modified Truhlar extrap.	27.2	3.12
	CBS [b]	28.4	3.10
NeAr	Original Truhlar extrap.	45.9	3.53
	aug-cc-pVDZ + cp	16.7	3.83
	aug-cc-pVTZ + cp	30.2	3.62
	Modified Truhlar extrap.	45.3	3.48
	CBS [c]	45.2	3.49
Ar_2	Original Truhlar extrap.	60.6	3.94
	aug-cc-pVDZ + cp	43.4	4.05
	aug-cc-pVTZ + cp	71.4	3.90
	Modified Truhlar extrap.	99.9	3.78
	CBS [b]	95.7	3.81

(a) Original Truhlar extrap. = extrapolation using equation (2) with cc-pVDZ and cc-pVTZ basis sets and no counterpoise correction; aug-cc-pVDZ + cp and aug-cc-pVTZ + cp refer to calculations performed with these extended basis sets and inclusion of the counterpoise correction; modified Truhlar extrap. refers to the combined use of the results from aug-cc-pVDZ + cp and aug-cc-pVTZ + cp calculations in the extrapolation. $\alpha = 3.4$ and $\beta = 2.0$.

(b) From ref. (6).

(c) From ref. (26). These data refer to results from CCSD(T) calculations using an aug-cc-pV5Z basis set with added bond functions and should therefore be very close to the CBS limit.

Table 5.9. Van der Waals dissociation energies and equilibrium internuclear separations of ArH, ArHF, and ArFH.

Cluster	Methodology [a]	D_e/cm^{-1}	r_e/Å
ArH	Original Truhlar extrap.	15.8	3.87
	aug-cc-pVDZ + cp	14.8	3.92
	aug-cc-pVTZ + cp	24.2	3.71
	Modified Truhlar extrap.	34.8	3.57
	CBS [b]	33.8	3.60
ArHF	Original Truhlar extrap.	258.4	2.46
	aug-cc-pVDZ + cp	124.9	2.79
	aug-cc-pVTZ + cp	181.9	2.61
	Modified Truhlar extrap.	242.4	2.50
	CBS [c]	210.9	2.58
ArFH	Original Truhlar	97.9	3.36
	aug-cc-pVDZ + cp	48.3	3.57
	aug-cc-pVTZ + cp	74.4	3.42
	Modified Truhlar extrap.	99.9	3.32
	CBS [c]	94.2	3.37

(a) Original Truhlar extrap. = extrapolation using equation (2) with cc-pVDZ and cc-pVTZ basis sets and no counterpoise correction; aug-cc-pVDZ + cp and aug-cc-pVTZ + cp refer to calculations performed with these extended basis sets and inclusion of the counterpoise correction; modified Truhlar extrap. refers to the combined use of the results from aug-cc-pVDZ + cp and aug-cc-pVTZ + cp calculations in the extrapolation. $\alpha = 3.4$ and $\beta = 2.0$.

(b) From ref. (7)

(c) From ref. (8)

Tables 5.8 and 5.9 show dissociation energies and bond lengths for the six test van der Waals clusters obtained with values of 3.4 and 2.0 for α and β, respectively. For all except ArHF and ArFH the change of β from the value of 2.4 used earlier to the new recommended value of 2.0 has brought the extrapolated dissociation energies closer to the CBS limit. In all complexes except ArHF the D_e are within 6 % of the CBS limit or better. The calculated equilibrium bond distances are all within 0.1 Å of the CBS limit even for ArHF. However for all except ArHF and ArFH the bond distances are within 0.03 Å of r_e at the CBS limit. Importantly, for all clusters except ArHF, the modified Truhlar extrapolation is closer to the CBS limit for D_e and r_e than the aug-cc-pVTZ basis set. Consequently, although caution is likely to be warranted in certain cases, the results presented here suggest that extrapolation using the more recent values of α and β proposed by Truhlar and co-workers[17] of $\alpha = 3.4$ and $\beta = 2.0$ are also applicable to a wide range of van der Waals complexes.

It is encouraging that the extrapolation procedure is robust enough to offer significant improvements over aug-cc-pVTZ for a β parameter that has not been optimised for van der Waals clusters. Indeed even the original values determined from two molecules and an atom by Truhlar were acceptable (but not ideal) for the van der Waals clusters covered in the present work.

5.4.5 *He_2, HeNe, HeAr.*

The six van der Waals complexes described above were used to assess the applicability of the modified Truhlar extrapolation to van der Waals species. To provide a more extensive testing ground, other van der Waals complexes were subsequently considered. In this section He_2, HeNe and HeAr are considered, and table 5.10 shows the results.

Once again it is clear that again the original Truhlar extrapolation performs poorly for all three dimers. However the modified Truhlar extrapolation yields excellent estimates for D_e, within 1 cm^{-1} of the CBS limit in all three cases. Furthermore, the r_e is within 0.035 Å of the CBS value. Clearly these results provide further evidence that the modified Truhlar extrapolation is suitable for van der Waals complexes.

Table 5.10. Van der Waals dissociation energies and equilibrium internuclear separations of He_2, HeNe and HeAr.

Molecule	Basis Set / Method[a]	D_e/cm-1	r_e (Å)
He_2	Extrap	3.04	3.27
	aug-cc-pVDZ / c.p.	4.08	3.18
	aug-cc-pVTZ / c.p.	5.93	3.04
	Extrap aug / c.p.	7.91	2.94
	CBS [b]	7.65	2.965
HeNe	Extrap	21.44	2.97
	aug-cc-pVDZ / c.p.	6.21	3.30
	aug-cc-pVTZ / c.p.	10.32	3.12
	Extrap aug / c.p.	15.01	3.00
	CBS [b]	14.50	3.035
HeAr	Extrap	10.88	3.75
	aug-cc-pVDZ / c.p.	10.14	3.76
	aug-cc-pVTZ / c.p.	15.57	3.59
	Extrap aug / c.p.	21.38	3.48
	CBS [b]	20.58	3.478

(a) See footnote to table 5.8 for description of various methods.

(b) Complete basis set estimate taken from ref. (26)

5.4.6 *HeH and NeH*

Following on from the earlier calculations presented for ArH, similar calculations were carried out on the open shell dimers HeH and NeH. Table 5.11 compares the modified Truhlar extrapolation with calculations by other workers using large basis sets.[7, 31, 32]

For HeH the calculated dissociation energy in the present work is within 7% of the "best estimate" obtained by Partridge and Bauschlicher[7]. Our value is closer than a CCSD(T) calculation carried out using an aug-cc-pV5Z basis set, and only 0.2 cm^{-1} worse than a calculation using a large set of bond functions along with the aug-cc-pV5Z basis set. The equilibrium bond distances are the same to within 0.01 Å for the modified Truhlar extrapolation and the two quintuple zeta calculations.

For NeH, the dissociation energy is 0.86 cm^{-1} lower (7 %) than the experimental value[32] and only 1.02 cm^{-1} less than the "best estimate" as given in the work by Partridge *et al.*[31] r_e is the same as the "best estimate" and only 0.01 Å larger than the experimental value.

Table 5.11. Van der Waals dissociation energies and equilibrium internuclear separations of HeH and NeH.

Molecule	Basis Set / Method[a]	D_e/cm^{-1}	r_e/Å
HeH	aug-cc-pVDZ c.p.	2.55	3.80
	aug-cc-pVTZ c.p.	3.79	3.61
	Extrap aug c.p.	4.74	3.53
	aug-cc-pV5Z [b]	4.54	3.53
	aug-cc-pV5Z + bf [b]	4.97	3.53
	"Best Estimate" [b]	5.07	--
NeH	aug-cc-pVDZ c.p.	4.5	3.79
	aug-cc-pVTZ c.p.	8.13	3.55
	Extrap aug c.p.	11.16	3.44
	"Best Estimate" (1993) [c]	12.18	3.44
	aug-Stuttgart / c.p.[d], [e]	10.97	3.45
	Experiment [d]	12.02	3.43

[a] See footnote to table 5.8 for a description of various methods.

[b] Data from ref. (7). No value is available for the "Best estimate" r_e.

[c] Data from ref. (31).

[d] Data from ref. (32).

[e] aug-Stuttgart = use of the extended [6s, 6p, 6d, 6f] basis set for Ne and aug-cc-pVQZ basis set for H.

5.4.7 NeHF and NeFH

Reliable estimates of the CBS limit are unavailable for NeHF and NeFH so table 5.12 compares the results from the present calculations with two other works, a CEPA (coupled electron pair approximation) calculation by O'Neil *et al.*[33] and a study by Meuwly and Hutson[34] that morphs *ab initio* data to get a better fit with experimental parameters.

Before comparing the results from the present work with calculations performed by other groups it is worth considering the earlier work in some detail. The CEPA calculations of O'Neil *et al.* were carried out using a basis set that was specifically designed by these workers for NeHF. The O'Neil basis set is of a similar size to an aug-cc-pVTZ basis set but should provide a better description for NeHF.

The morphing study by Meuwly *et al.* attempted to take good *ab initio* potentials and modify them slightly to fit the available experimental data. The infrared experimental data consists of the rovibrational line positions spacing for both isomers of NeHF and of NeDF; however most information is available for the isomers Ne-HF and Ne-FD. It should be noted that Meuwly and Hutson comment that the potentials have primarily been fitted to spectroscopic data from DF to supplement the experimental data on the trimers. The morphing procedure attempts to achieve agreement with experiment by making changes that are as small as possible. However the degree that any single point of the *ab initio* surface is moved is at the discretion of the individual doing the fitting and is based on "physical understanding and intuition".[34] Meuwly *et al.* morphed several potentials: entirely *ab initio* CCSD(T) with aug-cc-pVDZ and with aug-cc-pVTZ basis sets; *ab initio* potentials from CCSD(T) and MP2 calculations

utilising the O'Neil basis set (described above); and the CEPA calculation using the O'Neil basis set included in table 5.12.

All of the morphed potentials yielded reasonably similar values for D_e and r_e, with the aug-cc-pVDZ case being noticeably the worst. The morphed potential using the CEPA calculation of O'Neil should be more accurate than the CEPA calculation alone. However, Meuwly *et al.* concluded that the most accurate of their potentials was probably that based on CCSD(T) calculations using the O'Neil basis set, and is the one yielding the results shown in table 5.12. This conclusion was reached by comparing how little the original potential surface had required changing to fit the experimental data. The major drawback with this study is that the largest amount of experimental data available is for the $v = 1$ vibrational state of DF and, consequently, Meuwly and Hutson admit that there is at present insufficient data on NeHF and NeDF for the morphed potentials to be reliable.

For NeHF the modified Truhlar extrapolation yields a D_e that is similar to the morphed potential, the difference being less than 2 cm^{-1}. In contrast, the discrepancy for the CEPA calculations is much larger, over 22 cm^{-1}. For r_e the morphed potential is 0.02 Å lower than the current work, while the CEPA calculation gives an r_e some 0.06 Å higher. For NeFH, our calculated D_e is midway between the CEPA calculation and the morphed potential, 6 cm^{-1} above the former and 5 cm^{-1} below the latter. The equilibrium bond distances for all three methods are within 0.1 Å with the value from the present work being the shortest, indicating that the calculated bond length is likely to be quite reliable.

Table 5.12. Van der Waals dissociation energies and equilibrium internuclear separations of NeHF and NeFH

Molecule	Basis Set / Method[a]	D_e/cm^{-1}	$r_e/Å$[b]
NeHF	aug-cc-pVDZ c.p.	57.3	2.43
	aug-cc-pVTZ c.p.	73.81	2.41
	Extrap aug c.p.	87.68	2.38
	CEPA calc [c]	65	2.44
	Morphed potential [d]	89	2.36
NeFH	aug-cc-pVDZ c.p.	23.29	3.3
	aug-cc-pVTZ c.p.	35.4	3.11
	Extrap aug c.p.	46.00	3.02
	CEPA calc [c]	39	3.104
	Morphed potential [d]	51	3.03

(a) See table 5.8 for a description of the various methods.

(b) r_e = Ne-H bond distance in NeHF and, Ne-F bond distance in NeFH. The H-F distance was fixed at 0.918 Å in this work.

(c) Data from ref. (33). HF was fixed at 0.917 Å.

(d) Data from ref. (34). HF was fixed at 0.917 Å.

There are clearly differences between our values and those of the other two studies and to some extent these can be explained. Counterpoise corrections were not made for either the CEPA nor any of the calculations used in the morphed potentials, and this may partly explain the differences. Secondly the inadequacies of the morphed potential may reflect insufficient experimental data being available to reliably construct empirical potential surfaces, particularly for the potential minimum D_e and not D_0. As commented earlier there is some IR data suitable for parameterising the Ne-HF minimum and the Ne-FD minimum but little elsewhere. Also Meuwly and Hutson found it necessary to employ data on the DF potential to supplement that for NeHF and NeDF. This will undoubtedly account for some of the differences between our data and the other two studies.

In conclusion the modified Truhlar extrapolation produces values midway between the other two works, emulates a large basis set and clearly produces reasonable values for D_e and r_e. Indeed the modified Truhlar extrapolation may be a more reliable estimate, of the dissociation energy and equilibrium bond distances for both NeHF and NeFH. It is possible that some of the problems regarding induction forces identified earlier in ArHF are also present in NeHF. However, since Ne is less polarisable than Ar induction effects should be much smaller in NeHF. Indeed any unaccounted for induction effects must be minor due to the similarities of the calculated bond lengths and the energies between this work and the morphed study.

5.4.8 HeHF AND HeFH

As for NeHF and NeFH, reliable CBS limits are also unavailable for HeHF and HeFH. Table 5.13 therefore compares the modified Truhlar extrapolation with

three other works, a symmetry adapted perturbation theory (SAPT) study,[35] an experimental infrared gas phase study,[36] and another theoretical study using CCSD(T)/aug-cc-pVQZ by Y. Zhang, H. Y. Shi and W. Z. Wang.[37]

The SAPT method is different to the supermolecular approach applied in our study in that the potential surface, and hence dissociation energy, is obtained directly and not from a difference in the total energies of the complex and fragments. The interaction energies are obtained as a sum of well defined contributions from electrostatic, exchange, induction and dispersion forces. The SAPT study of Moszynski *et al.*[35] concluded that HeHF and HeFH are mainly bound by dispersion forces with small but non-negligible contributions from the other forces.

The modified Truhlar extrapolation yields quite different dissociation energies to the SAPT study. For HeHF, D_e is 17 % higher (6.79 cm^{-1}), while r_e is 0.14 Å lower. For HeFH the D_e is 27 % lower (9.77 cm^{-1}) and the r_e is 0.03 Å higher. The most noticeable feature of this comparison is that our calculations predict a large change in binding energy from HeHF to HeFH of 20 cm^{-1}, with the bond strength for HeHF being virtually double that of HeFH. In contrast SAPT predicts very little difference in D_e for the two isomers.

Generally speaking the SAPT method is expected to produce results of a similar quality to the CCSD(T) method for the same sized basis set.[38] This is where the major difference between the calculations lies. The SAPT study essentially uses a basis set of comparable to size to the aug-cc-pVTZ basis set (in its contracted form [5s3p2d]) for helium but much smaller ones with fewer polarisation and diffuse functions for hydrogen and fluorine.

Table 5.13 Van der Waals dissociation energies and equilibrium internuclear separations of HeHF and HeFH.

Molecule	Basis Set / Method[a]	D_e/cm^{-1}	r_e/Å[b]
HeHF	aug-cc-pVDZ c.p.	31.66	2.44
	aug-cc-pVTZ c.p.	39.11	2.32
	Extrap aug c.p.	46.47	2.25
	Experimental [c]	39.20	2.39
	SAPT calc [d]	39.68	2.39
	aug-cc-pVQZ[e]	46.614	2.28
HeFH	aug-cc-pVDZ c.p.	13.83	3.36
	aug-cc-pVTZ c.p.	21.22	3.01
	Extrap aug c.p.	26.36	2.94
	Experimental[c]	35.12	2.95
	SAPT calc [d]	36.13	2.91
	aug-cc-pVQZ[e]	25.026	2.97

(a) See footnote to table 5.8 for description of various methods.

(b) r_e = Ne-H bond distance in NeHF and, Ne-F bond distance in NeFH. H-F distance was fixed at 0.918 Å in this work.

(c) Data from ref. (36).

(d) Data from ref. (35). r(HF) fixed at 0.917 Å

(e) Data from ref. (37).

The contracted [5s3p2d1f] basis set was employed for fluorine, which is actually much smaller than a cc-pVDZ basis set, although it does contain high order polarization functions. The contracted [3s2p1d] basis set was used for hydrogen, which is comparable in size to a cc-pVDZ basis set, although again it contains higher order polarization functions. This use of 'unbalanced' basis sets in the SAPT study probably accounts for much of the difference between the SAPT parameters and those calculated in the present work.

Lovejoy and Nesbitt[36] have carried out a gas phase infrared spectroscopic study of HeHF in a supersonic jet expansion. They determined D_0 to be 7.1 ± 0.1 cm^{-1}. The experimental data were fitted to an empirical function that combines Hartree-Fock and dispersion terms. This Hartree-Fock plus damped dispersion (HFD) model used by Lovejoy and Nesbitt is described by Rodwell *et al.*[39] The values obtained for D_e of 39.20 cm^{-1} and r_e of 2.39 Å were obtained for HeHF. Clearly their r_e is the same as the SAPT study and the dissociation energies are also very similar. Thus the differences between the experimental IR study and the values generated by the modified Truhlar extrapolation are very similar to those already described for the SAPT study.

In a similar fashion the D_e derived from the experimental data for HeFH is also very similar to the SAPT study, as is the bond distance. However in the case of r_e, the modified Truhlar extrapolated value is even closer, only 0.01 Å less. It is worth noting that for all the various methods, a large increase in bond distance is calculated upon going from HeHF to HeFH but that only the modified Truhlar extrapolation predicts a corresponding decrease in the bond strength, as might have been expected.

During the preparation of this Chapter a new and directly relevant piece of work by Chinese workers was encountered in the literature.[37] The data is included in table 5.13 and the theoretical values were generated using CCSD(T) method and an aug-cc-pVQZ basis set. The potential energy surface of HeHF which includes the minima of both isomers was mapped out. From table 5.13 it is clear that for both HeHF and HeFH the dissociation energies and bond distances at the minima agree very closely with the modified Truhlar extrapolation.

In summary, the modified Truhlar extrapolation produces van der Waals dissociation energies and equilibrium bond distances quite different to either the SAPT or the experimental studies. Given the good performance of the modified Truhlar extrapolation in describing NeHF and NeFH, it seems likely that a similarly good performance, if not better, would be expected for HeHF and HeFH. This is confirmed by the recent publication of the work of Zhang *et al.* Consequently, we suspect our calculations may be far more reliable than the SAPT work by Moszynski. If this is true then the D_0 and D_e values for HeHF quoted by Lovejoy and Nesbitt are questionable and merit further experimental investigation.

5.5 CONCLUSIONS

The Truhlar basis set extrapolation has been applied to the study of van der Waals complexes for the first time. The original Truhlar extrapolation has been shown to perform very poorly in describing the van der Waals dissociation energies and bond lengths. However with two changes, addition of a set of standard diffuse functions coupled with employment of the counterpoise correction, the extrapolation procedure yields dissociation energies (D_e) within approximately 5 % of the estimated CBS limit and equilibrium bond distances (r_e) consistently

within 0.1 Å. In all cases the modified Truhlar extrapolation yields results closer to the CBS limit than either the aug-cc-pVDZ or aug-cc-pVTZ calculations used in the extrapolation procedure. The only case when the modified Truhlar extrapolation performed poorly was for ArHF, where D_e is 15 % larger than the CBS value. This discrepancy has been attributed to a poor description of induction forces.

The effect of changing the value of the empirical parameter β, which affects the correlation energy contribution in the extrapolation procedure, has been investigated. The conclusion is that a value of β between 2.0 and 2.2 for the van der Waals complexes investigated is optimum and is in agreement with the value of β=2.0 proposed by Fast and Truhlar *et al.* from their study of 29 chemically bound molecules. Consequently, we propose a modified Truhlar extrapolation which uses the empirical parameters of Fast and Truhlar *et al.* of α = 3.4 and β = 2.0, but with the addition of a single set of diffuse functions to both the cc-pVDZ and cc-pVTZ basis sets and a counterpoise correction to account for the basis set superposition error. These changes make the modified extrapolation scheme more computationally expensive than the original but still much cheaper than the large basis set calculations required for a meaningful description of van der Waals clusters.

A recent study by Dunning[40] investigating the CCSD(T) method showed, that the intrinsic error of the CCSD(T) method is ~1 % for chemically bound molecules and up to ~3 % for rare gas dimers, indicating that the CCSD(T) method at the CBS limit is a close approximation to reality. Thus the modified Truhlar extrapolation described in this chapter may have a wide range of applications. The modest computational requirements open up many possibilities,

including the investigation of van der Waals complexes containing one or more heavy atoms, the study of large complexes, and the extensive mapping of multidimensional potential energy surfaces. Further applications of the modified Truhlar extrapolation are described in later chapters, specifically chapters 6 and 7.

Finally, we note that Dunning has recently suggested[40] that doubly augmented basis sets are required for calculations on van der Waals clusters. Ironically, we have good agreement with CBS limits for singly augmented basis sets. It would be interesting to investigate the effect of using doubly augmented basis with the modified Truhlar extrapolation. However this would of course increase the computational cost and will go some way towards defeating the object of employing the Truhlar extrapolation.

5.6 REFERENCES

1. P. Hobza, and R. Zahradnik, *Chem. Rev.*, **88** (1988) 871.
2. G. Chalasinski, and M. Gutowski, *Chem. Rev.*, **88** (1988) 943.
3. A. D. Buckingham, P. W. Fowler, and J. M. Hutson, *Chem. Rev.* **88** (1988) 963.
4. G. Chalasinski and M. Szczesniak, *Chem. Rev.*, **94** (1994) 1723.
5. P. Hobza, H. L. Selze, and E. W. Schlag, *Chem. Rev.*, **94** (1994) 1767.
6. T. van Mourik, A. K. Wilson, and T. H. Dunning, *Mol. Phys.*, **96** (1999) 529.
7. H. Partridge and C. W. Bauschlicher, *Mol. Phys.*, **96** (1999) 705.
8. T. van Mourik and T. H. Dunning, *J. Chem. Phys.*, **107** (1997) 2451.
9. J. M. L. Martin, *Chem. Phys. Lett.*, **259** (1996) 669.
10. T. Helgaker, W. Klopper, H. Koch, and J. Noga, *J. Chem. Phys.*, **106** (1997) 9639.
11. A. Halkier, W. Klopper, T. Helgaker, P. Jørgensen, and P. R. Taylor, *J. Chem. Phys.*, **111** (1999) 9157.
12. D. E. Woon, *J. Chem. Phys.*, **100** (1994) 2838.
13. D. G. Truhlar, *Chem. Phys. Lett.*, **294** (1998) 45.
14. T. H. Dunning, *J. Chem. Phys.*, **90** (1989) 1007.
15. R. A. Kendall, T. H. Dunning, and R. J. Harrison, *J. Chem. Phys.*, **96** (1992) 6796.
16. D. E. Woon and T. H. Dunning, *J. Chem. Phys.*, **98** (1993) 1358.
17. P. L Fast, M. L. Sánchez, and D. G. Truhlar, *J. Chem. Phys.*, **111** (7) (1999) 2921.
18. A. Halkier, T. Helgaker, P. Jorgensen, W. Klopper, H. Koch, J. Olsen and A. K. Wilson, *Chem. Phys. Lett.*, **286** (1998) 243.

19. C. Schwartz, *Phys. Rev.*, **126** (1962) 1015.

20. D. P. Carroll, H. J. Silverstone, R. M. Metzger, *J. Chem. Phys.*, **71** (1979) 4142.

21. R. N. Hill, *J. Chem. Phys.*, **83** (1985) 1173.

22. J. M. L. Martin and P. R. Taylor, *J. Chem. Phys.*, **106** (1997) 8620.

23. Y.-Y. Chuang and D. G. Truhlar, *J. Phys. Chem. A,* **103** (6) (1999) 651.

24. A. Halkier, T. Helgaker, W. Klopper, P. Jorgensen and A. G. Csaszar, *Chem. Phys. Lett.*, **310** (1999) 385.

25. Gaussian 94/DFT, Revision B.2, M. J. Frisch, G. W. Trucks, H. B. Schlegel, P. M. W. Gill, B. G. Johnson, M.A. Robb, J. R. Cheeseman, T. Keith, G. A. Peterson, J. A. Montomery, K. Raghavachari, M. A. Al-Laham, V. G. Zakrzewski, J. V. Ortiz, J. B. Foresman, J. Cioslowski, B. B. Stefanov, A. Nanayakkara, M. Challacombe, C. Y. Peng, P. Y. Ayala, W. Chen, M. W. Wong, J. L. Andres, E. S. Replogle, R. Gomperts, R. L Martin, D. J. Fox, J. S. Binkley, D. J. Defrees, J. Baker, J.P. Stewart, M. Head-Gordon, C. Gonzalez and J. A. Pople, Gaussian, Inc., Pittsburgh PA (1995).

26. S. M. Cybulski, and R. R. Toczylowski, *J. Chem. Phys.*, **111** (1999) 10520.

27. J. U. Grabow, A. S. Pine, G. T. Fraser, F. J. Lovas, R. D. Suenram, T. Emilsson, E. Arunan and H. S. Gutowsky, *J. Chem. Phys.*, **102** (1994) 1181.

28. C. Chuang, K. J. Higgins, H. C. Fu and W. Klemperer, *J. Chem. Phys.* **112** (2000) 7022.

29. I. C. Hayes, G. J. B. Hurst, and A. J. Stone, *Mol. Phys.*, **53** (1984) 107.

30. P. W. Fowler and A. D. Buckingham, *Mol. Phys.*, **50** (1983) 1349.

31. H. Partridge, D. W. Schwenke and C. W. Bauschlicher, *J. Chem. Phys.*, **99** (12) (1993) 9776.

32. T. Kiljunen, J. Eloranta and H. Kunttu, *J. Chem. Phys.*, **110** (24) (1999) 11814.

33. S. V. O'Neil, D. J. Nesbitt, P. Rosmus, H.-J. Werner and D. C. Clary, *J. Chem. Phys.*, **91** (1989) 711.

34. M. Meuwly and J. M. Hutson, *J. Chem. Phys.*, **110** (17) (1999) 8338.

35. R. Moszynski, P. E. S. Wormer, B. Jeziorski and A. van der Avoird, *J. Chem. Phys.*, **101** (4) (1994) 2811.

36. C. M. Lovejoy and D. J. Nesbitt, *J. Chem. Phys.*, **93** (1990) 5387.

37. Y. Zhang, H. Y. Shi and W. Z. Wang, *Acta Physico-Chimica Sinica.* **17** (2001) 1013.

38. P. Jensen and P. R. Bunker (Ed's), Computational Molecular Spectroscopy, (2000) Wiley.

39. W. R. Rodwell, L. T. Sin Fai Lam and R. O. Watts, *Mol. Phys.*, **44** (1981) 225.

40. T. H. Dunning, *J. Phys. Chem. A,* **104** (2000) 9062.

CHAPTER 6

HRgF Molecules

6. HRgF MOLECULES

6.1 INTRODUCTION

Noble gases are particularly stable due to their filled orbitals. However, as early as 1933 Pauling[1] predicted that the heavy noble gases would form chemical bonds and in 1962 this prediction became a reality when Bartlett[2] prepared $XePtF_6$, the first noble gas compound. Since then a large number of noble gas compounds of xenon and krypton have been prepared.[3]

Recently, Pettersson, Lundell and Räsänen have developed and applied an elegant technique for producing a whole range of new rare gas molecules of the general form HRgY, where Rg = rare gas atom and Y = H, F, Cl, Br, I, CN, NC or SH.[4-6] The technique consists of selecting a suitable HY molecule, photodissociating and trapping it in rare gas matrix, followed by careful annealing of the matrix. The hydrogen atoms readily diffuse through the matrix on annealing and may approach a rare gas atom on the opposite side from a halogen atom, leading to the desired HRgY molecule. This method may be used to produce HRgY species in a matrix of the same rare gas or of another, dopant rare gas. The species produced have been observed in the matrix by infrared absorption or time-resolved luminescence spectroscopy and thus their vibrational frequencies may be determined.

HRgY molecules have only recently been subjected to *ab initio* calculations. In 1995, Pettersson, Lundell and Räsänen[4] observed the first hydrogen-rare gas atom bonds, when they reported infrared matrix isolation spectra of HXeCl, HXeBr, HXeI and HKrCl. The spectra were assigned with the assistance of vibrational frequencies determined from *ab initio* calculations. Calculations were also presented for some molecules not detected experimentally, namely, HXeF, HKrF, HArF and HArCl.

The calculations were performed with the MP2 method to account for electron correlation and effective core potentials (ECP) were employed for the rare gas and halogen atoms. The *ab initio* harmonic vibrational frequencies were found to be generally in line with the experimental frequencies, although they were usually overestimated. In particular, the predicted Rg-H stretching frequencies were found to be up to 500 cm^{-1} too high.

For all of the species studied the total energy calculated for the HRgY molecules was found to be higher than the sum of the total energies for the individual atoms (at infinite separation). In other words, these molecules are all unstable with respect to the separated atoms limit, but they remain bound because of an avoided crossing which creates a potential well (see later). The equilibrium geometry is linear and the binding is mainly ionic.

Shortly after the work described above, Pettersson, Lundell and Räsänen[5] presented infrared matrix isolation data on HXeH, HXeD and DXeD, accompanied by *ab initio* calculations at the MP2 level using the LANL1DZ (ECP) basis set. In general good agreement was obtained between predicted harmonic frequencies and these extracted from IR measurements. Again the total energy of the molecule at equilibrium is higher than that of the sum of the individual atoms in each case.

More recent work from the same group has focused on other new HXY species. HXeCN, HXeNC and HKrCN were detected in an infrared matrix isolation study using xenon and krypton matrices, and *ab initio* calculations at the MP2 level were provided to assist in assigning the spectra.[7] Additionally, the HKrNC isomer was investigated theoretically. Lundell *et al.*[8] have also published the results of a study on HXeI.

In 2000, Wong[9] published a purely theoretical paper concerned mainly with HHeF, but also HNeF, HArF and HKrF. Wong employed DFT calculations (B3LYP) as well CCSD with the correlation consistent basis set cc-pVTZ for all molecules. Additionally, HHeF was treated at the CCSD(T) level with the larger aug-cc-pVTZ and aug-cc-pVQZ basis sets. HHeF was found to be bound despite helium having the largest ionisation energy of any element. The Wong study marked a turning point in the theoretical investigation of HRgY molecules because of the use of correlation consistent basis sets along with CCSD(T), which offers a much improved description of electron correlation over DFT and MP2 methods. This results in the prediction of HArF and HKrF being of *lower* energy than the individual atoms - in contrast to the earlier calculations at lower levels of theory by Lundell *et al.* described above. Only HHeF is predicted to be less stable than the atoms. Another interesting feature of Wong's study is the prediction that HNeF is bound in DFT calculations but unbound at the CCSD level. The Wong study is discussed in more detail later.

Shortly after the Wong study, Lundell, Chaban and Gerber[10] published their results from a comprehensive *ab initio* investigation of HRgF species for all rare gases. Both MP2 and CCSD(T) methods were used with the 6-311++G(2d, 2p) basis set. Anharmonic vibrational frequencies were calculated from *ab initio* potential surfaces using the correlation consistent vibrational self consistent field (CC-VSCF) method. In line with Wong's study, all species except HHeF and HNeF are predicted to be more stable than the individual atoms. Also concurrent with Wong, HNeF is predicted to be bound at the MP2 level but not at CCSD(T).

Shortly after it was predicted to be observable by the aforementioned *ab initio* calculations, HArF was detected in the laboratory.[11] This is the first chemically bound molecule containing argon that has been observed experimentally.

The latest work on HRgF molecules was on HArF by Runeburg *et al.*[12] This theoretical study is the most sophisticated yet performed on HRgY molecules. The CCSD(T) method with a large basis set was employed to calculate the potential surface for the ground electronic state of HArF. This potential surface was then used to calculate harmonic vibrational frequencies and anharmonic corrections. In addition, the effect of the argon matrix on the vibrational frequencies of HArF was estimated from MP2 calculations on HArF in an octahedral cavity of 6 argon atoms. All the estimated harmonic frequencies were improved when compared with experiment when the anharmonic and matrix effect corrections were applied.

With the exception of the study on HArF by Runeburg *et al.* (which has appeared in the literature during the latter stages of the present work), all *ab initio* calculations to date have been carried out with relatively low levels of theory and/or small basis sets. In order to provide an improved description the modified Truhlar extrapolation has been applied to HHeF, HNeF and HArF in this work. Calculations on HArF will provide a rigorous test of the modified Truhlar extrapolation when applied to HRgF molecules by comparison with both the high quality *ab initio* calculations by Runeburg *et al.* and the experimental data of Khriachtchev *et al.* For HHeF and HNeF the modified Truhlar extrapolation should provide the most accurate *ab initio* study of the potential energy surfaces of these molecules to date. Dissociation energies, equilibrium bond distances and harmonic vibrational frequencies are calculated for all three molecules (except for HNeF, which is not bound). The harmonic vibrational frequencies were calculated using the

SURVIBTM[13] program from a potential surface of *ab initio* points generated by the modified Truhlar extrapolation.

6.1.1 Energetics of HRgF Molecules

Before the computational procedure is described, and the results discussed, a brief overview of the energetics of HRgF molecules is given.

Several of the *ab initio* studies described above have included calculations of *charge* distributions for HRgY molecules to gain an idea of the nature of the bonding.[4,5,7,8,10-12,14] HRgY molecules owe their stability to the dominance of $HRg^+ - F^-$ character in the bonding, *i.e.* there is a major ionic component. In contrast the covalent HRgY species destabilises the molecule generating an unbound potential surface. HRgF molecules are generally more stable than the individual atoms, and it is the interaction of the ionic and covalent species that is crucial in determining their stability. An avoided crossing is formed from the ionic and covalent potential curves, which creates an extra barrier to atomisation (see Figure 6.2). As shown in Figure 6.1, the global minimum for H, Rg and F is HF + Rg. The global minimum is reached from HRgF via the bending coordinate but this generally has a barrier much larger than the barrier to atomisation through bond stretching.

Previous work has indicated that HNeF and HHeF may be exceptions to the general picture presented above. In particular, previous *ab initio* calculations on HNeF have not shown conclusively whether this molecule is bound or unbound. Furthermore, there are still some uncertainties as to whether HNeF and HHeF have energies above or below their respective separated atom limits. These are two of the issues investigated in this chapter.

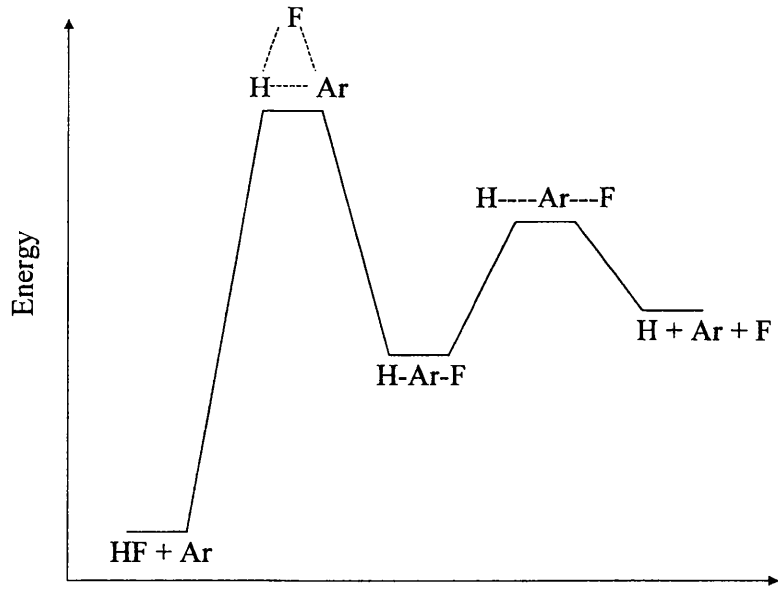

Figure 6.1. Diagram indicating the relative energies (not to scale) of the various chemical species arising from the H/Ar/F system. Dashed lines indicate bond formation/breaking during the transition between stable species.

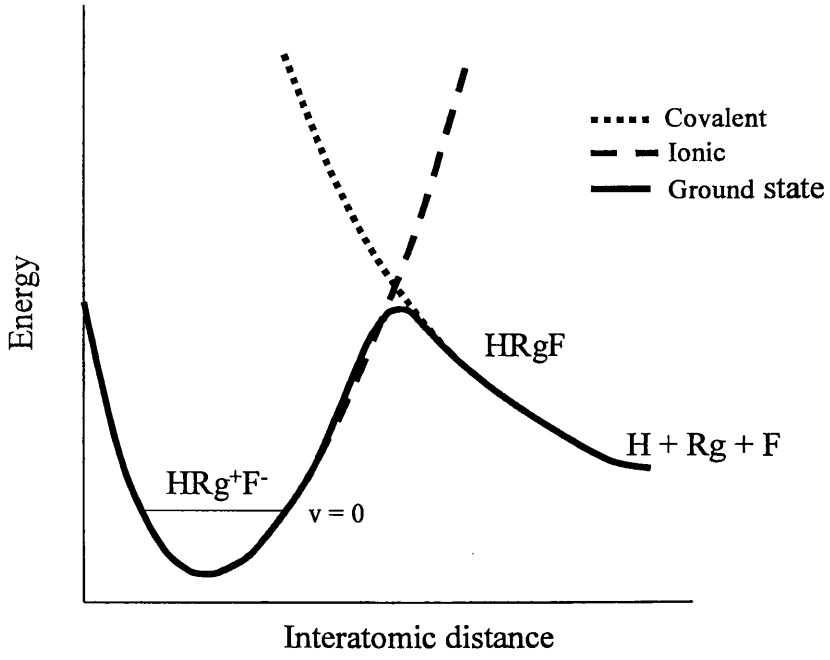

Figure 6.2. Diagram showing the avoided crossing on the ground state potential surface for HRgF molecules. The avoided crossing significantly stabilises the HRgF species.

6.2 COMPUTATIONAL METHODS

Calculations on the H-Rg-Y molecules are complicated by the ion-pair character, the interaction of neutral and ionic surfaces, and the relatively weak bonds that result. In addition, for xenon and krypton relativistic effects will become important and therefore ought to be taken into account. The weak bonding naturally leads to longer bonds and so basis sets with diffuse functions will be important. Weak binding energies also mean that small errors in the calculations will have more prominent effects than for strongly bound molecules. Consequently, a large proportion of the electron correlation must be accounted for.

6.2.1 Potential Energy Surfaces

The HRgF molecules have been investigated by employing the Truhlar extrapolation scheme as described in the previous chapter. The CCSD(T) method was used in combination with the aug-cc-pVDZ and aug-cc-pVTZ basis sets. As described in the previous chapter, all single point energies were corrected for the basis set superposition error by using the counterpoise procedure.

A 3D potential energy surface was generated for each molecule to allow any potential minima to be found, to calculate the dissociation energy, and as a starting point for vibrational frequency calculations. Vibrational frequencies were calculated using the program SURVIBTM[13], which is described later. As indicated earlier HRgF molecules are known to be linear and therefore the molecule was constrained to this geometry and a potential energy surface was determined from 50 single point calculations obtained by varying the H-Rg and Rg-F distances. Firstly, a crude potential surface of 25 points was created to determine where the approximate minimum energy configuration lay, by varying both the H-Rg and Rg-F bond

distances over a 0.4 Å range in 0.1 Å steps. A second potential surface of 25 points was then created around the approximate minimum determined by the previous potential surface by varying both the H-Rg and Rg-F bond distances over a 0.16 Å range in 0.04 Å steps. The potential surface was then interpolated using a bilinear interpolation procedure available in Microcal Origin (version 6) to add 1 extra point along each axis (H-Rg and Rg-F coordinates) between those calculated. This created a subsection of the potential surface made from the 400 points of a 20 x 20 point matrix, namely 25 *ab initio* calculated points and 375 points created from the bilinear interpolation. This allowed the minimum energy structure to be ascertained to within approximately 0.004 Å and the dissociation energy (D_e) to within approximately 5 cm^{-1} or less. The interpolation did not greatly affect the energy at the minimum, only lowering it by less than 1% when compared to the estimated minimum of the purely *ab initio* surface.

6.2.2 Vibrational Frequency Calculations

For HArF and HHeF the zero point energy and the vibrational frequencies were calculated using the program SURVIBTM.[13] In order to perform this analysis it was necessary to calculate a 4D potential surface by adding in the bending coordinate to the 3D potential surface used previously. Further *ab initio* calculations were carried out at a range of bond angles (θ) and bond lengths (of both H-Rg and Rg-F). The vibrational frequencies from SURVIBTM were obtained by using a 4D potential surface constructed from a matrix of 104 points. The 104 points were created from *ab initio* calculations of every combination of four bond angles and three bond lengths of both the HRg and RgF bonds making 36 points, plus an additional 16 points of every combination of the original four bond angles and two extra bond

distances for HRg and RgF. These 52 points were used twice by taking account of the symmetry of the molecule about the linear configuration, *i.e.* the potential surface is an even function in (θ - 180). The bond angles chosen were 140°, 160°, 165° and 170° (and by symmetry 220°, 200°, 195° and 190°).

In choosing an analytical function to fit the pointwise potential energy surface a compromise must be made between maximum function flexibility (high order polynomial) and the finite number of energy points. The quality of the fit was monitored by comparing the individual *ab initio* points to the points calculated by the fitted function (as calculated by SURVIBTM). The quality of the fit was also assessed by the root mean square (RMS) deviation.

A fifth order polynomial gave the smallest overall RMS deviation (usually 0.0001 Hartrees (~20 cm^{-1}) or less) and none or very few fitted points with a large deviation (>0.001 Hartrees (~200 cm^{-1})) from the respective *ab initio* point. The minimum RMS deviation was found when a broad selection of bond angles was used. *Ab initio* calculations at a HRgF angle of 180° were not used as this would induce errors into the SURVIBTM calculation due to slight inconsistencies created by Gaussian. Specifically, Gaussian makes use of symmetry where possible to reduce the number of integrals evaluated in the *ab initio* calculations. This introduces small rounding errors and produces a small but not insignificant discontinuity between the total energy at the linear geometry and that obtained at a very slight deviation from linearity (lower symmetry).

Harmonic vibrational frequencies were calculated by SURVIBTM using a conventional normal mode analysis as described in Chapter 4.

6.3 RESULTS AND DISCUSSION

Dissociation energies, interatomic equilibrium bond distances and vibrational frequencies have been calculated for HHeF and HArF. A comparison will be made with the best available calculations by other workers and, in the case of HArF, a comparison will also be made with matrix isolated infrared spectra.

HNeF does not form a minimum on its potential surface. The calculated potential surface is presented and the reason for the absence of a minimum is discussed toward the end of this chapter.

6.3.1 HHeF

6.3.1.1 Structural Calculations and Energetics

Table 6.1 shows the structural data calculated for HHeF and is compared to the best previous calculations available in the literature[9,10]. A 3D representation of the potential surface and a contour plot are shown in figures 6.3 and 6.4, respectively. The equilibrium internuclear distances calculated in this work are comparable to those of Lundell *et al.* and Wong, clearly indicating that the same potential minimum has been located in all cases.

In all cases the dissociation energy is negative, indicating that the total energy of the atoms at infinite separation is lower than that of the molecule. In other words, the molecule is unstable with respect to dissociation to individual atoms. Despite this, HHeF is predicted to be observable because of an avoided crossing which creates a barrier to dissociation, as discussed in more detail later.

Table 6.1. Structural data for HHeF

HHeF	DZ[a]	TZ[a]	Extrap.[b]	Lundell *et al.*[c]	Wong[d]
D_e / cm^{-1}	-8143.6	-6435.6	-5344.3	-3347.2	-5650.9
R_e (H-He) / Å	0.83	0.81	0.804	0.825	0.811
R_e (He-F) / Å	1.43	1.41	1.413	1.422	1.416

(a) CCSD(T) calculations from this work with aug-cc-pVDZ or aug-cc-pVTZ basis sets, counterpoise corrected.

(b) Modified Truhlar extrapolation, counterpoise corrected.

(c) CCSD(T) calculations with 6-311++G(2d,2p) basis set from ref. 10.

(d) D_e calculated using CCSD(T) with aug-cc-pVQZ basis set, based on aug-cc-pVTZ optimised geometry from ref 9.

The dissociation energy calculated by Wong is larger than that calculated in the present work by ~300 cm^{-1}, which amounts to approximately a 5 % difference. The aug-cc-pV*X*Z series of basis sets are expected to systematically approach the CBS limit, and this can clearly be seen from the trend in dissociation energies from the aug-cc-pVDZ, aug-cc-pVTZ and aug-cc-pVQZ basis sets (the last is from Wong's calculations). The Truhlar extrapolation continues this trend, producing a D_e of lower energy than the aug-cc-pVQZ basis set and ought therefore to be closer to the CBS limit. However, there is need for some caution in this comparison since our dissociation energy is counterpoise corrected whereas that by Wong is not. However, Wong has examined the effect of the BSSE and estimated it to be no more than 40 cm^{-1} for the aug-cc-pVQZ basis set. This is clearly a modest effect and does not invalidate the overall conclusion, namely there is a systematic trend in D_e values for the aug-cc-pV*X*Z basis sets and the extrapolated value from the present work should be closest to the CBS limit.

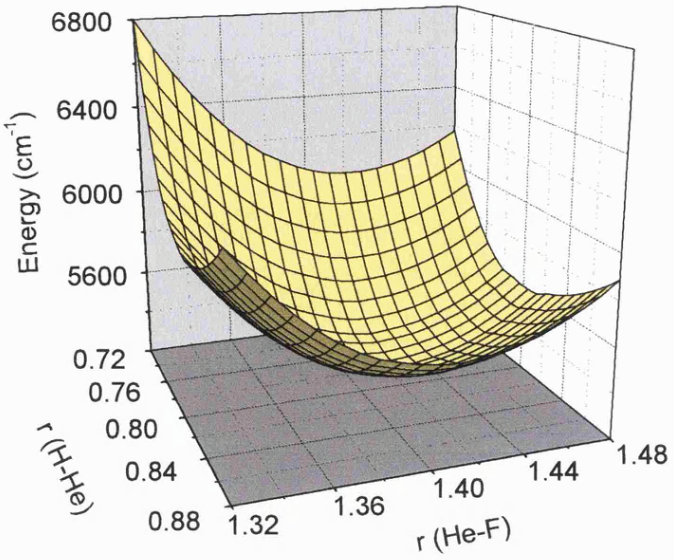

Figure 6.3. View of the HHeF potential energy surface. This focuses on the region around the minimum only. Internuclear distances are in Å. The surface was created from 25 *ab initio* points and 375 points generated by a bi-linear interpolation. See text for further details.

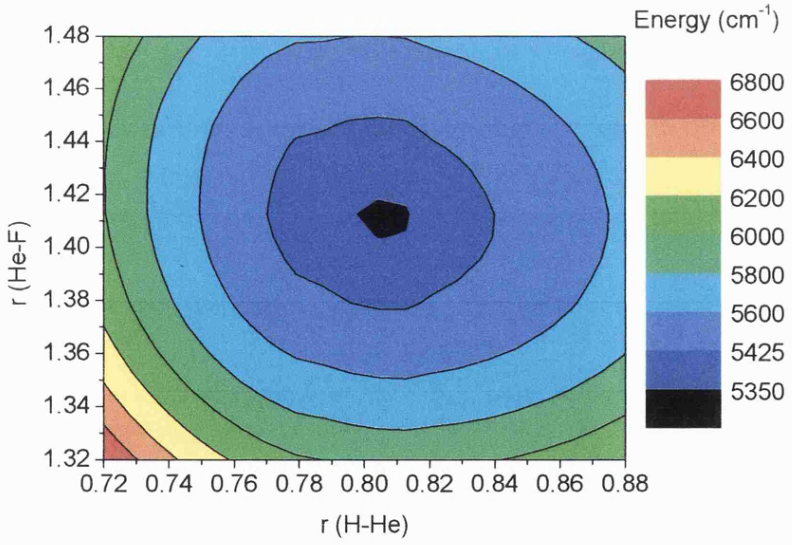

Figure 6.4. Contour plot of the HHeF potential surface shown in figure 6.3. Internuclear distances are in Å.

Interestingly, the modified Truhlar extrapolation produces an atomisation energy that is very different to that calculated by Lundell *et al.* The difference, 1997 cm^{-1}, or some 59%, is most likely due to the difference in the basis sets used. Both the 6-311++G(2d, 2p) used by Lundell *et al.* and the aug-cc-pVTZ basis set used in the modified Truhlar extrapolation are triple zeta basis sets with additional polarization and diffuse functions. However the 6-311++G(2d, 2p) basis set contains fewer functions than the aug-cc-pVTZ basis set, 11 compared to 14 contracted functions respectively. The aug-cc-pVTZ basis set contains more polarization functions, including functions of higher order. In addition to this the modified Truhlar extrapolation imitates a much larger basis set than either the triple zeta basis set used in this work or by Lundell *et al.*, and is therefore expected to produce a dissociation energy closer to the complete basis set limit than either would individually. Secondly, the correlation consistent basis sets are correlation consistent in the sense that each basis set contains all functions that lower the energy by at least a set amount and consequently are more suited for use in correlation calculations[15,16] than are the split valence basis sets.[17] Another important difference is that the dissociation energy calculated by Lundell *et al.* has not been corrected for basis set superposition error. However the effect of the basis set superposition error, in this case (as noted above), is expected to be much smaller than the difference between the calculated energies and will usually tend to lower the dissociation energy. BSSE is therefore unlikely to account for the difference in the dissociation energies.

In conclusion the D_e calculated by Lundell and co-workers is seriously in error due to a deficient basis set, and our value of D_e calculated using the modified Truhlar extrapolation represents the current best estimate.

6.3.1.2 Harmonic Vibrational Frequency Calculations

The harmonic vibrational frequencies for HHeF are shown in Table 6.2 along with values calculated previously by Lundell *et al.* and Wong. The frequencies are similar but not identical, the differences being under 7 % for the bend and the He-F stretch. However, for the He-H stretch the difference is still approximately 7 % compared to the Wong study, but our value is 355 cm^{-1} larger, or some 17 % more, than that obtained by Lundell *et al.*

The differences in the calculated frequencies and zero point energies are likely to be linked to the differences in the dissociation energies discussed earlier. As described above, Lundell *et al.* and ourselves have used rather different basis sets. The D_e from this work was much larger than Lundell *et al.* and will probably account for the larger stretching frequencies that we obtained. It is worth noting that Wong used a different method (CCSD) and a different (smaller) basis set for calculating the harmonic frequencies than was used for the dissociation energy.

In conclusion, harmonic vibrational frequencies have been calculated for HHeF using a potential energy surface derived from the modified Truhlar extrapolation. This should provide a higher quality potential surface than previous work and therefore the vibrational frequencies calculated here are currently the best available.

Table 6.2. Harmonic vibrational frequencies calculated for HHeF

HHeF	HHeF bend / cm^{-1}	He-F stretch / cm^{-1}	He-H stretch / cm^{-1}
DZ[a]	778	963	2037
TZ[a]	762	980	2354
Extrap[b]	756	983	2465
Lundell *et al.*[c]	777	964	2110
Wong[d]	809	1037	2304

(a) Calculations performed using CCSD(T) method with aug-cc-pVDZ or aug-cc-pVTZ basis sets (counterpoise corrected).

(b) Modified Truhlar extrapolation (counterpoise corrected).

(c) CCSD(T) calculations with 6-311++G(2d, 2p) basis set, from ref. 10.

(d) CCSD calculations with cc-pVTZ basis set, from ref. 9.

(e) This value is quoted by Lundell *et al.* but is clearly erroneous.

6.3.2 HArF

6.3.2.1 Structural Calculations and Energetics

Structural parameters for HArF are shown in table 6.3, along with results from earlier *ab initio* studies on this molecule, one by Lundell *et al.*[10] and the other by Runeburg *et al.*[12] Lundell *et al.* used the CCSD(T) method with a 6-311++G(2d, 2p) basis set, whereas Runeburg *et al.* used CCSD(T) with an aug-cc-pV5Z basis set. Runeburg *et al.* employed the counterpoise correction whereas Lundell *et al.* did not. The *ab initio* potential energy surfaces after bi-linear interpolation are shown in figures 6.5 and 6.6. It is worth noting that unlike HHeF, the energy for dissociating to atomic

fragments for HArF is positive, showing that HArF is more stable than the individual atoms at infinite separation.

Table 6.3. Structural data for HArF

HArF	DZ[a]	TZ[a]	Extrap.[b]	Lundell *et al.*[c]	Runeburg *et al.*[d]
D_e / cm^{-1}	-1802.1	1137.3	2802.5	4113.4	2984.2
R_e (H-Ar) / Å	1.39	1.35	1.338	1.3550	1.3288
R_e (Ar-F) / Å	2.03	2.0	1.979	2.0048	1.9690

[a] CCSD(T) calculations with aug-cc-pVDZ or aug-cc-pVTZ basis set (counterpoise corrected).

[b] Modified Truhlar extrapolation (counterpoise corrected).

[c] CCSD(T) calculations with 6-311++G(2d, 2p) basis set, from ref. 10.

[d] CCSD(T) calculations with aug-cc-pV5Z basis set, counterpoise corrected, from ref. 12.

As for HHeF, Lundell *et al.* obtain a very different D_e for HArF compared with our work. In the case of HArF, Runeburg *et al.* have also published calculations using the much larger aug-cc-pV5Z basis set. The results of Runeburg *et al.* should produce values close to the CBS limit. When the Truhlar extrapolation values from the present work are compared to the aug-cc-pV5Z values the equilibrium bond distances are similar: R_e (H-Ar) is 0.009 Å larger and R_e (Ar-F) is 0.010 Å larger for the modified Truhlar extrapolation. The dissociation energies are also in quite close agreement, the modified Truhlar extrapolation being 6.1% (181.7 cm^{-1}) smaller. Our findings, taken together with those of Runeburg *et al.*, indicate that the true D_e for HArF is $\leq$ 3000 cm^{-1}.

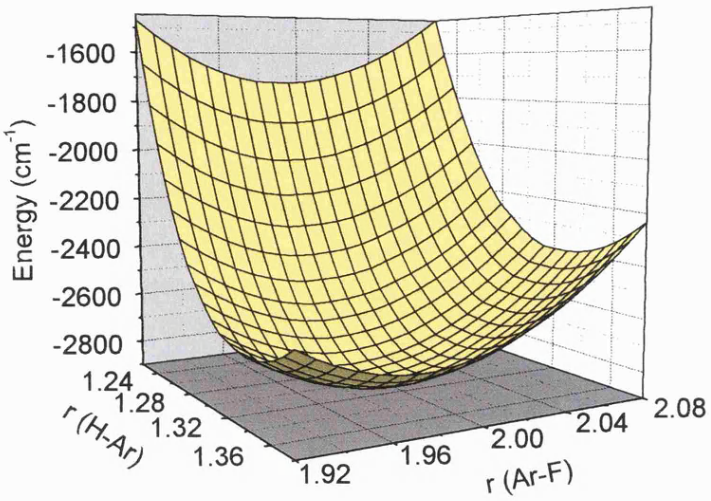

Figure 6.5. View of the HArF potential energy surface. This focuses on the region around the minimum only. Distances are in Å. The surface was created from 25 *ab initio* points and 375 additional points generated by a bi-linear interpolation. See text for further details.

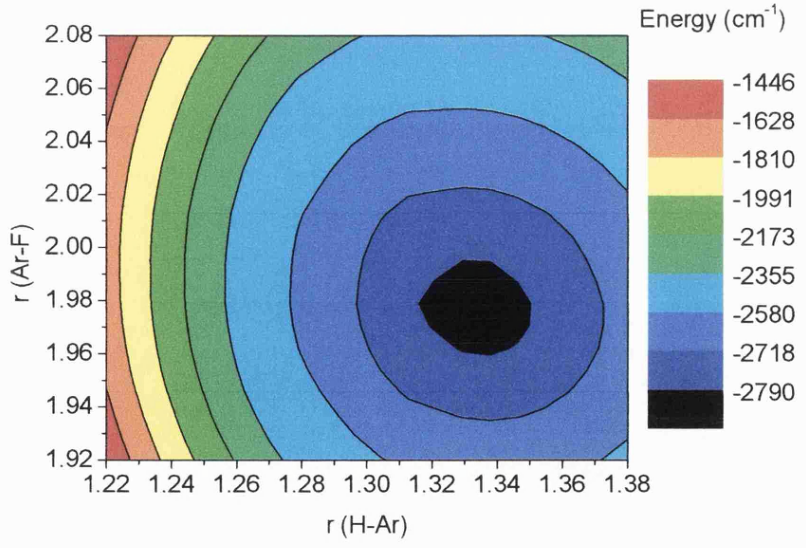

Figure 6.6. Contour plot of the HArF potential surface shown in figure 6.5. Distances are in Å.

6.3.2.2 *Vibrational Frequency Calculations*

Table 6.4 compares harmonic vibrational frequencies calculated with the modified Truhlar extrapolation with the two earlier *ab initio* studies. In addition, a matrix isolation investigation of HArF has been carried out by Khriachtchev *et al.*[11] and the vibrational fundamental frequencies obtained are also included in table 6.4.

Table 6.4. Vibrational frequencies for HArF

HArF	Ar-F stretch $(cm)^{-1}$	H-Ar-F bend $(cm)^{-1}$	H-Ar stretch $(cm)^{-1}$
DZ[a]	455	673	1760
TZ[a]	540	737	1842
Extrap.[b]	546	757	1946
Lundell[c]	479	781	1793
Runeburg[d]	480 (463)	729 (686)	2097 (1925)
Experimental[e]	435.7	687.0	1969.5

(a) CCSD(T) calculations with aug-cc-pVDZ or aug-cc-pVTZ basis sets (counterpoise corrected).

(b) Modified Truhlar extrapolation (counterpoise corrected).

(c) CCSD(T) calculation using 6-311++G(2d, 2p) basis set, not counterpoise corrected, from ref. 18.

(d) CCSD(T) calculation from ref. 12 using aug-cc-pVQZ basis set (not counterpoise corrected). Values in parenthesis have been corrected for anharmonic and matrix effects.

(e) Experimental IR data from ref. 11.

The discrepancy between the harmonic vibrational frequencies of HArF calculated in this work and those of Lundell and co-workers is similar to that found for HHeF

frequencies. The explanation is similar to that already discussed earlier for HHeF and so need not be considered further.

In judging the reliability of our calculated vibrational frequencies, the most useful comparison is with the work of Runeburg *et al.* Runeburg *et al.* obtained harmonic frequencies higher than the experimental fundamental frequencies, as would be expected given the neglect of anharmonicity. In the Truhlar extrapolation work of this thesis the Ar-F stretch and the bending mode also yield harmonic frequencies higher than the experimental fundamentals, but this is not the case for the Ar-H stretch.

There is a considerable discrepancy between our harmonic frequencies and those of Runeburg *et al.*, which is in contrast to the structural and energetics calculations. The reasons for this are not immediately clear, but one factor to bear in mind is that Runeburg *et al.* used a smaller (aug-cc-pVQZ) basis set when calculating vibrational frequencies, than the aug-cc-pV5Z basis set used to calculate the dissociation energy. Thus their vibrational frequencies should be <u>further</u> from the CBS limit than their structural and energetics calculations.

Energies calculated with aug-cc-pV*X*Z series of basis sets gradually approach the CBS limit, which allows extrapolation with some confidence towards the CBS limit. Since vibrational frequencies are derived from derivatives of the potential energy, extrapolation of vibrational frequencies as a function of basis set should also be smooth. If correct, the aug-cc-pVQZ harmonic frequencies of Runeburg *et al.* should therefore continue the trend of increasing frequencies that is evident for the aug-cc-pVDZ and aug-cc-pVTZ basis sets. From table 6.4 this is clearly not the case, at least not for the Ar-F stretch and the bending mode. There are two possible reasons for this. One possibility is that omission of a counterpoise correction by

Runeburg *et al.* has affected their calculated frequencies. However this would generally be expected to lead to overestimates of stretching frequencies and therefore probably cannot account for all of the discrepancies. Secondly, different methods were used by Runeburg *et al.* and ourselves to calculate the harmonic vibrational frequencies. Runeburg *et al.* have used a technique employing numerical second differentiation whereas SURVIBTM uses numerical differentiation of an analytical gradient. These two methods are known to lead harmonic frequencies that can differ by a few percent[19].

Our calculated vibrational frequencies are roughly in line with the experimental matrix isolated frequencies of Khriachtchev *et al.*, although there are discrepancies. Compared to the experimental values the H-Ar stretch is 0.8 % too low and the bend is overestimated by 10 %. Worst agreement is obtained for the Ar-F stretch which is 110.3 cm^{-1}, or some 25 %, higher than the experimental value. The discrepancies will doubtless be due to the relatively weak bonding and effects of the matrix environment.

In addition to calculating harmonic frequencies, Runeburg *et al.* also calculated anharmonic corrections and estimated the effect of the matrix on the vibrational frequencies. The matrix effect was taken in to account by assuming that it is dominated by nearest neighbour interactions. The vibrations of HArF in an octahedral cavity with six nearest neighbour octahedrally coordinated argon atoms were therefore considered. The matrix shifts were estimated to be -9, -7 and +38 cm^{-1} for the Ar-F stretch, bend and H-Ar stretch, respectively. The values in parenthesis in table 6.4 show matrix corrected vibrational fundamental frequencies obtained by Runeburg *et al.* As expected these frequencies are clearly much closer to the experimental values than our matrix-uncorrected harmonic frequencies.

6.3.3 HNeF

HNeF is different to both HHeF and HArF in that calculations using the modified Truhlar extrapolation indicate that there is no bound minimum for this molecule. Figures 6.7 and 6.8 show the potential surface in the region where a linear structure would lie if it existed. Only an inflection in the potential surface is observed in the H-Ne direction. Along the Ne-F coordinate, the surface contains a minimum at approximately 2.0 Å for small H-Ne values (0.8-1.0 Å); at longer H-Ne distances the potential is repulsive in the Ne-F coordinate. The apparent small ripples near the centre of the potential surface are an artefact of the interpolation procedure used to generate the potential surface and contour plots.

The shape of the potential surface suggests that a minimum in both H-Ne and Ne-F might have formed had the energetics been slightly different. In calculations performed by Lundell *et al.*[10] at the MP2 level (using a 6-311++G(2d,2p) basis set) a minimum was found, but calculations by the same research team using the CCSD(T) method and the same basis set yielded no minimum. This is the same result that Wong[9] discovered when comparing B3-LYP and CCSD calculations. Clearly the present work supports the view that HNeF is unbound. Perturbation theory recovers a large proportion of the dynamic electron correlation but is poor for describing static electron correlation. This leads to problems for molecules with near degenerate states like HNeF (in HNeF the two states concerned are the lowest ionic and covalent states). MP2 produces a minimum for HNeF as only the ionic surface is considered.

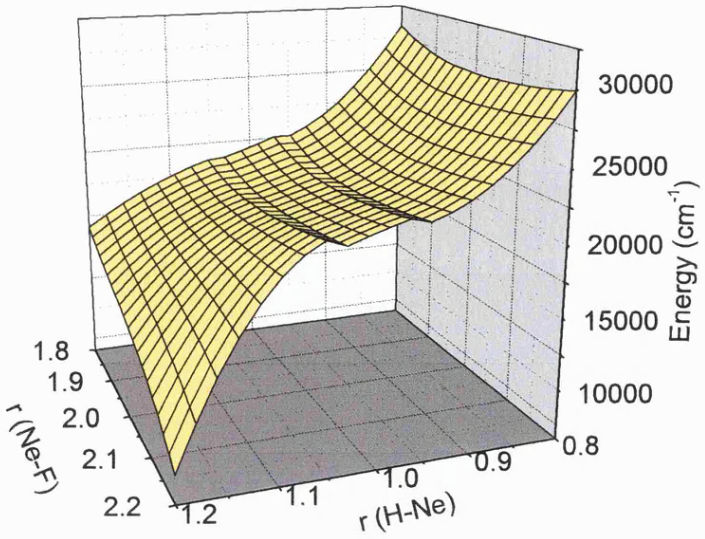

Figure 6.7. HNeF potential energy surface. The surface has been created from 25 *ab initio* points and 375 points generated by a bi-linear interpolation. Distances are in Å. The ripples in the centre were shown to be an artefact of the interpolation procedure; when additional *ab initio* data were used these ripples disappeared.

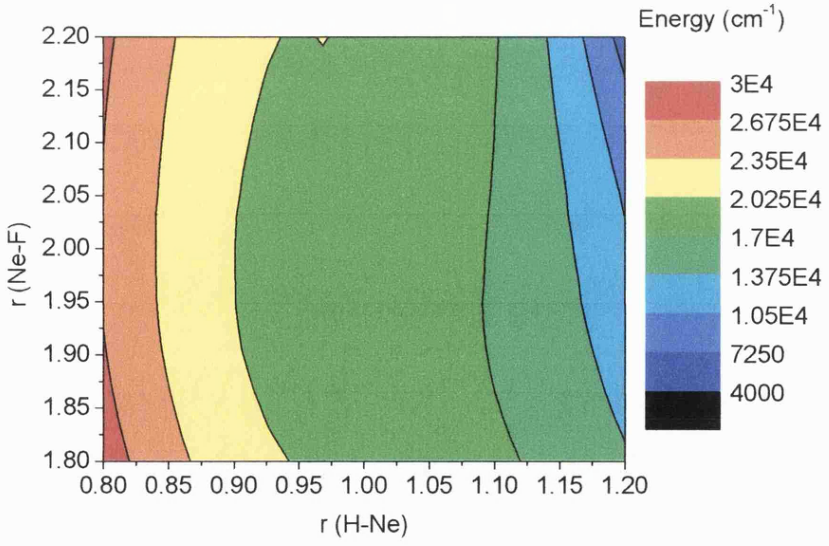

Figure 6.8. Contour plot of the HHeF potential surface shown in figure 6.1. Distances are in Å.

Interestingly the potential surface of HNeF around the avoided crossing demonstrates a much larger interaction energy (with respect to the atomisation limit) than either HHeF or HArF. The HNeF interaction energy is approximately -18500 cm^{-1}, much higher than the respective dissociation energies of -5338 cm^{-1} and 2803 cm^{-1} for HHeF and HArF. This clearly indicates that the interaction on the ionic potential surface is much stronger for HNeF compared with either HHeF or HArF. However, note that the total energy of the individual atoms lies lower than the energy of the HNeF cluster. This result is roughly in line with the dissociation energy found for bound HNeF, -20228 cm^{-1} at MP2 by Lundell *et al.* and -14288 cm^{-1} at B3-LYP by Wong.

As mentioned in the introduction the ionic bonding in all three HRgF species studied is different. In HArF interaction is dominated by the Ar^+ - F^- interaction. Helium is much less polarisable than argon and so the ionic interaction is dominated by H^+ - F^- interaction without any involvement of helium. Neon also possesses a low polarisability, but it has a larger diameter than helium and therefore the increased separation between H^+ and F^- weakens the ionic attraction. Consequently there is insufficient ionic interaction to stabilise HNeF, which results in the cluster being unbound.

The covalent curve crosses the ionic curve very close to the minimum of the ionic curve, thereby creating an avoided crossing with no minimum on the adiabatic ground state potential surface. However it is interesting to be able to map out the avoided crossing as an inflection in the potential surface (see Figures 6.7 and 6.8). The slope of the potential changes twice, indicating three distinct areas: short H-Ne distances (< ~0.9 Å) where the ionic potential dominates and the potential is mainly represented by the steep repulsive wall of the ionic curve as it approaches the bottom

of the ionic potential curve; medium H-Ne distances (~0.9 Å - ~1.1 Å) where the avoided crossing itself takes place as the potential surface changes to being mainly dominated by the covalent repulsive curve and is at its flattest; and thirdly long H-Ne distances (> ~1.1 Å) where the repulsive covalent curve dominates and the potential surface becomes steeper again.

6.4 GENERAL DISCUSSION

The bonding in HRgF is a combination of three possible representations, covalent H-Rg-F and the ionic representations HRg^{+}-F^{-} and HRg^{-}-F^{+}. Lundell *et al.*[10] have suggested that in general these three structures contribute approximately in the ratio 20/60/20, respectively. In other words the binding is mainly ionic with some element of covalent character. The approximate ratios of the contributions of the three representations were determined by an analysis of the electron density via electron localisation functions (ELF).[20]

There are two likely routes for dissociation, via the bending coordinate leading to the fragments HF + Rg, and a channel leading to neutral atoms H + Rg + F. An avoided crossing between the ionic ($HRg^{+}F^{-}$) and covalent (HRgF) potential curves occurs that creates a barrier to dissociation via atomisation.

The potential energy surface of HArF has been extensively studied by Runeburg *et al.*[12] and Wong.[9] Wong found that a barrier to dissociation along the bending coordinate for HArF of approximately 9797.2 cm^{-1} leading to the global minimum products Ar + HF. When this is compared to the barrier to dissociation via atomisation calculated by Runeburg *et al.* (2258 cm^{-1}) it is clear that the minimum energy path is to atomisation. For HeHF, dissociation by the bending coordinate will be of more importance, as the barrier (calculated by Wong[9]) is considerably lower

than for HArF and will compete with bond stretching for the lowest energy pathway. In view of the above findings our calculations have concentrated on the energy of atomisation as this will certainly be the preferred dissociation pathway for HArF and HNeF, and may also be a significant pathway for HHeF even if it is not the lowest energy pathway.

The data presented in this work for HArF produces bond distances and dissociation energies close to the calculations carried out by Runeburg *et al.* with their large aug-cc-pV5Z basis set and would suggest that the modified Truhlar extrapolation succeeds with HRgY. This leads to the conclusion that for HHeF, the data presented in this work is closer to the CBS limit than in any previous work. Similarly, our calculation of the ground state potential surface of HNeF should currently be the best available, and confirms that HNeF is unbound.

Figures 6.9-6.11 show diagrammatical representations of dissociation via atomisation of the HRgF clusters. Figure 6.9 for HArF is based on data from both this work and a similar diagram produced by Runeburg *et al.* Figures 6.10 and 6.11 are based solely on the results of the present work. The diagrams show the avoided crossing between the ionic and covalent curves, and illustrate the change from HArF, where the total energy of the atomic fragments lies above the energy of the HArF cluster, through HNeF where there is no minimum, to HHeF where the combined energy of the atoms lies below that of the HHeF cluster.

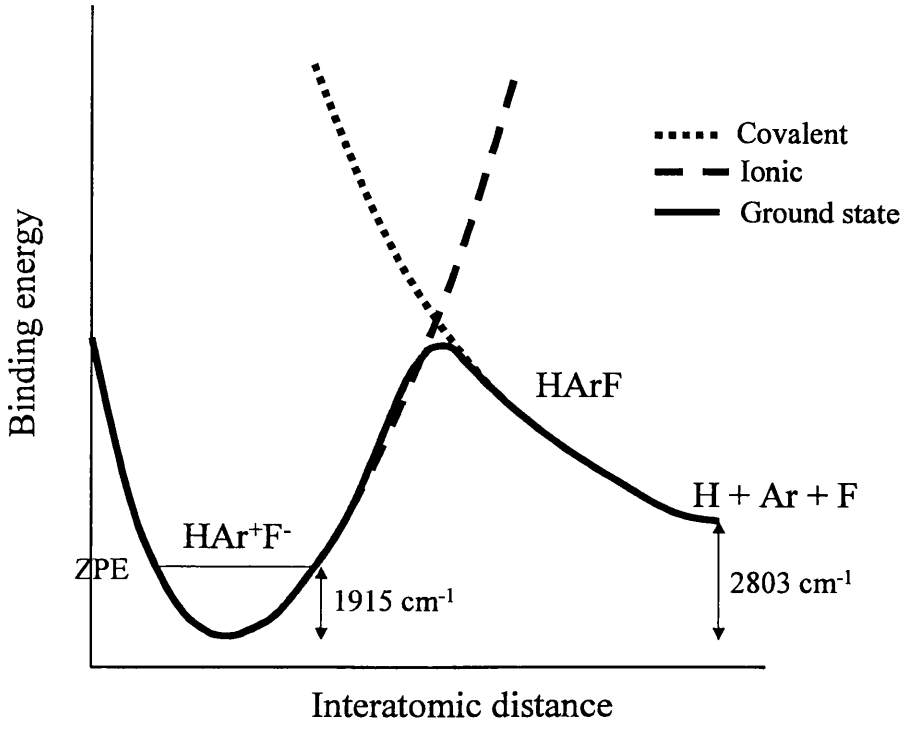

Figure 6.9. Diagrammatic potential energy curve for HArF atomisation. The energy of the atomic fragments lies above the zero point energy (ZPE) of HArF.

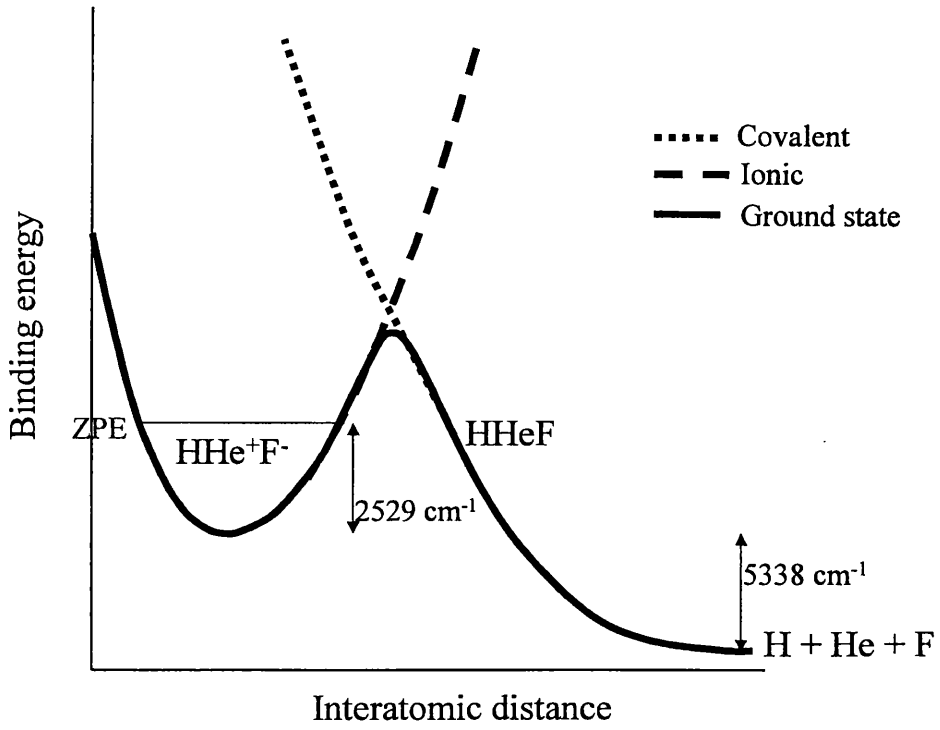

Figure 6.10. Diagrammatic potential energy curve for HHeF atomisation. The energy of the atomic fragments lies below the energy of the HHeF cluster.

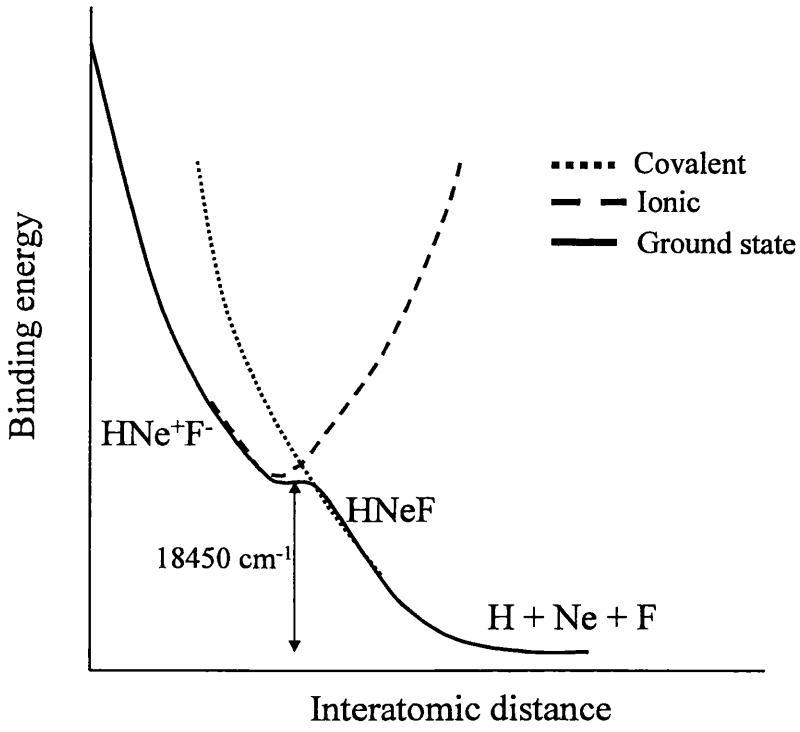

Figure 6.11. Diagrammatic potential energy curve for HNeF atomisation. The covalent curve is shown crossing the ionic curve close to the minimum of the ionic curve, thus producing a purely repulsive surface. The exact position of the avoided crossing is unknown.

6.5 SUMMARY

The modified Truhlar extrapolation has been applied to the unusual, chemically bound rare gas containing molecules HArF, HNeF and HHeF. The calculated dissociation energy and bond distances for HArF compare well with CCSD(T) calculations by Runeburg *et al.* using a relatively large basis set (aug-cc-pV5Z).

The calculations on HHeF and HNeF are the most sophisticated yet performed. For HNeF the potential surface has been investigated around the avoided crossing of the ionic and covalent curves and clearly shows no minimum for linear HNeF. For HHeF the calculated bond distances, dissociation energies and harmonic frequencies are all expected to be fairly close to the CBS limit. As a consequence of these findings the dissociation energies and harmonic vibrational frequencies for HHeF and HNeF calculated by Lundell *et al.*[10] have been shown to be erroneous.

The satisfactory findings for these molecules, which are far more strongly bound than the van der Waals clusters used to test the modified Truhlar extrapolation in Chapter 5, provides evidence that the modified Truhlar extrapolation is potentially applicable to a wide range of molecules and clusters. It should be useful for calculating potential energy surfaces, dissociation energies, and vibrational frequencies.

As the strength of the bonding in molecules increases it may be expected that extrapolation will be less beneficial as smaller basis sets will often produce acceptable results. However, the data in this chapter have clearly shown that for the HRgF molecules, extrapolation offers considerable improvements over the aug-cc-pVTZ basis set at marginal extra cost.

6.6 REFERENCES

1. L. Pauling, *J. Am. Chem. Soc.*, **55** (1933) 1895.
2. N. Bartlett, *Proc. Chem. Soc.*, (1962) 218.
3. J. H. Holloway and E. G. Hope, *Advan. Inorg. Chem.*, **46** (1999) 51.
4. M. Pettersson, J. Lundell and M. Räsänen, *J. Chem. Phys.*, **102** (1995) 6423.
5. M. Pettersson, J. Lundell and M. Räsänen, *J. Chem. Phys.*, **103** (1995) 205.
7. M. Pettersson, J. Lundell, L. Khriachtchev and M. Räsänen, *J. Chem. Phys.*, **109** (1998) 618.
6. M. Pettersson, J. Lundell and M. Räsänen, *Eur. J. Inorg. Chem.*, (1999) 729.
8. M. Pettersson, J. Lundell, L. Khriachtchev, M. Räsänen, G. M. Chaban and R. B. Gerber, *Chem. Phys. Lett.*, **322** (2000) 389.
9. M.W. Wong, *J. Am. Chem. Soc.*, **122** (2000) 6289.
10. J. Lundell, G.M. Chaban and R.B. Gerber, *Chem. Phys. Lett.*, **331** (2000) 308.
11. L. Khriachtchev, M. Pettersson, N. Runeburg, J. Lundell and M. Räsänen, *Nature*, **406** (2000) 874.
12. N. Runeburg, M. Pettersson, L. Khriachtchev and J. Lundell, *J. Chem. Phys.*, **114** (2001) 836.
13. W. C. Ermler, H. C. Hsieh and L. B. Harding, *Comp. Phys. Comm.*, **51** (1988) 257.
14. S. Berski, Z. Latajka, B. Silvi and J. Lundell., *J. Chem. Phys.*, **114** (2001) 4349.
15. D. E. Woon and T. H. Dunning, *J. Chem. Phys.*, **98** (1993) 1358.
16. P. Jenson and P. R. Bunker (eds.), *Computational Molecular Spectroscopy*, Wiley, (2000) 15.
17. K. Krishnan, J. S. Binkley, R. Seegar and J. A. Pople, *J. Chem. Phys.*, **72 (1)** (1980) 650.
18. A. VeldKamp, G. Frenking, *Chem. Phys. Lett.*, **226** (1994) 11.

19. W. J. Hehre, L. Radom, P. v.R. Schleyer and J. A. Pople, *Ab Initio Molecular Orbital Theory*, Wiley (1986), page 230.

20. S. Berski, B. Silvi, J. Lundell, S. Noury and Z. Latajka, in C. Minot, *et al.* (Eds), *progress in Theoretical Chemistry and Physics*, Kluwer, Amsterdam, **1** (2001) 259.

CHAPTER 7

RgC_2 Clusters

7. RgC_2 CLUSTERS

7.1. INTRODUCTION

Small carbon clusters continue to be the target of intense scientific interest. These species are important because they are the building blocks of larger carbon clusters such as buckminsterfullerene. In addition carbon clusters are increasingly seen as key molecules in the formation of smaller electronic components.[1] Carbon nanotubes are one possibility for the next generation of smaller electronic components. They are produced in a gas phase reaction whereby carbon atoms condense at the end of a growing tube.[2]

The simplest carbon clusters C_2 and C_3, have been extensively studied both experimentally and theoretically. For example fluorescence from C_2 and C_3 molecules in a variety of environments has been observed.[3-7] Although there is a large body of information on small carbon clusters, almost nothing is known about their van der Waals complexes with rare gas atoms. In fact the sole reported piece of work was an *ab initio* study of Ar-C_2 by Naumkin and McCourt.[8] This is somewhat surprising given that similar species such as N_2-Ar and O_2-Ar have been known for many years.[9-14] The problem is, of course, partly experimental since relatively extreme conditions are required to generate useful quantities of C_2 in the gas phase. Nevertheless, it should be possible to form rare gas-C_n complexes using laser ablation of a carbon target followed by supersonic cooling *providing* the complexes possess a significant dissociation energy.

In their 1997 study of Ar-C_2, Naumkin and McCourt employed the CCSD(T) method coupled with the correlation consistent aug-cc-pVTZ basis set. The potential energy surface for the ground electronic state was constructed and it was found that at

equilibrium the complex is linear. Naumkin and McCourt obtained a D_0 of 85.5 cm^{-1} for the van der Waals bond following a calculation of rovibrational levels of Ar-C_2.

Although the aug-cc-pVTZ basis set is a good one for calculations on chemically bound molecules, it is relatively small for calculations on van der Waals complexes. In order to recover most of the dispersion energy, which will be the principal binding force in Ar-C_2, a more flexible basis set is generally required. Such calculations can be expensive, especially for generating an adequate number of potential energy points to fully map the potential energy surface. A more economical procedure is to retain small basis sets but to employ an extrapolation procedure to approach the complete basis set limit.

As discussed in Chapter 5, the simple basis set extrapolation procedure introduced by Truhlar in 1999 can be adapted for calculations on van der Waals complexes.[15] This extrapolation is based on CCSD(T) calculations using two standard correlation consistent basis sets. The calculations on 15 van der Waals complexes presented in Chapter 5 show that even for two small basis sets, the aug-cc-pVDZ and aug-cc-pVTZ sets, more than 95 % of the binding energy can be obtained *providing* the counterpoise correction is incorporated into the procedure.

In this work the modified Truhlar extrapolation has been applied to He-C_2, Ne-C_2 and Ar-C_2. The work on Ar-C_2 builds upon that of Naumkin and McCourt. The qualitative conclusions of Naumkin and McCourt are confirmed, but we find a significantly higher dissociation energy. Our calculations on HeC_2 and NeC_2 are the first calculations of van der Waals complexes between helium/neon and carbon clusters. The implications of our findings for spectroscopic studies of complexes between carbon clusters and rare gases are discussed.

7.2. COMPUTATIONAL METHODS

The modified Truhlar extrapolation (as described in Chapter 3) was applied to RgC_2 complexes. Firstly, a CCSD(T)/aug-cc-pVTZ calculation was carried out on C_2 to determine the equilibrium bond distance, which was found to be 1.250 Å. The interaction between C_2 and a rare gas atom is expected to be weak. Consequently little change in the C-C distance will occur on complex formation and therefore in these calculations the C-C distance has been fixed at the free C_2 value in all cases. Calculations on ArC_2 and NeC_2 were performed using MOLPRO,[16] whereas those on HeC_2 were performed using Gaussian 94.[17]

The potential energy surfaces of the RgC_2 clusters were calculated as a function of the two Jacobi coordinates: the distance from the rare gas atom to the centre of mass of C_2 (r), and the angle θ between r and the C_2 internuclear coordinate (R). The equilibrium distance was found by first making a rough determination with a CCSD(T)/aug-cc-pVDZ geometry optimisation, and then a little more precisely with a geometry optimisation at aug-cc-pVTZ. By making use of symmetry the entire angular coordinate can be mapped out by calculations with $90^\circ \leq \theta \leq 180^\circ$. The distance coordinate was investigated for approximately twelve distances around the estimated equilibrium bond distance, the typical step size being 0.2 Å. After counterpoise correction the *ab initio* data were extrapolated using the modified Truhlar extrapolation. The potential energy surface generated by the modified Truhlar extrapolation was then interpolated, using a bilinear interpolation method available in the Microcal Origin program, to generate a finer grid of points. A 4X4 interpolation was carried out so that the interpolated grid contains sixteen times as many points as the purely *ab initio* grid. The finer grid of points was then used to generate the potential energy surfaces presented here. From the potential surface, the

global minimum occurs for a linear geometry ($\theta = 180^{o}$). In addition, a saddle point is found for the T-shaped geometry ($\theta = 90^{o}$).

The *ab initio* data (after modified Truhlar extrapolation) were then used to produce a 2D graph of potential energy versus *r* at each of the turning point angles. Microcal Origin was then used to fit a 6-order polynomial to each 2D graph of *ab initio* data to determine *r* at the minimum energy, for that angle. Thus *r* and θ, at equilibrium and the saddle point, are now known.

The *ab initio* potential energy points were then used to determine rovibrational energy levels. The starting point was to find a more sophisticated potential energy function to fit to the *ab initio* data. The chosen functional form was based on the Dymond-Rigby-Smith (DRS) potential.[18] In the original work using this potential it was applied to the rare gases and was found to predict the correct temperature dependence of the second viral coefficients. The DRS potential has the added advantage that it is relatively simple.

The form of the potential function used is

$$V(r,\theta) = \sum_{\lambda}\sum_{n}\frac{C_n}{r^n}P_{\lambda}(\cos\theta) \qquad (7.1)$$

where r and θ are the Jacobi coordinates defined earlier, and $P_{\lambda}(\cos\theta)$ is a Legendre polynomial of order λ.

In this work the full DRS potential energy expansion has been used for the isotropic part of the RgC_2 potential. This involves terms in r^{-6}, r^{-8}, r^{-18}, r^{-24} and r^{-28}. However, to reduce the computational expense the radial contribution to the anisotropic terms was reduced to a simple Lennard-Jones 6-12 potential energy

function. The coefficients included in the expansion are summarised in Table 7.1 for the ArC_2 case. Because of the symmetry of RgC_2 only even order Legendre polynomials were required and the expansion in these was truncated at the sixth order. The coefficients were determined by a least squares fit of the *ab initio* potential energy points to the chosen potential energy function. For all three van der Waals complexes considered the standard deviation in the fit was <5 cm^{-1}.

Table 7.1. Values of coefficients used in the DRS potential energy expansion for ArC_2.

	n	C_n
$\lambda = 0$	-28	0.3104
	-24	-1.1813
	-18	2.0497
	-8	-1.2819
	-6	-1.4839
$\lambda = 2$	-12	0.4486
	-6	-0.7225
$\lambda = 4$	-12	-0.0288
	-6	-0.0125
$\lambda = 6$	-12	0.0220
	-6	-0.0330

To calculate the rovibrational levels of the complexes, standard computer programs applicable to relatively rigid molecules are not appropriate. Instead, the program BOUND, written by Jeremy Hutson, was employed.[19] The potential energy function described above was used as input into the program and it then proceeded to solve the Schrödinger equation for nuclear motion using a coupled channel method. Full details have been provided elsewhere by Hutson.[20] The energy level calculations were restricted to levels with overall angular momenta (J) of 0 or 1.

7.3. RESULTS AND DISCUSSION

7.3.1 ArC_2

ArC_2 is the only RgC_2 cluster that has been subjected to previous study. The *ab initio* data of Naumkin and McCourt[8] are compared to the data calculated by the modified Truhlar extrapolation in Table 7.2. According to Naumkin and McCourt, at equilibrium the complex has a linear geometry, and a saddle point was found for the T-shaped geometry. The work presented here also predicts a minimum at linear geometry and a saddle point when T-shaped. Naumkin and McCourt have calculated a coarse grid (0.25 Å) of *ab initio* data compared to the present work and consequently their results from CCSD(T)/aug-cc-pVTZ calculations are slightly different.

Table 7.2. ArC_2 structural data.[a]

		aug-cc-pVDZ	aug-cc-pVTZ	Extrap.[b]	Naumkin *et al.*[c]
θ=180°	r_e / Å	4.212	4.093	4.006	4.13
	D_e / cm^{-1}	89.0	113.9	134.9	115.0
θ=90°	r / Å	4.069	3.937	3.863	4.00
	D / cm^{-1}	59.0	87.0	106.9	88.1

(a) All calculations in this work were performed using CCSD(T) and a fixed C-C distance of 1.250 Å. The counterpoise correction was employed.

(b) Modified Truhlar extrapolation using the aug-cc-pVDZ and aug-cc-pVTZ data.

(c) Results from ref. 8. CCSD(T)/aug-cc-pVTZ calculations were used with the C-C distance fixed at 1.25 Å. Naumkin and McCourt data is given to the accuracy quoted in ref. 8.

Figures 7.3 and 7.4 show a 3D potential surface and a contour plot of the calculated *ab initio* data after interpolation.

For linear ArC_2 the modified Truhlar extrapolation calculates D_e to be 134.9 cm^{-1}, which is significantly deeper than the aug-cc-pVTZ calculation. The modified Truhlar extrapolation gives r_e = 4.006 Å, which is slightly shorter than the aug-cc-pVTZ value. r_e is a Jacobi coordinate, which means that the equilibrium separation between Ar and the nearest C atom is actually 3.381 Å.

For T-shaped ArC_2, the modified Truhlar extrapolation again predicts a significant deepening of the potential well and shortening of r compared to aug-cc-pVTZ. The distance of the argon from the closest carbon atom increases from 3.381 Å when linear to 3.913 Å when T-shaped.

Figure 7.1 shows the calculated energy levels for ArC_2 obtained from BOUND. The calculations yield D_0 = 102.2 cm^{-1} and therefore the zero point energy (D_e - D_0) is 32.7 cm^{-1}. The height of the saddle point above the minimum can be calculated from the data in Table 7.2, as the difference between the minimum energies at 180° and 90°. This simple calculation leads to a barrier height of 28.0 cm^{-1}. Figure 7.2 is a diagrammatical representation of the main features of the RgC_2 potential energy surface. The energy level calculations suggest that there are no rovibrational levels lying below the barrier/saddle point. It therefore seems likely that the C_2 moiety will easily undergo internal rotation, although it may be significantly hindered.

This confirms the findings of Naumkin and McCourt, although a larger D_0 is predicted in our new work. Naumkin and McCourt calculated that the zero point energy would lie just above the saddle point by ~4 cm^{-1}, which is very close to the ~5 cm^{-1} calculated in the work presented here.

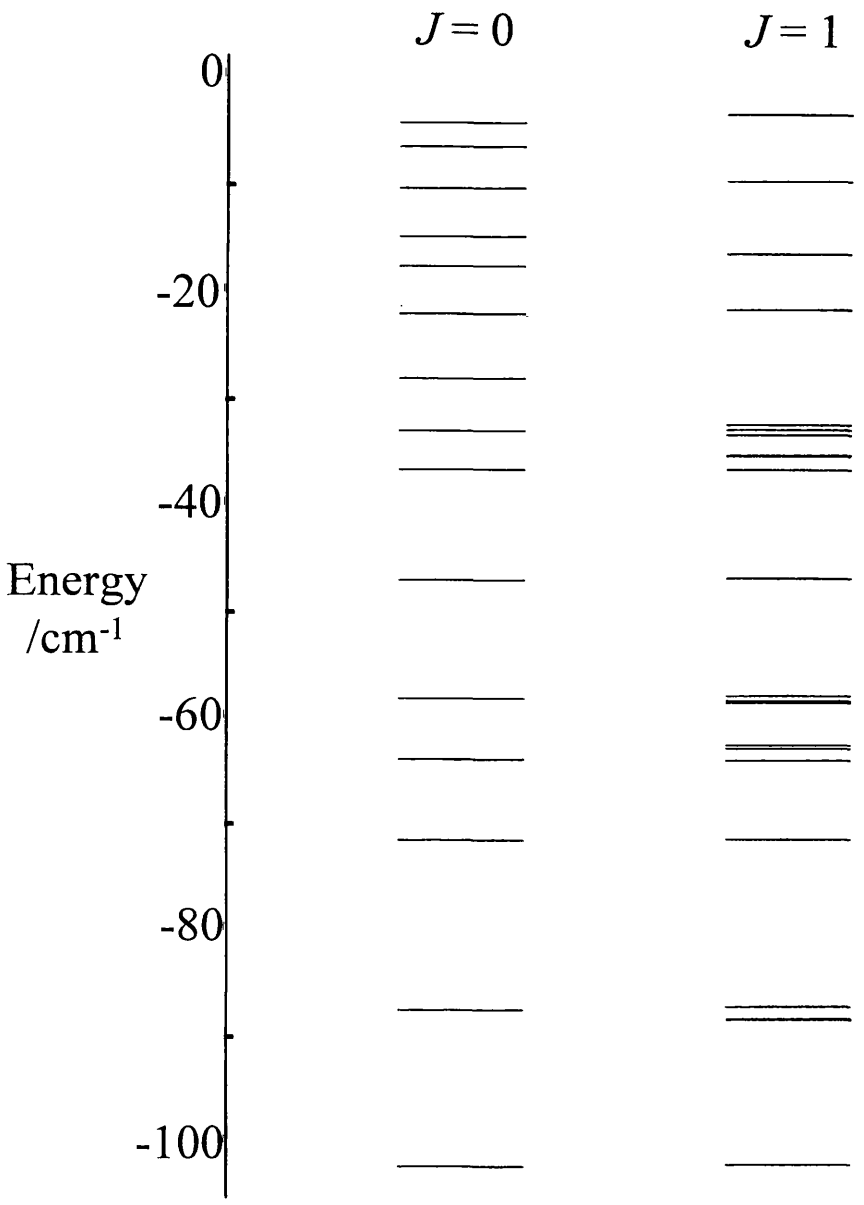

Figure 7.1. Plot of the ground state energy levels calculated for ArC_2.

The energy levels predicted in this work form a relatively complex pattern. However it is difficult to assign quantum numbers to the predicted rovibrational energy levels because they cannot be interpreted in terms of the normal rovibrator model used for relatively rigid molecules. To identify the character of the energy levels, it is necessary to inspect the form of the wavefunctions, an exercise that has not been carried out in this work. However, we can identify many similarities between the $J = 0$ and $J = 1$ manifolds. Although a crude approximation, the ArC_2 complex with freely rotating C_2 group can be regarded as an asymmetric top. For $J = 1$ we have, in the symmetrical rotor limit, $k = 0$ and $k = 1$ sub-states. In an asymmetric rotor the two-fold degeneracy of the $k = 1$ sub-states is resolved (into two levels with different parities) and this is the reason for the closely spaced doublets observed in the $J = 1$ stack.

A cursory inspection of the energy level diagram in Figure 7.1 suggests that the ground state van der Waals stretching frequency is approximately 30.7 cm^{-1}. This conclusion was arrived at because the -71.5 cm^{-1} level in the $J = 0$ manifold has a corresponding level in $J = 1$ (-71.4 cm^{-1}). The -71.4 cm^{-1} level in J = 1 is not split, implying that $k = 0$. Excited bending levels will generally correlate with $k \neq 0$. Consequently, these $J = 0$ and $J = 1$ levels correspond to purely stretching vibrations.

Clearly the van der Waals cluster ArC_2 should possess many bound rovibrational levels. This would indicate that under the right experimental conditions ArC_2 could be observed. The possible experimental methods that might be employed for detecting ArC_2, NeC_2 and HeC_2 are discussed in a separate section after all the results have been presented.

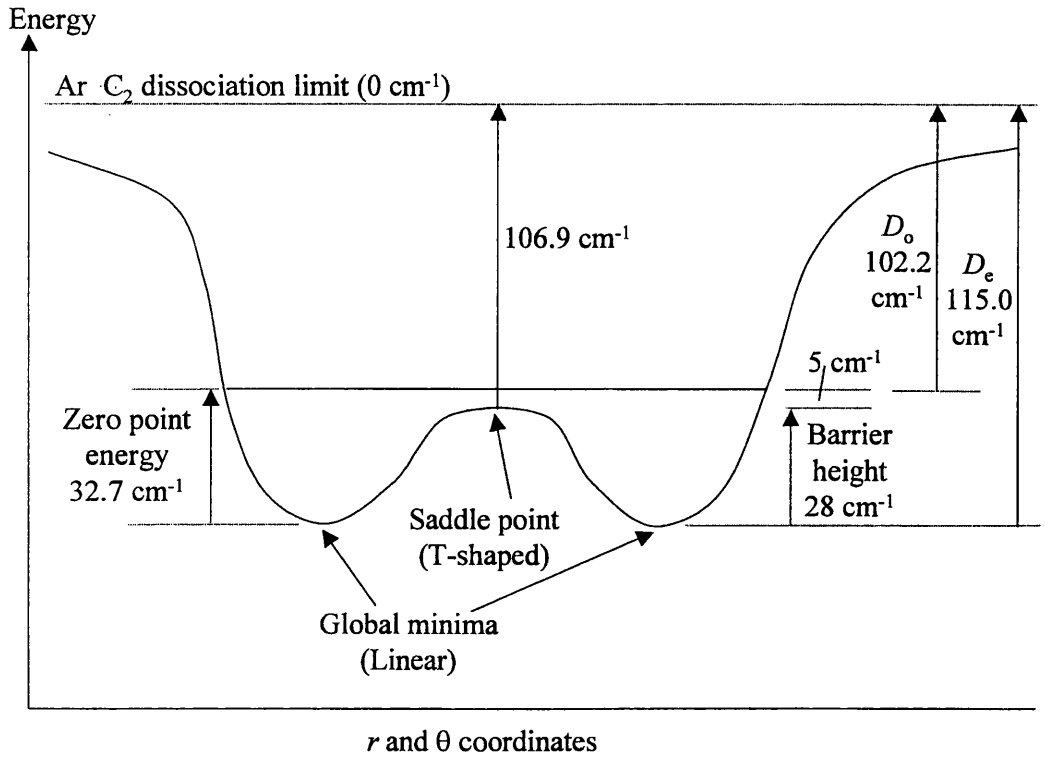

Figure 7.2. Diagram (not to scale) illustrating the main features of the ArC_2 potential energy surface. In this depiction both r and θ both vary along the horizontal axis.

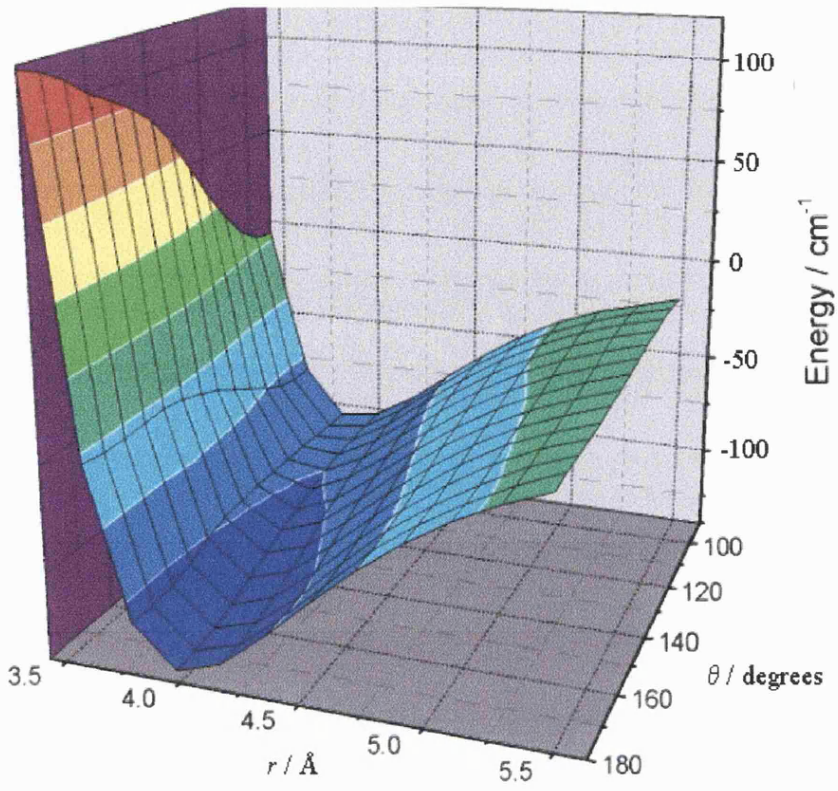

Figure 7.3 3D plot of ArC_2 potential energy surface. r and θ are Jacobi coordinates (see text for details). The surface shows the data after interpolation (see text for details).

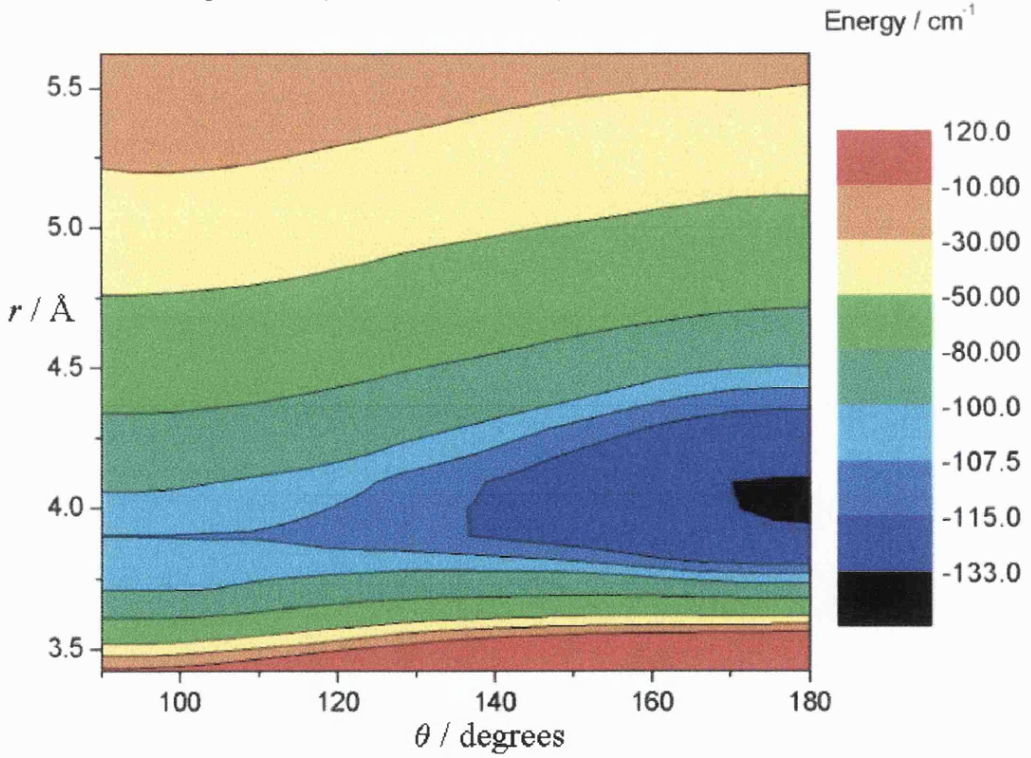

Figure 7.4 Contour plot showing ArC_2 potential energy surface. The colours in this figure do not represent the same contours as the colours in Figure 7.3.

7.3.2. NeC_2

No previous calculations or experimental studies have been performed on NeC_2. Table 7.3 shows r_e and D_e calculated using aug-cc-pVDZ and aug-cc-pVTZ basis sets and the modified Truhlar extrapolation.

Table 7.3. NeC_2 structural data.[a]

		aug-cc-pVDZ	aug-cc-pVTZ	Extrap.[b]
$\theta = 180^\circ$	r_e / Å	4.104	3.965	3.899
	D_e / cm^{-1}	24.8	38.4	48.3
$\theta = 90^\circ$	r / Å	3.933	3.746	3.654
	D / cm^{-1}	18.2	30.0	39.3

(a) All calculations in this work were performed using the CCSD(T) method and a fixed C-C distance of 1.250 Å. All data has been counterpoise corrected.

(b) Modified Truhlar extrapolation using the aug-cc-pVDZ and aug-cc-pVTZ data.

Figures 7.5 and 7.6 show a perspective view and a contour plot of the potential surface calculated by the modified Truhlar extrapolation. For NeC_2 the modified Truhlar extrapolation significantly deepens the potential well compared to aug-cc-pVTZ and aug-cc-pVDZ at both linear and T-shaped geometries. In a similar manner the bond distance decreases with the progression from aug-cc-pVDZ to aug-cc-pVTZ to extrapolated. The equilibrium structure for NeC_2 is found to be linear and NeC_2 has a saddle point at the T-shaped geometry in a similar manner to ArC_2.

If the neon to nearest carbon atom (Ne-C) distances are calculated for the two turning points, they are found to be 3.274 Å when linear and 3.707 Å when T-shaped.

Thus the Ne-C distance when linear is significantly shorter than the T-shaped geometry.

Figure 7.7 shows the calculated rovibrational levels for NeC_2. The zero point energy obtained is 18.6 cm^{-1}, and therefore D_0 is found to be 29.7 cm^{-1}.

The zero point energy level is 9.6 cm^{-1} above the saddle point on the potential energy surface, and hence the C_2 moiety can be expected to undergo relatively free rotation. NeC_2 is calculated to be bound and has a potential well containing 16 rovibrational levels (for $J = 0$ and $J = 1$).

The energy levels predicted in this work also form a series of closely spaced doublets. However as discussed earlier in the ArC_2 section, it is difficult to specifically assign quantum numbers to the rovibrational energy levels because they cannot be interpreted in terms of the normal rovibrator model used for relatively rigid molecules. However, inspection of the energy level diagram in Figure 7.7 suggests that the first excited van der Waals stretching level occurs at 18.8 cm^{-1}. This is clearly a very low stretching frequency and reflects the van der Waals bond in NeC_2.

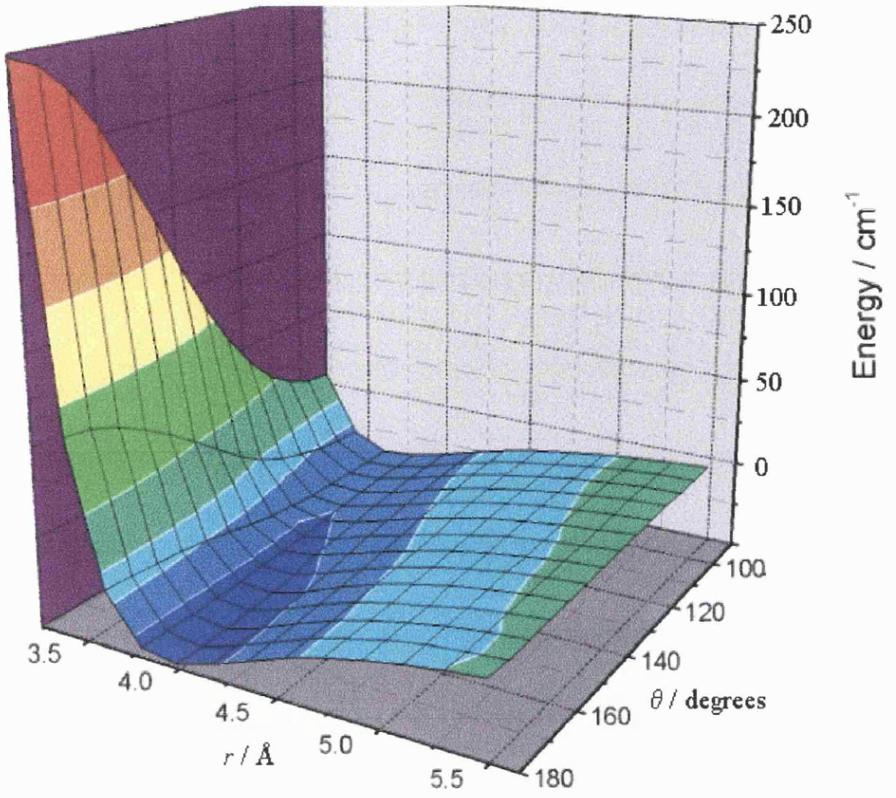

Figure 7.5 3D plot showing NeC_2 potential energy surface. r and θ are Jacobi coordinates. The surface shows the data after interpolation.

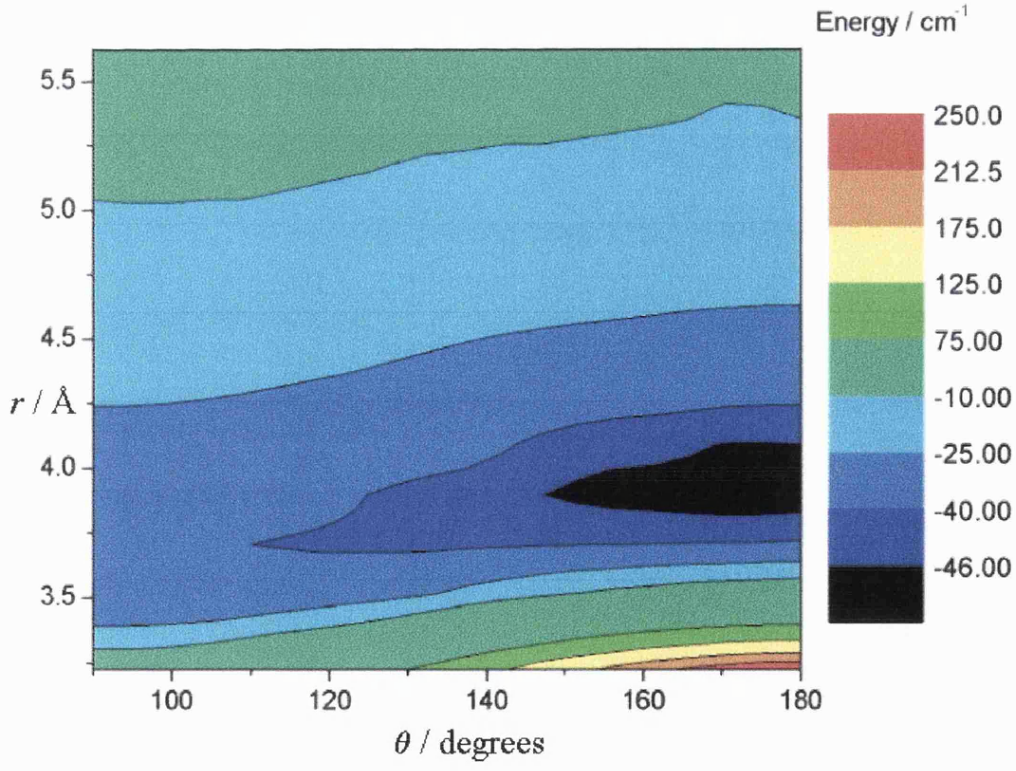

Figure 7.6 Contour plot of NeC_2 potential energy surface.

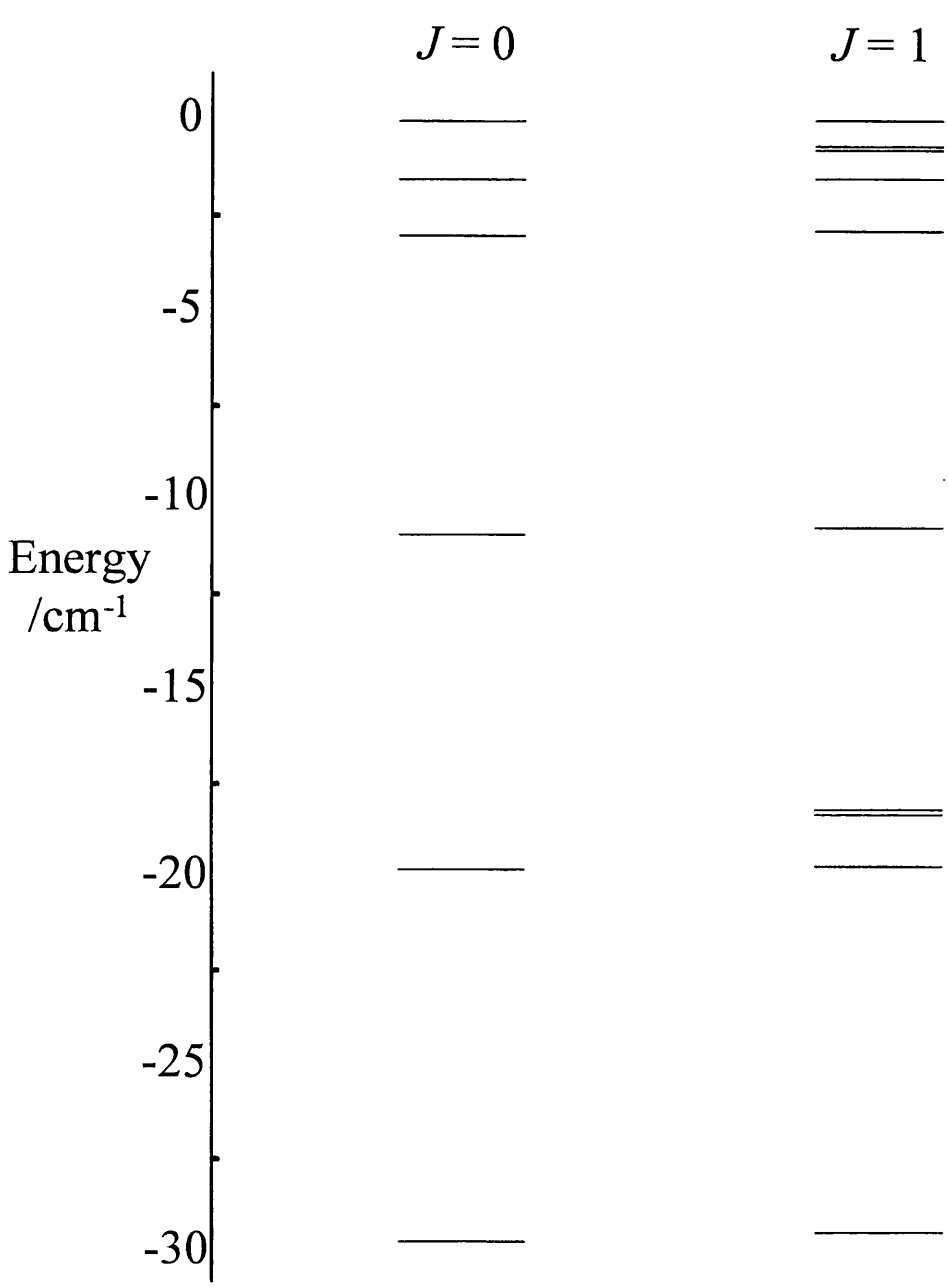

Figure 7.7. Plot of the electronic ground state energy levels calculated for NeC_2.

7.3.3. HeC_2

HeC_2 is by far the weakest bound of the van der Waals RgC_2 clusters studied but, as Table 7.4 shows, it does have a non-zero potential well depth.

Table 7.4. HeC_2 structural data.[a]

		aug-cc-pVDZ	aug-cc-pVTZ	Extrap.[b]
θ=180°	r_e / Å	4.086	4.019	3.971
	D_e / cm^{-1}	15.4	18.4	20.6
θ=90°	r / Å	3.984	3.827	3.740
	D / cm^{-1}	9.9	13.6	16.5

(a) All calculations were performed using CCSD(T) and a fixed C-C distance of 1.250 Å. All data has been counterpoise corrected.

(b) Modified Truhlar extrapolation using the aug-cc-pVDZ and aug-cc-pVTZ data.

Similar to ArC_2 and NeC_2, the modified Truhlar extrapolation provides a significant deepening of the potential well at both linear and T-shaped geometries compared to non-extrapolated calculations. In line with the deepening of the potential well, r also decreases from aug-cc-pVTZ to extrapolated at both linear and T-shaped geometries. Figures 7.8 and 7.9 show a 3D graph and contour plot of the interpolated *ab initio* data calculated using the modified Truhlar extrapolation.

The potential well of HeC_2 is very shallow and consequently is calculated to contain only one rovibrational level, which lies 5.8 cm^{-1} below the dissociation threshold. The zero point energy is calculated to be 14.8 cm^{-1}.

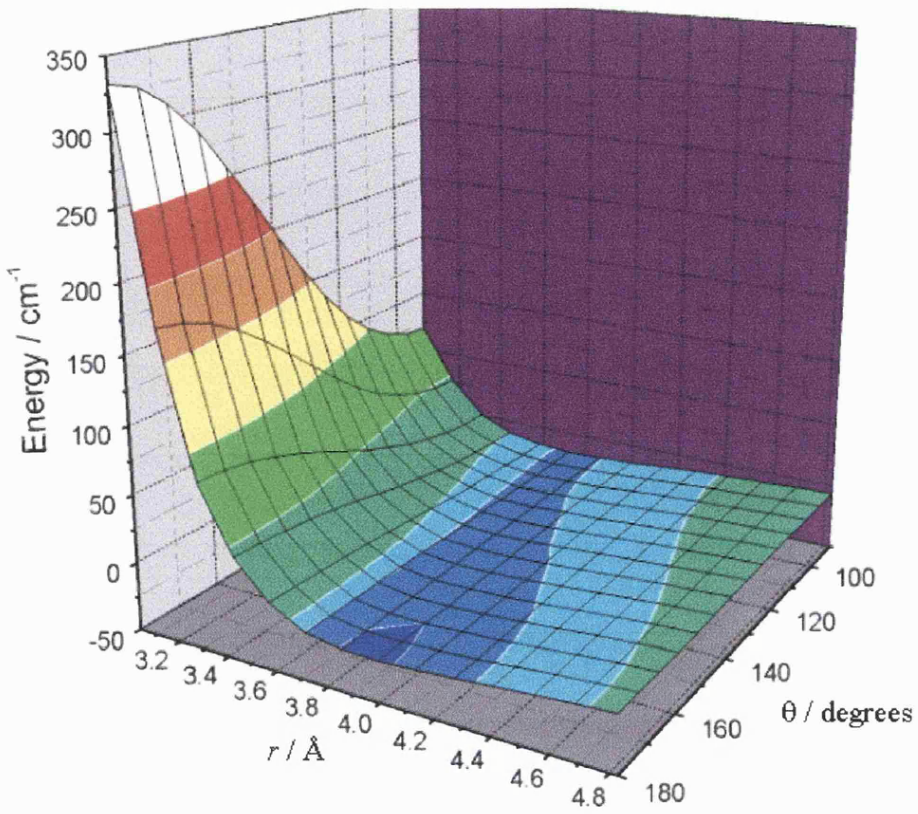

Figure 7.8 3D plot showing HeC_2 potential energy surface. r and θ are Jacobi coordinates. The surface shows the data after interpolation.

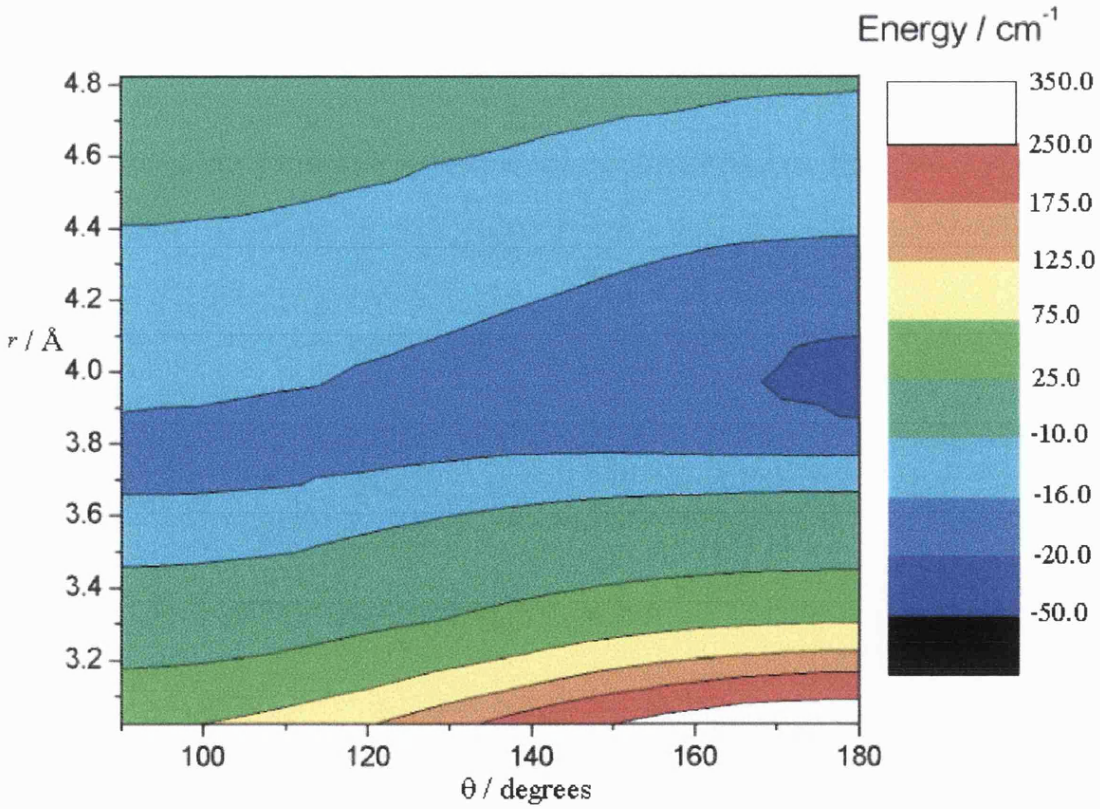

Figure 7.9 Contour plot showing HeC_2 potential energy surface.

7.4. IMPLICATIONS FOR EXPERIMENTAL OBSERVATION

The very shallow potential energy wells of all three RgC_2 molecules will make experimental observation of these species challenging. The ArC_2 van der Waals well (D_e = 134.9 cm^{-1}) has been calculated to contain a reasonable number of rovibrational levels, with D_0 being 102.2 cm^{-1}. Even though this bond is weak, many other van der Waals species with smaller binding energies have been observed before.

To observe RgC_2 species spectroscopically, a supersonic jet would be essential. Laser ablation could be used to produce C_2 from solid carbon. However the challenge would be to sufficiently cool the C_2 and/or RgC_2 such that any RgC_2 species formed do not dissociate prior to detection. This is particularly difficult in the vicinity of a laser ablation plasma. The use of an extended pre-expansion zone and/or pre-cooling of the nozzle and carrier gas may be necessary to ensure formation of significant quantities of these clusters.

To observe transitions in the ground electronic state of RgC_2, microwave spectroscopy would be the best option. Microwave studies of van der Waals and hydrogen bonded species, including rare gas-homonuclear diatomic species have been performed before. LIF spectroscopy could also be used to electronically excite RgC_2 species in an experiment similar to that described in Chapters 2 and 3 for BaOH.

Another possible technique for generating ArC_2 is in a low temperature matrix. Details for this type of experiment (applied to a different system) are discussed in Chapter 8. Matrix isolation avoids the problem of forming complexes in a relatively warm region. Instead, C_2 clusters could be formed by one of many techniques (laser ablation, thermal evaporation, electrical discharge) and deposited in the ultra cold matrix *before* complex formation.

Along similar lines to matrix isolation, ArC_2 could be trapped in a helium nanodroplet. These provide a fluid environment but at an ultra low temperature (0.18 K).[21] The ArC_2 complex could then potentially be observed with a variety of spectroscopic techniques, the most obvious being LIF spectroscopy.

NeC_2 is much less strongly bound than ArC_2 and would be far more difficult to produce and observe experimentally. However, it should be possible to trap and observe NeC_2 in a helium nanodroplet.

7.5. CONCLUSIONS

The potential energy surfaces of ArC_2, NeC_2 and HeC_2 have been calculated using the modified Truhlar extrapolation. For NeC_2 and HeC_2 the calculations presented here represent the first investigation of these complexes. In the case of ArC_2 there is a previous CCSD(T) study by Naumkin and McCourt.[8]

The ground state potential energy surface for all three clusters predicts linear equilibrium structures in each case. The calculated potential energy surfaces have been used to determine rovibrational energy levels for all three species. ArC_2 and NeC_2 are calculated to have a considerable number of bound energy levels, whereas HeC_2 is calculated to possess only one rovibrational level. Although difficult, it may be possible to form ArC_2 in a supersonic jet. However, it would certainly be possible to form both ArC_2 and NeC_2 in helium nanodroplets and therefore the prospects for observing these species spectroscopically are rather good.

7.6. REFERENCES

1. M. Gross, *Chem. Br.*, May 2002 Pg 36.

2. P. Birkett, *Chem. Br.*, May 1999 Pg 45.

8. F. Y. Naumkin and F. R. W. McCourt, *J. Chem. Phys.*, **107** (1997) 1185-1194.

3. A. N. Goyette, J. E. Lawler, L. W. Anderson, D. M. Gruen, T. G. McCauley, D. Zhou and A. R. Krauss, *J. Phys. D-Appl. Phys.*, **31** (1998) 1975.

4. P. E. Bengtsson and M. Alden, *Appl. Phys. B-Lasers Opt.*, **60** (1995) 51.

5. X. Y. Song, Y. H. Bao, R. S. Urdahl, J. N. Gosine and W. M. Jackson, *Chem. Phys. Lett.*, **217** (1994) 216.

6. E. A. Rohlfing, *J. Chem. Phys.*, **91** (1989) 4531.

7. T. Okada, Y. Kajiyama, H. Andou and M. Maeda, *Appl Phys B-Photo Phys.*, **47** (1988) 191.

9. A. R. W. McKellar, *J. Chem. Phys.*, **88** (1988) 4190.

10. J. Mettes, B. Heymen, P. Verhoeve, J. Reuss, D. C. Laine and G. Brocks, *Chem. Phys.*, **92** (1985) 9.

11. C. A. Long, G. Henderson and G. E. Ewing, *Chem. Phys.*, **2** (1973) 485.

12. G. Henderson and G. E. Ewing, *Mol. Phys.* **27** (1974) 903.

13. F. Pirani and F. Vecchiocattivi, *Chem. Phys.*, **59** (1981) 387.

14. G Henderson and G. E. Ewing, *J. Chem. Phys.*, **59** (1973) 2280.

15. P. R. Butler and A. M. Ellis, *Mol. Phys.*, **99** (2001) 525.

16. MOLPRO is a package of *ab initio* programs written by H-J Werner and P. J. Knowles with contributions from J. Almlof, R. D. Amos, A. Berning, M. J. O. Deegan, F. Eckert, C. Hampel, R. Lindh, W. Meyer, A. Nicklass, K. Peterson, R. Pitzer, A. J. Stone, P. R. Taylor, M. E. Mura, P. Pulay, M. Schutz, H. Stoll, T. Thorsteinsson and D.L. Cooper.

17. Gaussian 94/DFT, Revision B.2, M.J. Frisch, G.W. Trucks, H.B. Schlegel, P.M.W. Gill, B.G. Johnson, M.A. Robb, J.R. Cheeseman, T. Keith, G.A. Peterson, J.A. Montomery, K. Raghavachari, M.A. Al-Laham, V.G. Zakrzewski, J.V. Ortiz, J.B. Foresman, J. Cioslowski, B.B. Stefanov, A. Nanayakkara, M. Challacombe, C.Y. Peng, P.Y. Ayala, W. Chen, M.W. Wong, J.L. Andres, E.S. Replogle, R. Gomperts, R.L Martin, D.J. Fox, J.S. Binkley, D.J. Defrees, J. Baker, J.P. Stewart, M. Head-Gordon, C. Gonzalez and J.A. Pople, Gaussian, Inc., Pittsburgh PA (1995).

18. J. H. Dymond, M. Rigby and E. B. J. Smith, *J. Chem. Phys.*, **42** (1965) 2801.

19. J. M. Hutson, Bound computer code, version 5 (1993).

20. J. M. Hutson, *Comp. Phys. Commun.*, **84** (1994) 1.

21. J. P. Toennies and A. F. Vilesov, *Ann. Rev. Phys. Chem.*, **49** (1998) 1.

CHAPTER 8

Matrix Isolation

8. MATRIX ISOLATION

8.1 INTRODUCTION

8.1.1 BACKGROUND

Matrix isolation is a technique first performed in 1924 by the research group of Kamerlingh Onnes. Emission spectra of oxygen and nitrogen atoms trapped in matrices of nitrogen or mixtures of nitrogen and rare gases were investigated.[1] Matrix isolation became much more common in the 1960's upon the widespread availability of liquid helium and, more importantly, the advent of closed-cycle microrefrigeration units. Put simply, matrix isolation is the trapping of a molecule in a rigid cage (matrix) of a chemically inert substance, usually at a low temperature.[2] The solid inert matrix prevents the trapped species from translational movement, thus depriving it of the opportunity to react with any other chemical species. Thus matrix isolation offers the possibility of trapping short lived highly reactive intermediates indefinitely.

In reality a trapped species will inevitably undergo some perturbation by the matrix. Unless a particularly non-inert matrix is chosen the interaction between the matrix atoms and the trapped species is usually observed as a perturbation to the spectrum of the truly isolated species (*i.e.* in the gas phase). The best approximation to an inert matrix is one composed of rare gas atoms. To form such matrices very low temperatures are required.

Historically, matrix isolation has offered the opportunity to observe transient species such as radicals and unusual clusters with standard spectroscopic techniques. IR, Raman, E.S.R., UV/VIS absorption and emission spectroscopies have all been successfully applied in matrix isolation studies. In the past this was an invaluable strength. However, nowadays there are many techniques, particularly those based on

laser spectroscopy, that are highly effective in detecting gas phase species, including transient molecules. To some extent the importance of matrix isolation has therefore declined.

However, matrix isolation still has much to offer. For example, the interactions of trapped species with the matrix and the effect of these interactions when compared to the gas phase can offer valuable information on intermolecular forces. Using matrix isolation for this purpose turns the original idea on its head: the desire is to see some interaction between the host matrix and the guest molecule.

The cage effect in matrices can also be important. For example, new rare gas containing molecules of the form HRgF have recently been observed in rare gas matrices. *Ab initio* calculations on these species were described in Chapter 6. The xenon, krypton and argon species have all been synthesized for the first time using matrix isolation by Khriachtchev *et al.* [3-7] Indeed HArF represents the first ever chemically bound Ar-containing molecule.

8.1.2 THIS WORK

The matrix isolation experiments described in this chapter were intended to investigate the interactions between metal-containing free radicals and a matrix of nitrogen or a rare gas (mainly argon). These species are very weakly bound and would prove exceedingly difficult to produce and observe in the gas phase even under supersonic jet conditions. Matrix isolation offers a solution to this problem by enforced proximity of the radical to the 'solvent'.

8.1.2.1 Previous work

The matrix isolation chamber employed in this work was originally designed and constructed by Alison Beardah.[8] The chamber was designed specifically for detecting metal-containing transient species in rare gas matrices by LIF spectroscopy. After the chamber was constructed Beardah carried out some initial test experiments to ensure the system was working correctly. Unfortunately, these trial experiments were not particularly successful. Before attempting work on transient molecules, a test experiment on benzene was carried out. Benzene was chosen because it is a readily available and reasonably volatile liquid, has a LIF spectrum in the near-UV, and has previously been observed in a matrix environment. It is thus an excellent starting point for testing the system.

The dispersed fluorescence spectrum of benzene obtained by Beardah is shown in figure 8.1. The signal/noise ratio is poor and the vibrational structure (discussed later) is not well resolved. The primary problem appeared to be associated with scattered laser light and despite making some attempts to minimise this, the problem persisted. Consequently, Beardah was unable to attempt any experiments on matrix isolated transient molecules.

8.1.2.2 This work

This chapter describes attempts to improve on the earlier work by Beardah. A series of experiments were carried out with the aim of progressively improving the performance level of the apparatus. Initial work aimed at tackling the scattered laser light problem and obtaining much better LIF spectra of benzene. Having succeeded in that aim the following species were then investigated:

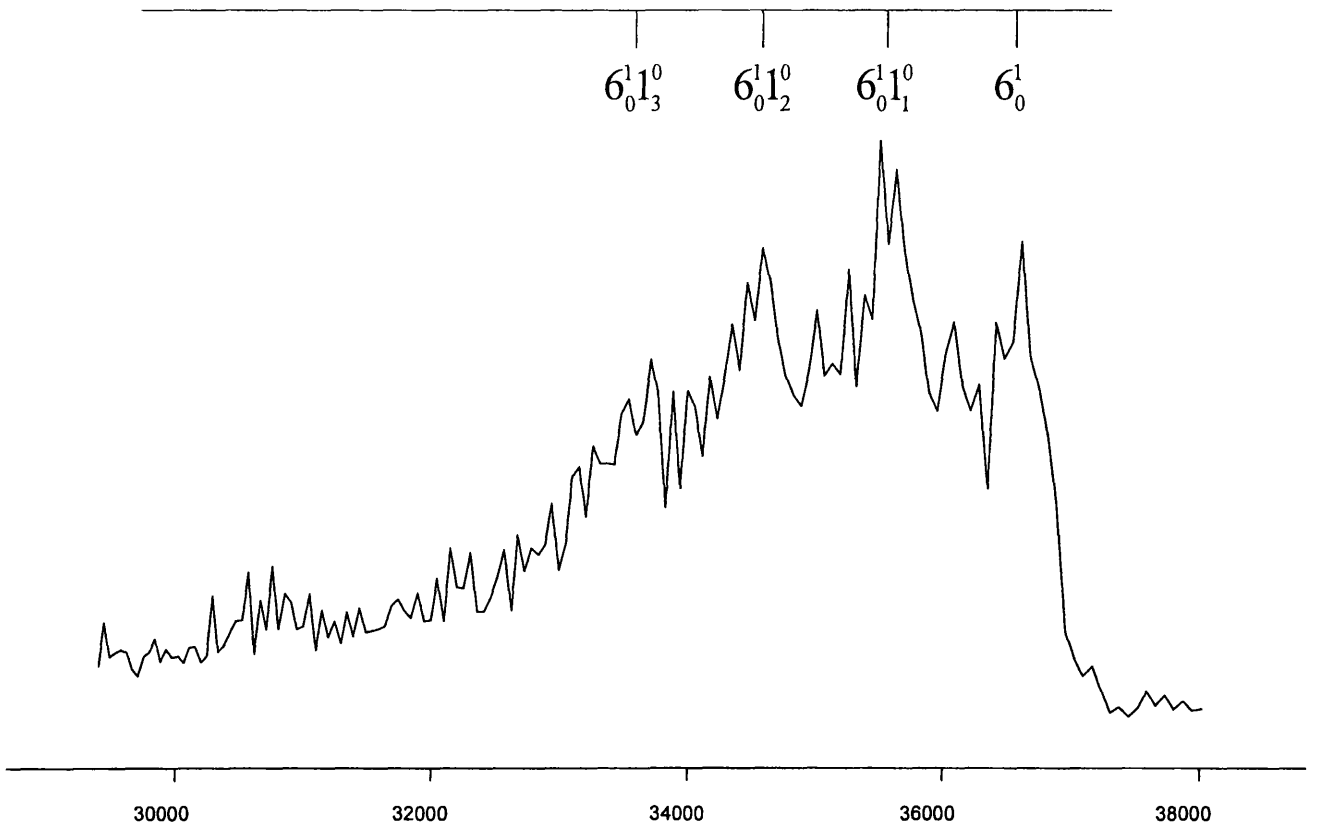

Figure 8.1 Dispersed fluorescence spectrum of the $\tilde{A}\,^1B_{2u}$ - $\tilde{X}\,^1A_{1g}$ electronic transition of benzene in a nitrogen matrix following laser excitation at 39370 cm^{-1}. This spectrum was recorded by A. Beardah.[8]

(I) *Ca and Ca_2.* These were chosen to establish the optimum conditions for trapping metal-containing species produced by laser ablation.

(II) *OH.* Before attempting experiments on metal-containing radicals an LIF investigation of the OH radical was carried out. This species has been extensively studied in rare gas matrices and therefore provided an important test of our ability to trap and detect free radicals.

Attention then switched to a metal-containing free radical. The chosen species, CaCl, has a strong and well known LIF spectrum. The results for CaCl, and the preceding experiments, are presented in this chapter. Before doing so, modifications made to the apparatus and the experimental procedure are described.

8.2 EXPERIMENTAL

The matrix isolation apparatus has been described in detail previously by Alison Beardah,[8] and so only a brief overview is provided here. The focus is mainly on the changes made to both the experimental conditions and the apparatus.

8.2.1 MATRIX ISOLATION APPARATUS

A schematic of the apparatus is shown in figure 8.2. It has three main functions: (i) radical production; (ii) trapping of radicals in an inert matrix; (iii) spectroscopic detection. Each is briefly described in the following pages.

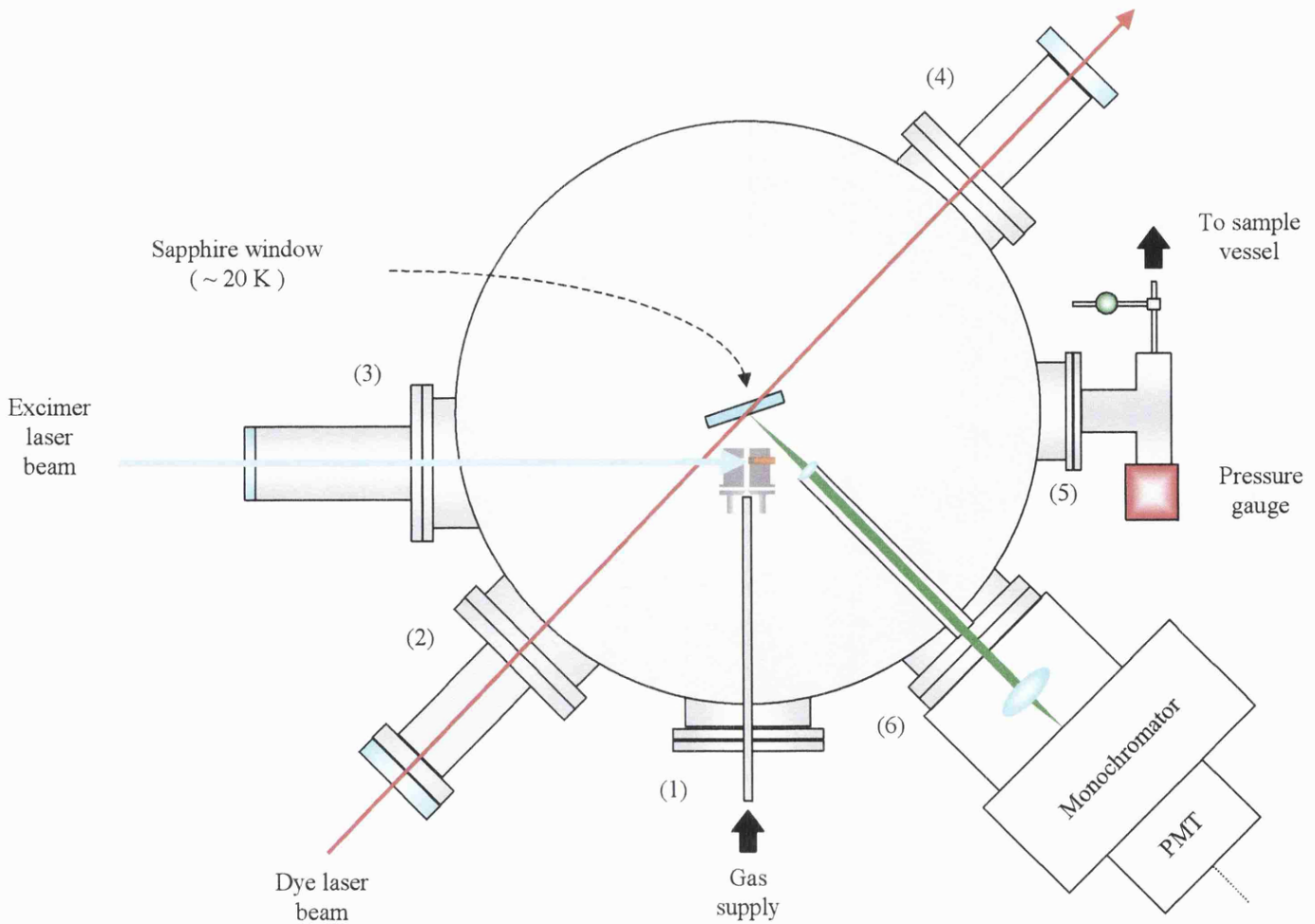

Figure 8.2 Schematic diagram of the matrix chamber. This is adapted from a similar diagram given by A. Beardah.[8]

8.2.1.1 Radical production

The aim was to generate metal-containing free radicals by reaction of metal atoms in the gas phase with a suitable precursor. The metal atoms are formed by laser ablation of a solid metal target. A small amount (typically 0.01-0.1% by volume) of the precursor is seeded into an inert carrier gas, which will later become the host in the matrix. The laser ablation procedure is entirely analogous to that already described for the gas phase experiments in chapter 2.

An important difference between the gas phase and matrix isolation experiments is that in the latter it is not possible to monitor the quality of the ablation procedure on a shot to shot basis by detecting fluorescence. The apparatus was not designed for the LIF detection of gas phase species. Consequently, the only real time monitoring of the quality of the ablation procedure, and hence the concentration of the desired molecules, is to visually observe the ablation flame protruding from the ablation fixture. Experience in the gas phase experiments leads to the conclusion that this is at best an uncertain indicator of the performance of the laser ablation process.

8.2.1.2 Matrix formation

Once formed in the reaction channel the short-lived species must be transported to the cold window whilst minimising the possibility of reactions. This is achieved by a (pulsed) supersonic expansion of the gas mixture into a vacuum.

Upon reaching the cold window, the carrier gas (usually argon) condenses as an inert matrix which traps the reactive species. Ideally, once trapped in the matrix the reactive species are immobile and isolated from each other and can therefore be preserved for many hours. The cold window is a sapphire disc, which is cooled to approximately 20 K by a closed cycle refrigeration unit (Cryodyne Cryocooler Model

21). In order to achieve this temperature it is necessary to locate the window in a high vacuum (~$1x10^{-5}$ mbar or lower).

The closed cycle refrigeration unit consists of a cold head driven by a compressor unit. The compressor is used to supply the helium gas to the cold head at ~20 bar and to remove the excess heat from the helium returning from the cold head. The cold head assembly (figure 8.3) shows the sapphire window inside the copper mounting block that is attached to the cold station. The cold station is cooled by the helium expansion inside the second cooling stage of the cold head.

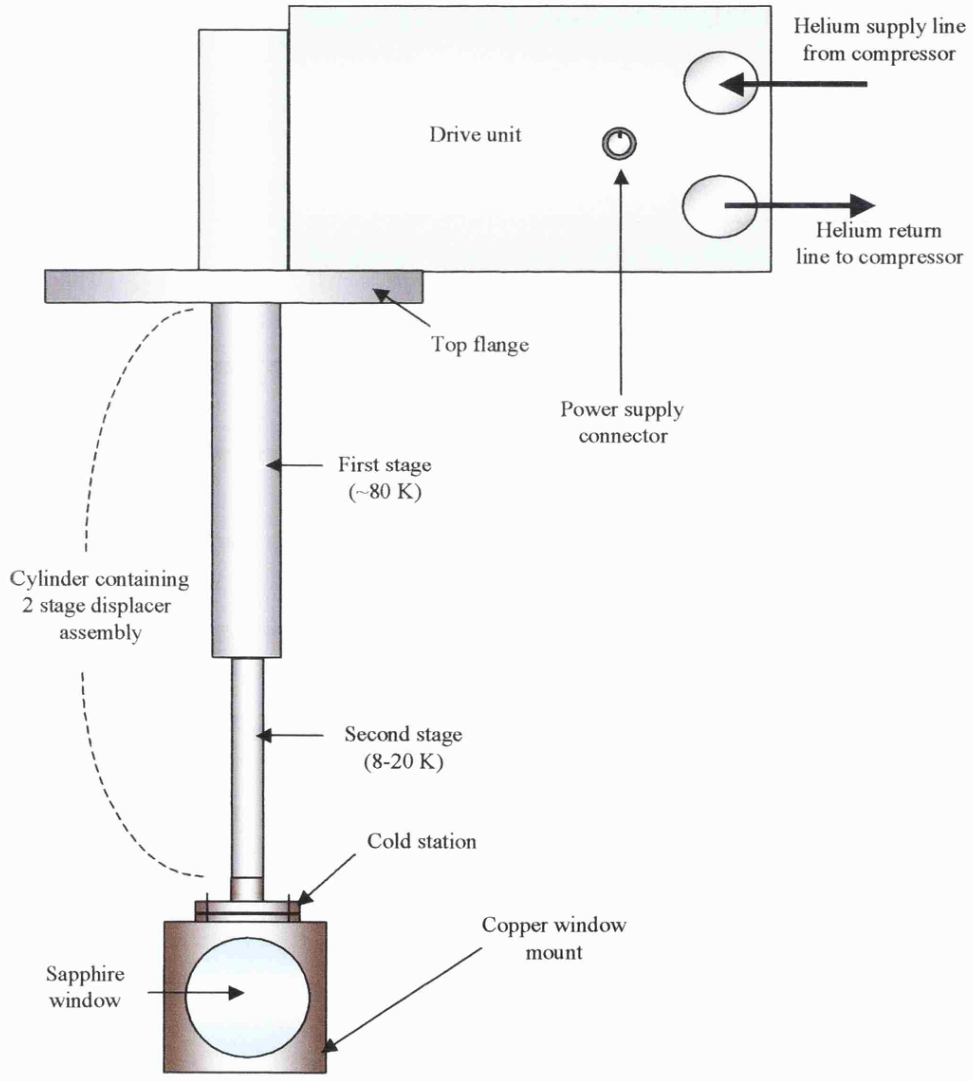

Figure 8.3 Schematic diagram of the cold head. This is adapted from a similar diagram given by A. Beardah.[8]

8.2.1.3 Detection

A pulsed tuneable dye laser was used to probe the guest species within the matrix. Fluorescence was collected by a lens, filtered by one or more long wavelength pass filters and/or a monochromator, and detected by a photomultiplier tube (PMT). Signal from the PMT is then processed as described in chapter 2 for the gas phase LIF work.

8.2.2 CHANGES MADE TO MATRIX ISOLATION EXPERIMENT AND APPARATUS.

During the testing and development stage of the new matrix isolation rig many small but important changes were made to the original equipment and the experimental procedure. Some of the more important changes are described below.

8.2.2.1 A new window

The first alteration, made even before the first experiments described below were performed, was to change the cold window from fused silica to one made from sapphire. Sapphire has much improved thermal and optical properties compared with fused silica. The sapphire window did not significantly reduce the temperature as recorded by the silicon diode temperature sensor (a Lake Shore Cryotronics DT-470-CU model) because the diode sensor is attached to the copper block beneath the window, and therefore does not measure the temperature of the window directly. However, the improved thermal conductivity of the sapphire window allows more efficient removal of heat from the centre of the window and hence faster cooling of the matrix during deposition.

8.2.1.2 Other physical changes

During testing and development several other apparatus changes were made.

(i) The base vacuum inside the chamber was improved, from a routine pressure of 8×10^{-6} mbar to 2×10^{-6} mbar. This was achieved by elimination of several small leaks at various locations in the vacuum chamber.

(ii) Light baffles were added to the dye laser exit arm (flange 4 in figure 8.2). This dramatically reduced the amount of scattered laser light reaching the PMT.

(iii) The majority of the surfaces inside the chamber were coated with a graphite film. This further reduced the amount of scattered dye laser light reaching the PMT.

(iv) A light collection cone was added onto the end of the fluorescence collection tube to ensure that light coming directly from the cold window was primarily fluorescence from deposited species, thus once again reducing the intensity of scattered laser light.

8.2.1.3 Changes to experimental conditions

The experimental conditions were optimised over many different experiments and the following conclusions were drawn.

(A) Deposition conditions very similar to those below generally worked for all experiments.

(i) 400 μs gas pulse - reasonably short to reduce the quantity of excess gas reaching the cold window and thereby not overloading the cold head (which could cause the window temperature to rise substantially).

(ii) 3 Hz pulse rate - if the pulse rate is increased the cold head is overloaded during deposition.

(iii) 1-15 minutes deposition time - the best spectra were recorded when the deposition time was ≤ 15 minutes (with 3Hz / 400μs pulses).

(iv) 4-5 bar carrier gas pressure behind the pulse valve. There is always a trade off between two factors. The higher the backing pressure of the carrier gas the larger the quantity of gas released per 400 μs pulse, which may overload the cold head during deposition. However high pressures result in a better supersonic jet expansion and thus more reactive species will be trapped in the matrix.

(B) Guest:host ratio - precursor:carrier gas ratios ranged from 1:100 to 1:10000. However this is almost certainly a poor indicator of the radical:host ratio actually present, due to the unknown number of metal atoms (or radicals) produced in the laser ablation process and, subsequently, how many of these are converted into the desired species. Furthermore, not all of the target molecules will be truly isolated, since a guest:host ratio of 1:10000 or better is generally required to achieve this. However as shown in the results section, this does not prevent matrix isolated spectra of radicals being recorded.

(C) Annealing had little or no effect. Annealing is a common tool used in matrix isolated experiments. It consists of warming the matrix to between 30 % and 50 % of the melting point of the matrix (25 - 42 K for argon), maintaining this temperature for a short period of time (1-10 minutes), and then cooling the matrix back down to below 30 % of its melting point. This allows the trapped

species and the cage to rearrange locally to allow the most stable trapping site to be adopted; this often simplifies complex spectra. Despite many attempts, annealing had no observable affect on the spectra recorded in the present work. The reason for this surprising finding is unknown. However, it may be partly due to the fact that the warming process was carried out in a very crude manner, *i.e.* by temporarily switching off the cold/head compressor. This made it difficult to control the window temperature with any precision and therefore effective annealing may never actually have been achieved.

8.3 RESULTS

During testing and development the new matrix isolation rig was used to perform LIF and DF experiments on several species from large stable molecules to small radicals, with mixed success.

8.3.1 Benzene

As mentioned earlier, in the initial experiments by Alison Beardah[8] benzene was used for testing purposes. The electronic transition chosen for investigation was the $\tilde{A}^1B_{2u} - \tilde{X}^1A_{1g}$ system. As shown earlier in figure 8.1, the quality of spectra obtained by Beardah was poor.

In this work, after replacing the fused silica window with a sapphire one, and after further optimisation of the deposition conditions (pulse length, pulse rate, carrier gas pressure and concentration of benzene), much improved spectra of benzene were recorded. A nitrogen matrix was used to be consistent with the previous work by Beardah. Two of the much improved benzene spectra are shown in figures 8.4 and 8.5.

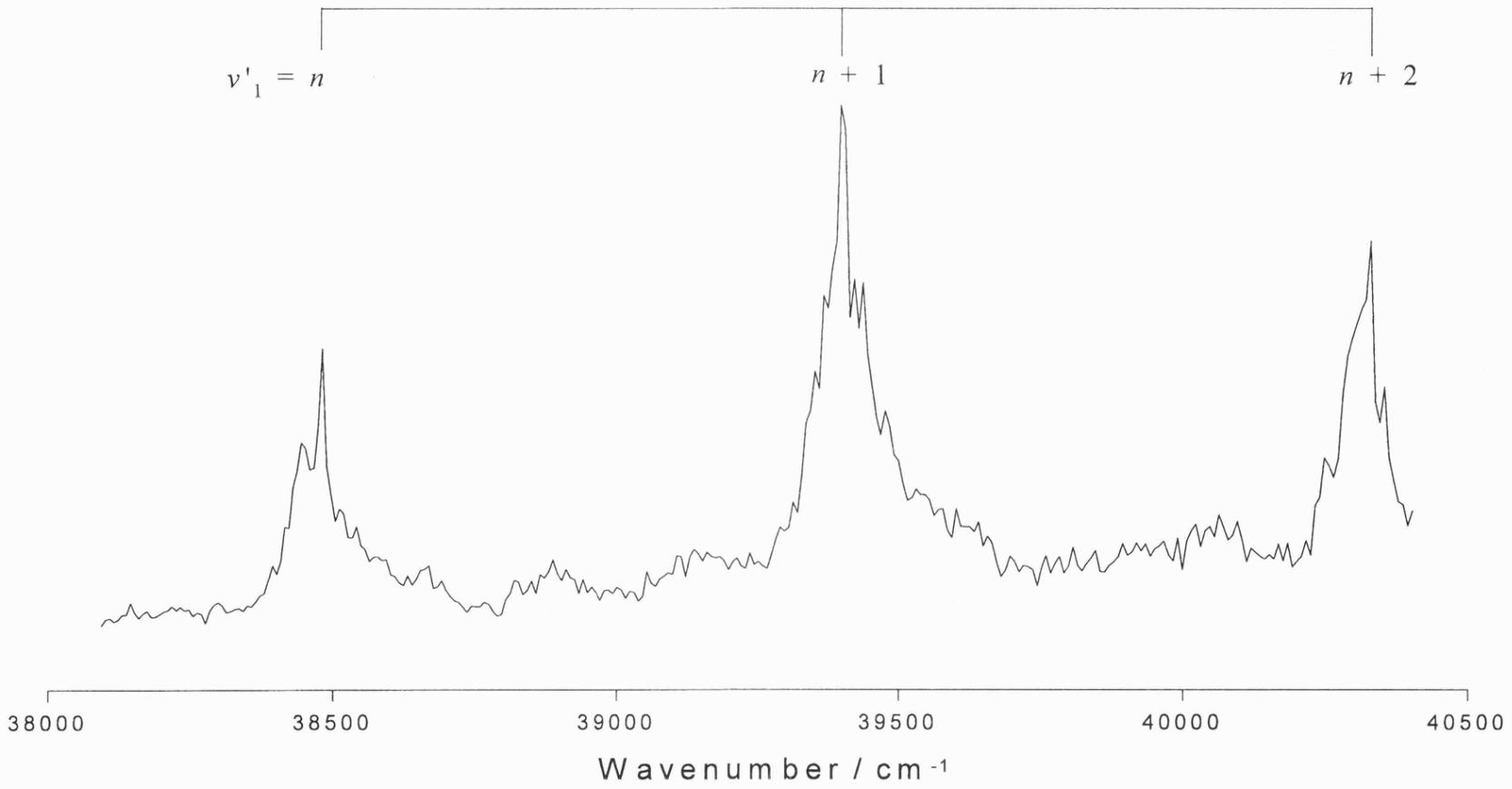

Figure 8.4 LIF excitation spectrum of the $\tilde{A}^1B_{2u} - \tilde{X}^1A_{1g}$ electronic transition of benzene in a nitrogen matrix. A vibrational progression in the ring breathing mode, v_1, is marked above the spectrum. This spectrum was obtained by scanning the dye laser wavelength and monitoring fluorescence at 36232 cm^{-1} with a monochromator/PMT combination.

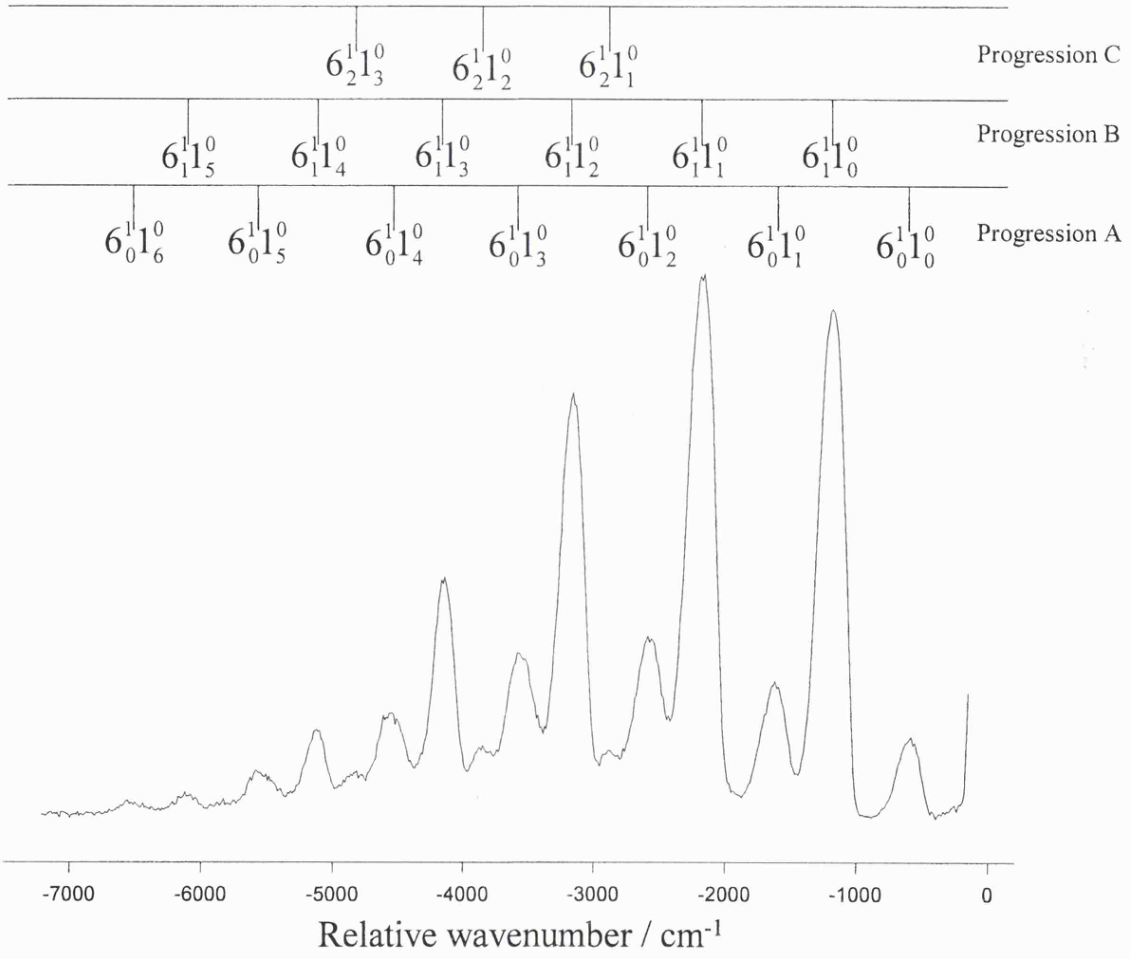

Figure 8.5 DF spectrum of the $\widetilde{A}^1B_{2u} - \widetilde{X}^1A_{1g}$ transition of benzene following excitation at 38462 cm^{-1}.

Figure 8.4 shows an LIF excitation scan of the $\tilde{A}$-$\tilde{X}$ transition. The monochromator was set to collect fluorescence at 36322 cm^{-1} while the laser was scanned from 40404 cm^{-1} to 38095 cm^{-1}. Figure 8.5 shows a typical dispersed fluorescence spectrum with the laser fixed at 38462 cm^{-1}, which corresponds to one of the peaks in the excitation scan. This can be compared with that in figure 8.1, and is clearly a dramatic improvement. Excitation at all three peak wavelengths in the excitation spectrum produced DF spectra very similar to the one shown in figure 8.5. The nitrogen matrix was kept at between 20-25 K during the 10 minute deposition and while spectra were recorded. All spectra were recorded through a monochromator with fairly narrow slits and no other filtering of the collected light.

The DF spectrum is in good agreement with emission spectra of benzene in matrices recorded previously by Gibson *et al.*[9, 10] The vibrational structure has been attributed to a progression in ν_1, the ring breathing mode, built upon the non-totally symmetric ν_6 vibration, an in-plane distortion of the ring caused by the simultaneous lengthening and shortening of two C-C bonds on opposite sides of the ring. The progression gives a ground state vibrational frequency of approximately 980 cm^{-1} for ν_1, which is reasonably close to the gas phase value determined by Callomon *et al.*[11] of 995.4 cm^{-1}. The matrix shift -15 cm^{-1}, is a modest shift for a nitrogen matrix.

The matrix isolated DF spectrum from this work is of a higher resolution than either the gas phase work of Callomon *et al.* or the matrix isolated work of Gibson *et al.* Unlike either of these earlier works, the spectrum in figure 8.5 actually consists of two strong progressions (labelled A and B, B being the strongest) and a third much weaker progression (labelled C). The vibrational interval in all three progressions is approximately 980 cm^{-1}. However, progressions A and B are offset from one another by approximately 600 cm^{-1}, and the same is probably true for progression C, although

the first members of this progression are likely masked by A and B. 600 cm^{-1} is very close to the frequency of ν_6 mode in the ground electronic state. Hence it is likely that the second progression will be a progression in ν_1 built upon $2\nu_6$, and in a similar fashion the third progression will be in ν_1 built upon $3\nu_6$. This has been assumed in the assignments shown in figure 8.5.

8.3.2 Atomic Calcium

Detection of atomic calcium was chosen as the first experiment involving metal atoms. Calcium atoms were generated by laser ablation of a solid calcium target in the presence of argon carrier gas. Bondybey and Brus[1] have previously reported the detection of calcium atoms in an argon matrix by UV/VIS spectroscopy. They reported excitation from the ground (^1S) state up to the $4s^14p^1$ ^1P state, followed by intersystem crossing to the lower $4s^14p^1$ ^3P state and emission back to the ground state. The relevant energy levels are depicted in figure 8.6.

The spectra reported by Bondybey and Brus were intense but very broad. Their bands showed a reasonably sharp onset on the long wavelength side, but long tails to shorter wavelengths. The broadening of the bands was attributed to large phonon side bands. Their phonon side bands in emission showed some structure.

The sharp onset of the band, or zero phonon line, represents the excitation energy of the trapped species only. Phonon side bands are caused by the energy levels of trapped species being perturbed by interactions with the matrix, *i.e.* excitation of lattice photons. The extent of the phonon side band is directly related to the *change* in interaction potential energy between the trapped species and the matrix on electronic excitation. In other words it is a Frank-Condon like effect. Since the Calcium atomic spectra recorded in the current work are shown in figures 8.7, 8.8 and

8.9. During excitation and emission scans it was necessary to use a combination of 600 nm and 620 nm long pass filters to reduce the intensity of scattered laser light (increase the signal to noise ratio) reaching the PMT. Figure 8.7 shows the excitation spectrum for the ^1P - ^1S transition whilst collecting emission at < 16130 cm^{-1} (> 620 nm) emitted from the lower ^3P state. Figure 8.8 shows the corresponding emission spectrum after excitation at 23810 cm^{-1}. Figure 8.9 shows an action scan over the same region as the excitation scan whilst emission was collected at ~15270 cm^{-1} only, by use of a monochromator to select a narrow range of frequencies for collection.

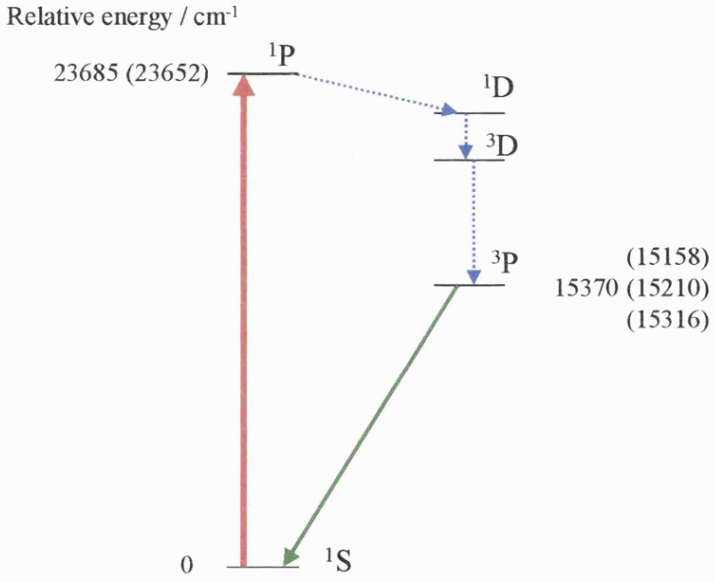

Figure 8.6 Low lying electronic energy levels of atomic calcium. Solid arrows represent absorption and emission. Dotted arrows represent non-radiative relaxation. Relative energies of the electronic levels determined from the onset of emission (zero phonon position) in figures 8.7 and 8.8 are indicated. Values in parenthesis indicate literature energies from gas phase emission.[1]

The spectra are in a similar wavenumber region to those reported by Bondybey and Brus for both excitation and emission. However, they differ in two important ways. Unlike the spectra of Bondybey and Brus, the bands in figures 8.7,

8.8 and 8.9 do not show a sharp onset, nor is any structure resolved in the phonon side bands. The source of the structure in Bondybey and Brus's spectra is unknown and therefore it is difficult to postulate why it is not observed in figures 8.7 and 8.8. However one possibility is that multiple site effects either cause the observed structure in Bondybey and Brus's spectra or obscure it in figures 8.7 and 8.8. The signal/noise ratio in figure 8.9 is much too weak to draw any conclusions about structure within the band envelope.

In conclusion, the new matrix isolation rig was successfully used to observe calcium atoms and their associated phonon side bands in both excitation and emission. However the absence of a sharp zero phonon line in figures 8.7 and 8.8 *may* indicate a possible problem. The S/N ratios in figures 8.7 and 8.8 are sufficient to record reasonable spectra, but quite poor considering that the LIF signal from atomic calcium would be expected to be very intense.

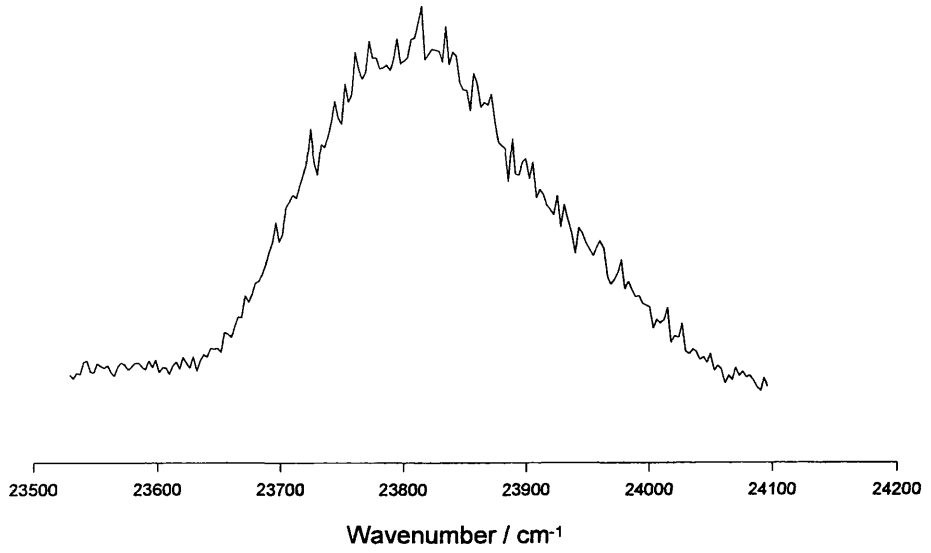

Figure 8.7 LIF excitation spectrum of the ^1P - ^1S electronic transition of atomic calcium isolated in an argon matrix. Fluorescence was filtered such that only emission from the ^3P - ^1S transition was observed. The band shows substantial phonon broadening. The laser dye curve artificially increases the intensity decay at higher wavenumbers.

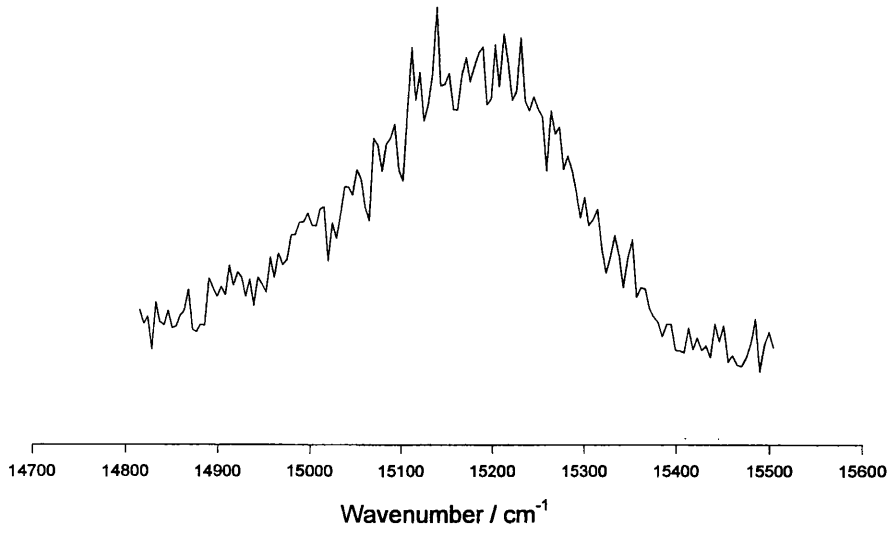

Figure 8.8 Dispersed fluorescence spectrum of the ^3P - ^1S transition of atomic calcium isolated in an argon matrix after excitation at 23810 cm^{-1}.

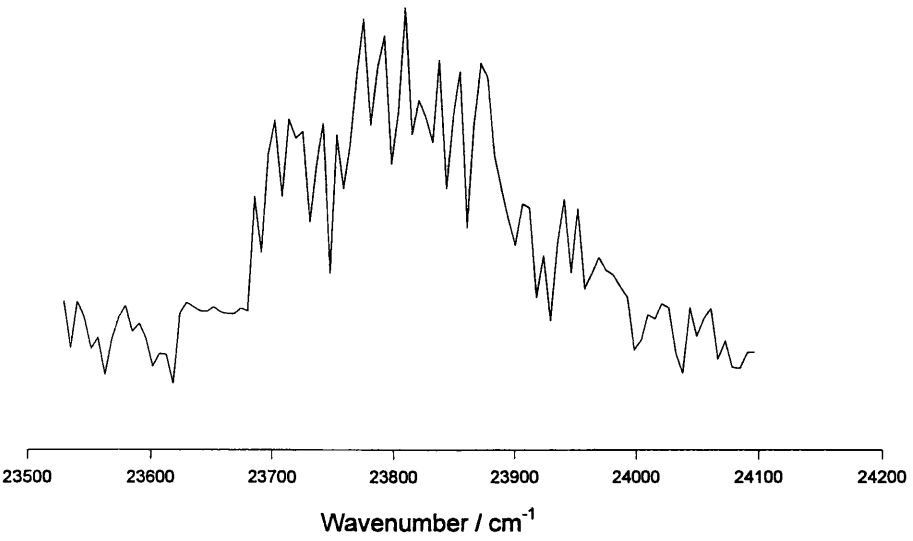

Figure 8.9 Action scan of the ^1P - ^1S transition of atomic calcium isolated in an argon matrix. Emission was collected at ~15270 cm^{-1} by use of a monochromator. The S/N ratio is poor because the intensity of collected emission was exceedingly low.

8.3.3 Calcium Dimer

After the initial success in observing atomic calcium in a rare gas matrix, efforts were made to detect Ca_2. Attention in this work focused on the $A\,^1\Sigma_u^+ - X\,^1\Sigma_g^+$ electronic transition, which falls in the red (origin at ~14750 cm^{-1}). Andrews, Dudley and Brewer[12] carried out a matrix isolation study on Ca_2, and found a long vibrational progression for the *A-X* system. This progression was not fully resolved due to phonon side bands broadening the observed peaks.

The experimental conditions used in the present work to observe Ca_2 were essentially the same as those used to observe atomic calcium. 680 nm and 700 nm long pass filters were required to adequately reduce the intensity of scattered laser light. The excitation spectrum recorded in the present work, shown in figure 8.10, is very similar to the spectrum of Andrews *et al.*, showing almost identical vibronic spacing, broadening due to phonon side bands, and virtually the same position of maximum absorption. For example, the average vibronic spacing in the *A* state is 109 cm^{-1} which compares very well to an average value of 111 cm^{-1} seen by Andrews *et al.*

8.3.4 Hydroxyl Radical

OH was chosen as the first test of the new matrix isolation apparatus for radical production and detection because it has a well-known and strong LIF spectrum. To produce OH, photolysis of H_2O_2 was employed. H_2O_2 vapour from a sample container maintained at 50 °C was seeded in to the argon gas stream before the pulsed valve. H_2O_2 was then photolysed at 193 nm using an ArF excimer laser in a laser ablation fixture prior to supersonic expansion, *i.e.* aside from the absence of a metal target the same experimental conditions as for the Ca/Ca_2 experiments were used.

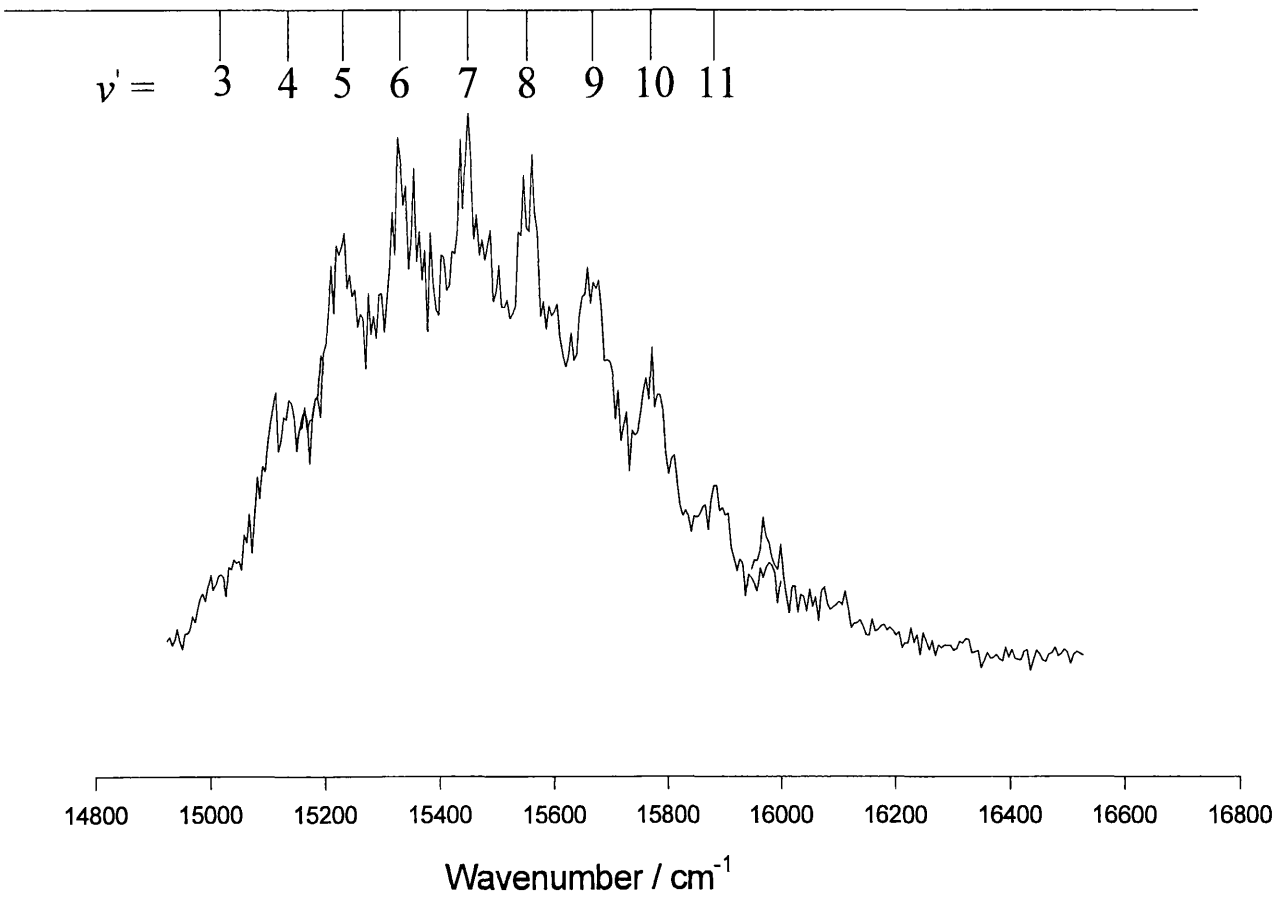

Figure 8.10 LIF excitation spectrum of the $A^1\Sigma_u^+ - X^1\Sigma_g^+$ electronic transition of Ca_2 trapped in argon. The spectrum is a composite of three scans recorded sequentially, which has resulted in slight discontinuities.

The small size of OH means it may easily diffuse through the matrix. Even if the average temperature of the matrix is low enough to maintain rigidity, localised heating at the surface of the matrix during deposition may allow OH to diffuse through the matrix and rapidly recombine. Hence, effective trapping and observation of OH will provide a strenuous test of the matrix rig and operating conditions.

Goodman and Brus[13] have previously observed the $A^2\Sigma^+ - X^2\Pi$ LIF spectrum of OH in an argon matrix. Their spectrum consisted of a broad band with a discernible low frequency progression built upon it, which was attributed to the Ar-HO stretch in the ArHO species.

In the present work an attempt was made to reproduce their excitation spectrum. Figure 8.11 shows an excitation spectrum of OH recorded in an argon matrix. This band is associated with the (1-0) vibrational component of OH in the *A-X* system. In general it has the same overall profile and position as Goodman and Brus's spectrum, but the low frequency progression mentioned above is not present. A possible explanation is a combination of poor S/N ratio and multiple site effects. Diffusion of OH molecules through the matrix, leading to perturbations of individual OH molecules by nearby OH radicals, would seem to be an unlikely explanation, despite the small size of OH. Diffusion should result in a gradual loss of signal over time, but the observed signal intensity was fairly constant over several hours.

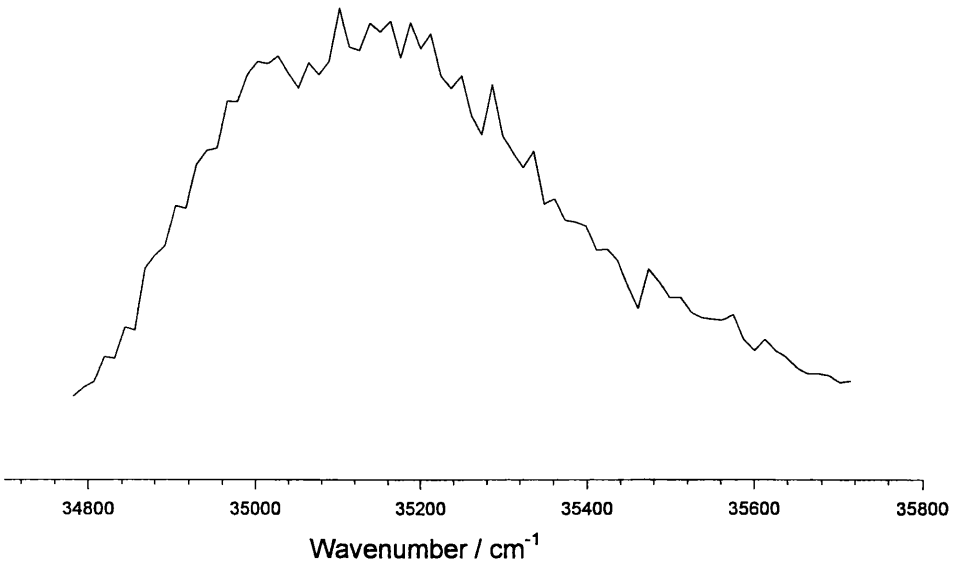

Figure 8.11 LIF excitation spectrum of the $A^2\Sigma^+ - X^2\Pi$ (1-0) electronic transition of OH radical trapped in an argon matrix.

The most likely explanation for the poor S/N ratio is that the cold head was not able to cope with the heat load from the depositing gas. The matrix window is nominally kept at 20-25 K during recording of spectra and during deposition. This is already a relatively high temperature for argon matrices. However, as mentioned in an earlier section, the temperature monitoring diode is not attached directly to the sapphire window and will certainly show a lower temperature than the surface of the matrix just after deposition. A matrix is usually considered rigid below 30 % of its melting point temperature.[2] For argon this is 25 K, so that the measured temperature is at the limit for the matrix to be considered rigid. It is likely that during deposition the temperature of the matrix rises above 25 K, perhaps conferring sufficient flexibility to allow substantial diffusion of OH. Recombination reactions would flourish under these conditions, which would reduce the number of OH molecules

trapped and hence reduce the fluorescence signal. The few surviving OH radicals would eventually become trapped beneath layers of argon and we speculate that these layers are sufficiently far from the deposition region that they achieve lower temperatures. This would explain why the OH signal remains largely unchanged for several hours.

One obvious solution to this problem would be to improve the cooling capacity of the cold head. Realistically this could only be achieved by installing a new cold head and compressor.

8.3.5 CaCl

Observation of CaCl would represent a culmination in the testing and development of the new matrix isolation rig. In order to produce this molecule, $CHCl_3$ was used as the Cl precursor.

CaCl has already been observed in an argon matrix by chemiluminescence from the reaction of Ca vapour and Cl_2, by Guo, Chang and Lee.[14] This study identified several electronic transitions and consequently approximate energies of the various excited states in an argon matrix are available. Here the focus is on excitation and DF spectra associated with the $A^2\Pi \leftarrow X^2\Sigma^+$ electronic transition of CaCl. Figure 8.12 shows the relevant energy levels.

Figure 8.13 shows a dispersed fluorescence spectrum of CaCl recorded in the present work after laser excitation at 16129 cm^{-1}. Excitation is to, and emission is from, the zero point level in the $A^2\Pi_{1/2}$ state. The transition has been significantly broadened by a phonon side band. However the zero phonon line is clearly visible at 15772 ± 15 cm^{-1}. Within experimental error this is the same as that observed by Guo

et al. at 15768 ± 12 cm^{-1}.[14] Aside from a shift in absolute position, the dispersed fluorescence spectrum following excitation to the $A^2\Pi_{3/2}$ state is identical to that from the $A^2\Pi_{1/2}$ component (see figure 8.14).

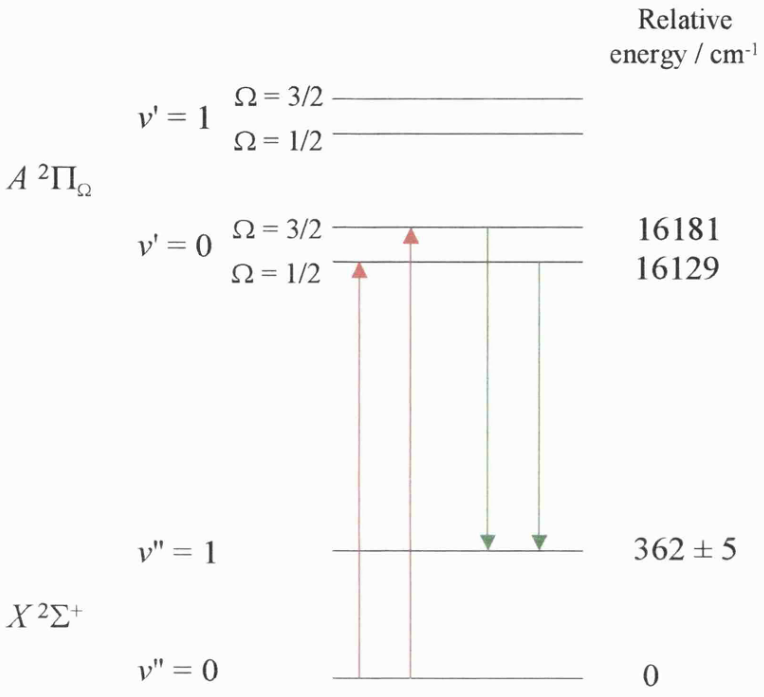

Figure 8.12 Energy levels of CaCl in an argon matrix, determined in this work. Ω refers to the electronic (orbital + spin) angular momentum projection quantum number. 320 nm long pass filters were used to reduce the intensity of scattered laser light.

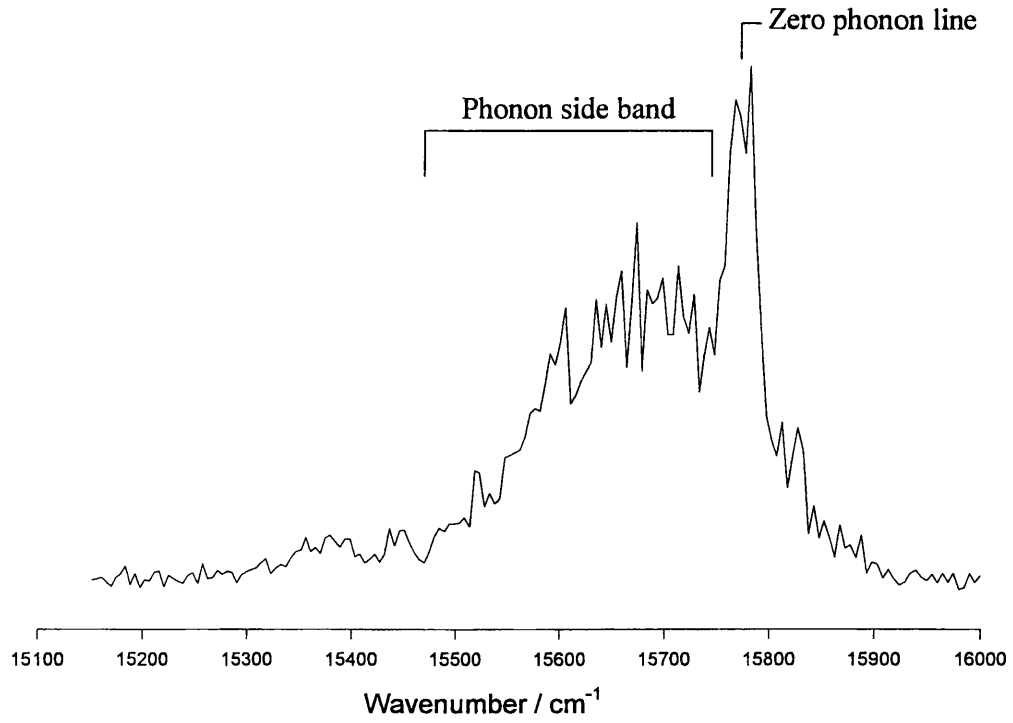

Figure 8.13 Dispersed fluorescence spectrum of CaCl in the $A^2\Pi_{1/2}$ - $X^2\Sigma^+$ (0-1) region after excitation at 16129 cm^{-1}. The zero phonon line and phonon side band are clearly visible.

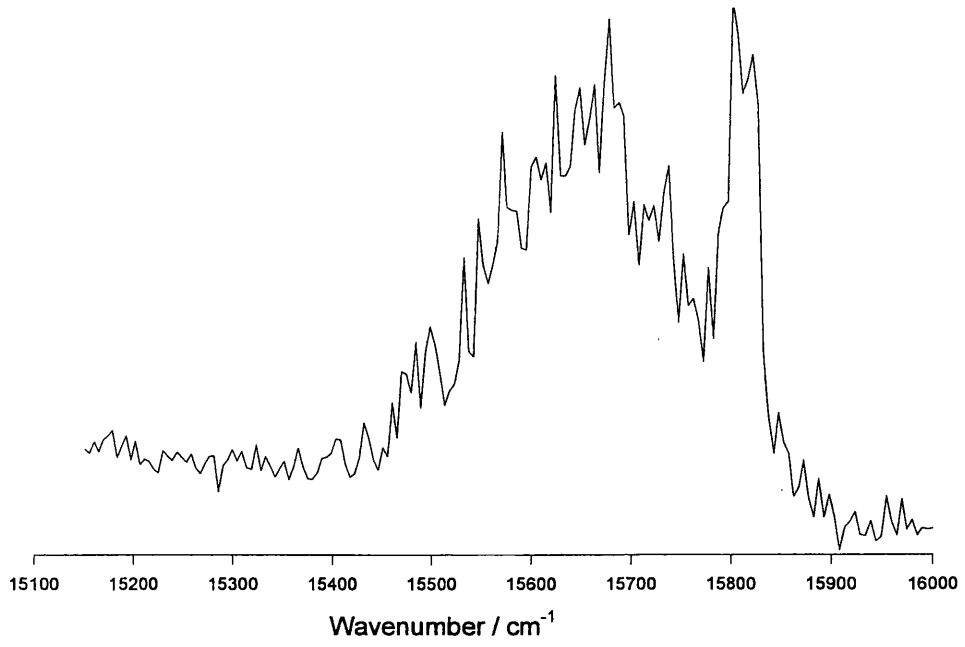

Figure 8.14 Dispersed fluorescence spectrum of CaCl in the $A^2\Pi_{3/2}$ - $X^2\Sigma^+$ (0-1) region of CaCl after excitation at 16181 cm^{-1}.

Figure 8.15 shows an action scan whilst monitoring emission at 15768 and 15823 cm^{-1}. The peaks are observed at the energies for excitation to the $\Omega = 1/2$ and 3/2 spin-orbit components of the $A^2\Pi$ state, respectively, specifically the 0-0 transitions. Emission is detected from the corresponding excited state spin-orbit component. Unlike the dispersed fluorescence spectra, the peaks in the excitation spectra do not appear to be broadened by phonon side bands; the reason for this is not clear.

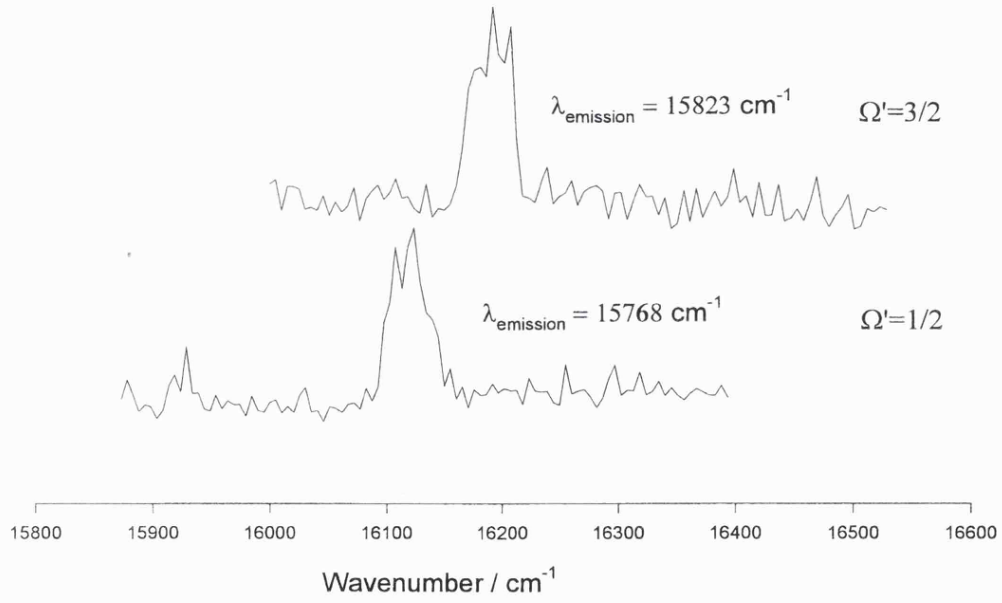

Figure 8.15 Excitation spectrum of the $A^2\Pi_{3/2,\,1/2} \leftarrow X^2\Sigma^+$ (0-0) transitions of CaCl whilst monitoring emission at a fixed wavelength. Emission is to v'' = 1 in the ground state.

The ground state vibrational frequency of CaCl in an argon matrix can be determined from the dispersed fluorescence spectra (figures 8.13 and 8.14). The difference between the centre of the zero phonon line and the pump laser position corresponds to the difference between the vibrational energy levels v'' =0 and v'' =1 in the ground state. Figures 8.13 and 8.14 yield slightly different values and therefore an average

has been taken which generates a ground state vibrational frequency of 362 ± 5 cm^{-1}. This value is close to that of Guo *et al.*, who obtained 369.8 cm^{-1}.[14]

The difference between the two peaks in figure 8.15 represents the spin-orbit splitting in the $A^2\Pi$ state. The difference between the peaks is approximately 52 ± 15 cm^{-1}. This agrees, within experimental error, with that obtained by Gao *et al.*

8.4 CONCLUSIONS

The series of experiments described here to detect various species ranging from benzene to CaCl has allowed optimisation of the experimental conditions and development of the new matrix isolation apparatus to be performed. The ultimate aim was to observe metal-containing free radicals, and in that limited sense this work was a success. However, the LIF spectra of CaCl were poor and do not bode well for future studies, especially for molecules which are more difficult to produce than alkaline earth monohalides.

There are several possible reasons why the experiments did not go as well as anticipated. Principal among them is the relatively high operating temperature of the cold head. The cold head employed was a Cryodyne Cryocooler Model 21. It should nominally be able to achieve 12 K, but it is more than 20 years old and therefore not in prime condition. The minimum matrix temperature was recorded at 20 K. This temperature is on the threshold of acceptability for a rigid argon matrix. However, the temperature at the surface of the matrix was likely to be higher due to heat dissipation from the deposition process. Under such conditions radical mobility, and therefore recombination, is likely to be facile. A cold head capable of much lower temperatures would be essential to minimise this major radical loss route.

Another substantial problem was scattered laser light. Long pass filters and/or a monochromator were used to reduce this but even so the scattered light reaching the PMT remained a serious problem. Despite our best efforts, this remains a problem.

The experimental procedure would also be greatly assisted if the LIF signals of molecules in the gas phase prior to deposition could be monitored. Real-time LIF monitoring would allow the deposition conditions to be rapidly optimised for radical production. Unfortunately, this would require major modifications to the vacuum chamber and so was not undertaken in the present study.

8.5 REFERENCES

1. V. E. Bondybey and L. E. Brus, *Adv. Chem. Phys.*, **41** (1980) 269.
2. S. Cradock and A. J. Hinchcliffe, *Matrix Isolation*, Cambridge University Press, 1975.
3. L. Khriachtchev, M. Pettersson, N. Runeburg, J. Lundell and M. Räsänen, *Nature*, **406** (2000) 874.
4. J. Lundell, M. Pettersson, L. Khriachtchev, M. Räsänen, G. M. Chaban and R. B. Gerber, *Chem. Phys. Lett.*, **322** (2000) 389.
5. M. Pettersson, J. Lundell, L. Khriachtchev and M. Räsänen, *J. Chem. Phys.*, **109** (1998) 618.
6. M. Pettersson, J. Lundell and M. Räsänen, *J. Chem. Phys.*, **102** (1995) 6423.
7. M. Pettersson, J. Lundell and M. Räsänen, *J. Chem. Phys.*, **103** (1995) 205.
8. A. M. Beardah, *PhD thesis* (1999), University of Leicester.
9. E. P. Gibson and A. J. Rest, *J. Chem. Soc. Faraday Trans.2*, **77** (1981) 109.
10. E. P. Gibson, G. R. Mant, R. Narayanswamy, A. J. Rest, S. Romano, K. Salisbury and J. R. Sodeau, *J. Chem. Soc. Faraday Trans.2*, **75** (1979) 1179.
11. J. H. Callomon, T. M. Dunn and I. M. Mills, *Phil. Trans. Royal Soc.*, **259** (1966) 499.
12. L. Andrew, W. W. Duley and L. Brewer, *J. Molec. Spec.*, **70** (1978) 41.
13. J. Goodman and L. E. Brus, *J. Chem. Phys.*, **67** (1977) 4858.
14. S. W. Guo, J. W. Chang and Y. P. Lee, *J. Chin. Chem. Soc.*, **32** (1985) 215.